MULTIPSEUDOPOTENTIAL INTERACTION: A LATTICE BOLTZMANN SCHEME FOR SIMULATION OF MULTIPHASE FLOWS

Sorush Khajepor

Submitted for the degree of Doctor of Philosophy

Heriot-Watt University

Institute of Mechanical, Process and Energy Engineering

School of Engineering and Physical Sciences

October 2017

ABSTRACT

In this study, a new pseudopotential Lattice Boltzmann (LB) scheme, multipseudopotential interaction (MPI), including boundary conditions is proposed for simulation of two-phase flows. It solves several drawbacks of available schemes such as being thermodynamically inconsistent with practical equations of state (EOSs), being limited to low-density ratios, not having an independently tunable interface width. The lattice interaction potential is described by a series of consistent sub-potentials. In theory, in addition to being intrinsically consistent with thermodynamics, the MPI-LB scheme is stable for a large range of density ratios (up to 10^6), and tunable for interface width. In engineering applications, the scheme is superior over the previous schemes of reproducing practical EOSs by removing the deficiency of creating unphysical potentials. The scheme is unlimited to implement the practical EOSs which can be expressed in a polynomial format. The scheme is studied and verified regarding liquid-vapour circular and flat interfaces, Laplace law, Galilean invariance, and change of viscosity. Furthermore, the scheme is investigated for the effects of different wall boundary conditions on the hydrodynamics of non-ideal single-phase fluids. The suitable boundary condition is chosen based on density variation across the channel, and errors because of domain resolution, relaxation time, and compressibility.

DEDICATION

Dedicated to my maman and baba, Shahnaz and Hamdola whose love for me has no boundaries nor conditions. No parameter could attenuate their support even their distance of 4,000 miles away.

ACKNOWLEDGEMENTS

I would like to thank Dr Baixin Chen who was not only my supervisor but also a good friend throughout my PhD program. Besides guiding and supporting me in Heriot-Watt University, he was always up for scientific discussion and trying new ideas.

I appreciate the help of our scientific group in different stages of my PhD program including Tariq Chaudhary, Dr Marius Dewar, Dr Jing Cui, and Dr Wei Wei.

I express my gratitude to the kind and helpful staff of Heriot-Watt University especially Dr Stephen Houston, Dr Peter Cumber for helping me with teaching, Professor Will Shu for being my second supervisor, and Mylene Honore-L'Hortalle Secretary of Institute of Mechanical, Process and Energy Engineering.

A researcher needs tranquillity to innovate. I appreciate the support of my lovely sister, Mina, and my brothers, Saeed and Sadegh, who provided peace for me from far away and all the amazing people who made Scotland my second home especially Angela, Pegah, Maryam, Jessica, Dalila, Atabak, Reza, Behnam, Jochen, Elsaye, Garry, Nurudeen, Shahriyar, Antonio, Panos, and Xavier.

ACADEMIC REGISTRY

Research Thesis Submission

Name:	Sorush Khajepor		
School/PGI:	School of Engineering and Physical Sciences		
Version: *(i.e. First, Resubmission, Final)*	Final	Degree Sought (Award **and** Subject area)	PhD Mechanical Engineering

Declaration

In accordance with the appropriate regulations I hereby submit my thesis and I declare that:

1) the thesis embodies the results of my own work and has been composed by myself
2) where appropriate, I have made acknowledgement of the work of others and have made reference to work carried out in collaboration with other persons
3) the thesis is the correct version of the thesis for submission and is the same version as any electronic versions submitted*.
4) my thesis for the award referred to, deposited in the Heriot-Watt University Library, should be made available for loan or photocopying and be available via the Institutional Repository, subject to such conditions as the Librarian may require.
5) I understand that as a student of the University I am required to abide by the Regulations of the University and to conform to its discipline.

* *Please note that it is the responsibility of the candidate to ensure that the correct version of the thesis is submitted.*

Signature of Candidate*:*		Date:	

Submission

Submitted By *(name in capitals):*	SORUSH KHAJEPOR
Signature of Individual Submitting:	
Date Submitted:	

For Completion in the Student Service Centre (SSC)

Received in the SSC by *(name in capitals):*			
Method of Submission *(Handed in to SSC; posted through internal/external mail):*			
E-thesis Submitted (***mandatory for final theses***)			
Signature:		Date:	

TABLE OF CONTENTS

NOMENCLATURE

Scales and units

Length

mm	Millimetre	10^{-3} m
cm	Centimetre	10^{-2} m
m	Meter	
km	Kilometre	10^{3} m

Mass

kg	Kilogram	
t	Tonne	10^{3} kg
Mol	Mole	

Time

s	Seconds	
min	Minutes	60s

Pressure

Pa	Pascals	kg/ms^2
bar	Bar	10^{5} Pa

Temperature

°C	Degrees Celsius	
K	Kelvin	

Angle

rad	radians	

Energy

J	Joules	kgm^2/s^2

Lattice Boltzmann terms

a, b	Arbitrary parameters of cubic equations of state

a_1, a_2, a_3, a_4	Coefficients of pressure tensor equation. For the nearest-node interactions they are $a_1 = 0$, $a_2 = 3$, $a_3 = 0$, $a_4 = 1/3.$
$\mathbf{c}_i$	Spatial vectors from a node to neighbouring nodes. They are used for calculation of interaction force between the node and nearest neighbours and beyond.
$c = \dfrac{\Delta x}{\Delta t}$	Lattice speed
$c_s = \sqrt{RT} = \dfrac{c^2}{3}$	Sound speed on the lattice
C_j	Parameters of consistent pseudopotential functions
D_i^n	n-th order total derivative in i direction in the lattice Boltzmann system ($D_i^1 = \partial_t + \mathbf{e}_i \cdot \nabla$)
$D2Q9, D3Q19, ...$	Different types of lattice
DR_{45}	Distortion ratio of a drop
DR_{90}	Distortion ratio which is the ratio of the longest diameter of a drop to the diameter perpendicular to the longest one.
$DR_{45} = \lvert 1 - r_0 / r_{45} \rvert$	Distortion ratio where r_0 is the radius of the drop along the horizontal line (0°) and r_{45} is that at 45°.
$\mathbf{E}^{(n)}$	Isotropy function of order n
$\mathbf{e}_i$	Microscopic velocity of lattice Boltzmann in i direction
e_n	Isotropy coefficient of order n
$e_2 = 1$	Second-order isotropy coefficient.
e_4	Forth-order isotropy coefficient. $e_4 = 1/3$ for D2Q9 lattice when only nearest-node interactions are considered.
f	Single-particle distribution function
f_i	Single-particle distribution function in i direction
f_i^{eq}	Equilibrium distribution function in i direction
$\mathbf{F}$	Internal or external force vector

$\mathbf{f} = \dfrac{\mathbf{F}}{\rho}$	Body acceleration
F_i	Source term or forcing term in i direction
$F^{(j)}$	Interaction force calculated from ψ_j
$\mathbf{F}^{total} = \mathbf{F}^{(1)} + \mathbf{F}^{(2)} + ... + \mathbf{F}^{(n)}$	Total force as summation of interaction forces which are calculated from $\psi_1, \psi_2, ..., \psi_n$.
F_α^{total}	A component of the total force
$\mathbf{F}_b$	A body force like gravity
g	Maxwell-Boltzmann distribution function
G	Amplitude of Shan-Chen Force
G_{fs}	Amplitude of fluid-solid interaction force
H	Boltzmann H function
$\mathbf{I}$	Identity matrix
k_B	Boltzmann constant
$K_j = -6e_4 + 12\Delta t G_j s_j$	A parameter used in definition of surface tension
Ny	Channel size or number of lattice nodes in y direction
m	A variable defined in SRK and PR equations of state
p	Pressure (scalar)
p_c	Critical pressure
$p_R = \dfrac{p}{p_c}$	Reduced pressure
$\mathbf{P}$	Pressure tensor
$p_{\alpha\beta}$	Pressure tensor component
p_0	A constant pressure or saturation pressure
p_b	Bulk pressure (equation of state pressure)
$\mathbf{Q} = Q_{\alpha\beta\gamma}\mathbf{e}_\alpha\mathbf{e}_\beta\mathbf{e}_\gamma$	Third order velocity moment of f_i^{eq}
R	Ideal gas constant
s_j	A free parameter which is added to the forcing term to change ε_j via $\varepsilon_j = -2(a_1 + 12\Delta t s_j G_j)/a_2$.
T	Temperature

T_c	Critical temperature
$T_R = \frac{T}{T_c}$	Reduced temperature
t	Time
Δt	Time step (always $\Delta t = 1$ in the lattice system)
$\mathbf{u}$	Velocity vector
$\mathbf{v} = \mathbf{u} - \frac{1}{2\rho}\mathbf{F}$	Actual fluid velocity in lattice Boltzmann system in presence of an internal or external force
$w\left(\lvert\mathbf{c}_i\rvert^2\right)$	Weight function for the interaction force in direction i. For the nearest-node interactions they are $w(1) = 1/3$, $w(2) = 1/12$.
w_i	weights of equilibrium distribution function in i direction
$\mathbf{x} = (x, y, z)$	Position vector
α	A variable defined in SRK and PR equations of state
Δx	Minimum distance between two lattice nodes
δ	Kronecker delta
$\Delta^{(n)}$	Fully symmetric tensor of the rank n
En	Kinetic energy of the system
ε_j	Parameters of consistent pseudopotential functions
$\eta = \frac{b\rho}{4}$	A variable for Carnahan-Starling equation of state
θ	Lattice temperature
κ	Coefficient of surface tension
λ_j	Parameters of consistent pseudopotential functions
μ	Dynamic viscosity
ν	Kinematic viscosity
$\nu = c_s^2(\tau - 0.5)$	Kinematic viscosity in lattice Boltzmann system
ξ	Microscopic velocity of Boltzmann equation
Ξ	Free energy density
ρ	Density
ρ_c	Critical density

$\rho_R = \frac{\rho}{\rho_c}$	Reduced density
ρ_l	Density of liquid phase
ρ_v	Density of vapour phase
ρ_s	Density of solid or wall
ρ_{ZH}	Density calculated from ZH boundary condition
ρ_{right}	Density at the right boundary
ρ_{left}	Density at the left boundary
$\boldsymbol{\sigma}$	Stress tensor
$\sigma_{\alpha\beta}$	Stress tensor component
$\sigma_{\alpha\beta}^{NS}$	Navier-Stokes stress tensor component
σ	Surface tension
$\sigma_R = \sigma / (c\, p_c)$	Nondimensional surface tension
τ	Nondimensional relaxation time
$\varphi(\rho)$	A function assumed depending only on the density
ϕ	A potential function for generalizing fluid-solid interactions
$\chi = bc^2 / a$	A parameter defined based on lattice speed c and a, b from cubic equations of state. The parameter controls the two-phase interface width in the multipseudopotential model.
ψ	Pseudopotential function
ψ^s	Single Pseudopotential function
ψ_j^M	j-th pseudopotential of multipseudopotential model
$\psi' = \frac{d\psi}{d\rho}$	Derivative of pseudopotential with respect to density
$\psi(\rho) = \left(\frac{\rho}{\lambda\varepsilon + C\rho} \right)^{1/\varepsilon}$	Consistent pseudopotential function
Ψ	Bulk free energy
$\Omega_a, \Omega_b, \Omega_c$	Constants of cubic equations of state
ω	Pitzer's acentric factor ($\omega = 0.344$ for water)

$\Upsilon = b^2 / a$	Compressibility control parameter as a function of a, b from cubic equations of state. Increase of Υ, increases the compressibility of multipseudopotential fluid.
∂	Partial derivative operator
$\partial_t = \frac{\partial}{\partial t}$	Partial derivative with respect to variable time
∇	Del or Nabla operator (vector)

Subscripts

i	Representing velocity directions on a lattice
j	Index of pseudopotentials used in multipseudopotential interaction model
q	Number of directions of a lattice
$0,1,2,...$	Lattice velocity directions
α, β, γ, …	Each one represents x, y, z coordinates.
0	Constant or initial value
R	Reduced or non-dimensional quantity with respect to thermodynamic critical point
c	Thermodynamic critical point
T	Transpose of a tensor
l	Liquid
v	Vapour
s	Solid
fs	Fluid-Solid interaction
ZH	Calculated from ZH boundary condition

Abbreviations

2D	Two dimensional
3D	Three dimensional
BEM	Boundary Element Method
CFD	Computational fluid dynamics
CS	Carnahan-Starling
CT	Computed tomography
DPD	Dissipative particle dynamics
EIT	Electrical impedance tomography
EOS	Equation of state
FDM	Finite difference method
FE	Free energy
FEM	Finite element method
FVM	Finite volume method
HCZ	He, Chen, and Zhang
HSD	He, Shan and Doolen

Kn	Knudsen number
LB	Lattice Boltzmann
LBE	Lattice Boltzmann equation
LBM	Lattice Boltzmann method
LDV	Laser doppler velocimetry
LGCA	Lattice gas cellular automata
MAC	Marker-and-cell
MD	Molecular dynamics
MPI	Multipseudopotential interaction
MRI	Magnetic resonance imaging
MRT	Multiple-relaxation-time
N-S	Navier-Stokes
PC	Phase contrast
PIV	Particle Image Velocimetry
PLIC	Piecewise linear interface calculation
PR	Peng-Robinson
RF	Radio frequency
SBB	Standard bounce-back
SC	Shan and Chen
SIMPLE	Semi-Implicit Method for Pressure Linked Equations
SRK	Soave-Redlich-Kwong
SRT	Single relaxation time
SPI	Single pseudopotential interaction
UPDV	Ultrasonic pulsed Doppler velocimetry
VOF	Volume-of-fluid
VW	Van der Waals
ZH	Zou and He
ZH-BI	ZH-based interaction
ψ-BI	Pseudopotential-based interaction
mψ-BI	Modified pseudopotential-based interaction

Non-dimensional numbers

$Ma = \frac{u}{c}$	Mach number, the ration of a velocity to the sound speed
$\mathrm{Pr} = \frac{\nu}{\alpha}$	Prandtl number, the ratio of kinematic viscosity to thermal diffusivity (α)
$Kn = \lambda / L$	Knudsen number
$\mathrm{Re} = \frac{\rho u L}{\mu}$	Reynolds number

LIST OF PHD PUBLICATIONS BY THE CANDIDATE

Journal Articles

Sorush Khajepor, John Wen, Baixin Chen, “Consistent implementation of real fluid EOS in pseudopotential lattice Boltzmann models”, 85th Annual Meeting of the International Association of Applied Mathematics and Mechanics (GAMM), Erlangen, Germany 2014.

Sorush Khajepor, John Wen, Baixin Chen, “Multipseudopotential interaction: A solution for thermodynamic inconsistency in pseudopotential lattice Boltzmann models”, Phys. Rev. E 91, 023301, 2015.

Sorush Khajepor and Baixin Chen, “Multipseudopotential interaction: A consistent study of cubic equations of state in lattice Boltzmann models” Phys. Rev. E 93, 013303, 2016.

Sorush Khajepor and Baixin Chen, “A study of boundary conditions for non-ideal fluid flow in pseudopotential lattice Boltzmann models”, submitted manuscript to Computer & Fluids journal.

Chapter 1 – Introduction

1.1 Perspective

Multiphase flows in various scales can be modelled by computational fluid dynamics (CFD) techniques solving the governing equations numerically using computers [1]. In general, the CFD techniques can be categorised based on the length scale of systems, for example, continuum and micro-scale methods have fundamentally different strategies to solve fluid flows. The Knudsen number, $Kn = \lambda / L$ [2], is a useful nondimensional number to distinguish these scales, where λ is the molecular mean free path which is about $10^{-7} m$ for air and about $10^{-10} m$ for water, and L is the characteristic length scale of the flow. When $Kn \sim 1$, fluid is considered as a discontinuous phase. Such system can be modelled by molecular dynamics (MD) [3] which solves Newton's equation of motion for every individual molecule. The gap between molecular scale and continuum is bridged by dissipative particle dynamics (DPD) [4] and the lattice Boltzmann method (LBM) [5]. DPD groups several molecules and represents them as a particle, and LBM applies the discretised Boltzmann equation for the cloud of particles. When $Kn << 1$, the fluid is a continuous phase, for which the flow dynamics can be described by macroscopic continuum theories, Navier-Stokes (N-S) equations [6]. In this chapter, after briefly overviewing experimental methods, we review the most well-known computational methods. When reaching LBM, we elaborate on different multiphase models and then narrow down the review to pseudopotential models. The advantages and drawbacks are studied which lead to the development of a new multiphase LB model proposed in this thesis.

1.2 Experimental techniques for multiphase flows

A multiphase flow can be investigated experimentally by detecting interfaces, velocities, concentrations, and chemical constituents of fluids/phases. The most popular experimental methods are magnetic resonance imaging (MRI), ultrasonic pulsed Doppler velocimetry (UPDV), electrical impedance tomography (EIT), X-ray radiography, and neutron radiography [7]. Among them the MRI and UPDV are more common and available. While the MRI equipment is much more expensive than the UPDV one, the MRI provides more technical information such as chemical constituent and interfacial dynamics of fluids/phases. The application of X-ray and neutron radiography is limited due to the safety and amount of data they can provide, for

example, the latter is used only for studying the multiphase flows involved in liquid metals. The EIT [8-10] is easy to set-up, however, analysing and interpreting the data is complicated. Only the UPDV and MRI can be used to measure velocity and dynamic properties of fluids systematically, the rest mainly can detect concentrations in the system [7] and need tracers to measure the velocities which is called Particle Image Velocimetry (PIV) [11].

The MRI has been used in study of fluids dispersion in porous media[12], sedimentation [13], suspensions [14], multicomponent stratified flows [15], and blood flow [16]. The MRI scanner is sensitive to protons in atoms. The molecules which have more rotational, trinational movements are better detected by the MRI rather than the ones which are fixed in a lattice [17]. Therefore, liquid and gas can be tracked but not a solid phase. By stimulating these nuclei and receiving their response the material and their thermodynamic state are identified. The main part of the MRI system is a magnet with the strength of 0.5-3 Tesla which can lift a regular car. It creates a uniform magnetic field inside the machine. The nuclei have a quantum characteristic called "spin" which aligns in the same or opposite direction of the main magnetic field [18]. The same-direction nuclei have less energy; however, the opposite-direction ones have more energy to keep their position. The useful phenomenon is that the number of the nuclei whose spin are oriented in the direction of the magnetic field are more than the ones in the opposite direction. The extra low-energy nuclei are the ones that the machine records the response of. The machine signals are sent via radio frequency (RF) coils which are absorbed by low energy nuclei. Their spin orientation changes to the opposite direction. They are not stable at high energy level because when the RF is switched off, they come back to their low energy level with the release of magnetic energy which is recorded with a receiver RF coil. But how to scan different locations in a domain? The nuclei only react to the signals at the "resonant frequency" which is dependent on the intensity of the magnetic field they are in. The higher the magnetic field the higher is the resonant frequency. Therefore, in a one-dimensional system, for example x direction, another coil is necessary to change the effect of the main magnet and create a gradient field (see Figure 1-1). For example, in x direction, the magnetic field decreases along the x axis. This causes the resonant frequency of nuclei to be changed along the x axis. Therefore, by sending RF energy at the resonant frequency

of $x = x_0$, only the nuclei placed at $x = x_0$ respond. This can be done in three dimensions by creating gradients of magnetic field in all x, y, and z axis. More details of the principle of MRI for detecting the fluids interactions and measurement of fluid velocity can be found from Günther's book [19] for reference.

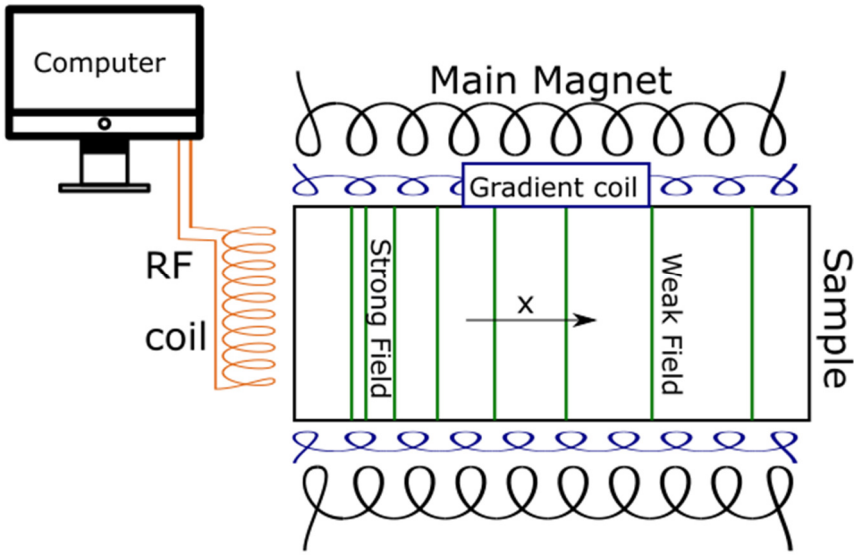

Figure 1-1. A simple schematic of an MRI machine.

The MRI can measure the velocities of fluid flows at the range of as low as 10^{-3} mm/s to 10^{2} cm/s [18]. In the rapid MRI systems the velocity and concentrations can be measured in the order of 10 ms [17]. It is possible to tag some part of the fluid and track them. In contrast to overall of the domain, that pixel does not send signals, which helps find velocities and concentrations in emulsions [17], the images of fluids' interfaces, and size distributions of droplets/particles/bubbles [20]. The phase contrast (PC) techniques in the MRI also can be used to measure fluid velocities [16]. The resolution of measurements generally depends on gradient of magnetic field, relaxation times of samples, and size of the coils [21].

X-ray is created by ionizing tungsten with the aid of an electron beam from a cathode. This beam is accelerated with a high potential voltage between cathode and anode and once it hits the anode the electromagnetic radiation is emitted. X-ray can pass through a multiphase system and is collected on a photographic film or digital detector. The beam is attenuated by different phases/materials in different ways. Therefore, a dense phase, that absorbs the most, is seen bright and a light phase is seen dark on the image. A

simple schematic of an X-ray scanner is shown in Figure 1-2. The attenuation of X-ray is described by Beer-Lambert law for multiphase flow [22, 23]

$$I = I_0 \exp[-((1-\varepsilon)\mu_1 + \varepsilon\mu_2)l] \tag{1-1}$$

where I_0 is the initial energy emitted, I is the captured beam, μ_1 and μ_2 are the absorption coefficients for two phases, ε is the volume fraction of phase 2, and l is the path of X-ray through the sample. The absorption depends on the atomic number of materials and the intensity of the X-ray [23].

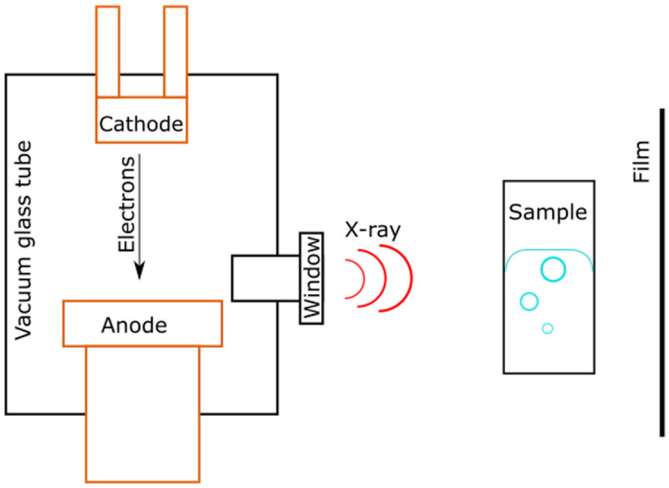

Figure 1-2. A simple schematic of an X-ray scanner.

X-ray is widely used in medical industry and can be used to take a sequence of images to follow the motion of objects [24]. Moreover, it can be used to study multiphase flows, for example, the dynamics of dense liquid jets [25], particle motions in concentrated suspensions [26], size and rise velocity of bubbles in a fluidized bed [27] [28, 29]. To have better images of 3D complex systems X-ray computed tomography (CT) should be used which gives high spatial resolution [30, 31]. A CT scan take hundreds of images of a sample in different directions and combine them to create a 2D image of a slice through the sample. By moving forward and finding the other slices a 3D image of the sample is obtained. Therefore, X-ray CT has a low temporal resolution which makes it suitable for time-averaged phase distributions [23].

The UPDV was at first used for blood flow measurement [32], but since then has been extended for velocimetry in different types of fluid flows and engineering applications

[33] such as flow of paper pulp suspensions [34], and dispersed gas phase in multiphase flow [35]. The UPDV, based on the Doppler effect, can measure the velocity of moving particles or tracers in the fluids. A transducer sends ultrasonic waves, and then measures the scattered wave that is reflected from the particles. The wave travels inside the fluid with slight, or no attenuation. The velocity (v_z) of the particle along the channel can then be estimated by

$$v_z = \frac{cf_D}{2f_0 \cos\theta} \tag{1-2}$$

where f_D is Doppler shift frequency (1/s), c is the sound speed (m/s), f_0 (1/s) is the frequency of the incident wave, and θ is the angle of transducer relative to the flow direction [7]. As shown in Figure 1-3 the distance of the particle from the transducer, S (m), can be calculated with the aid of the wave velocity and travel time, τ (s).

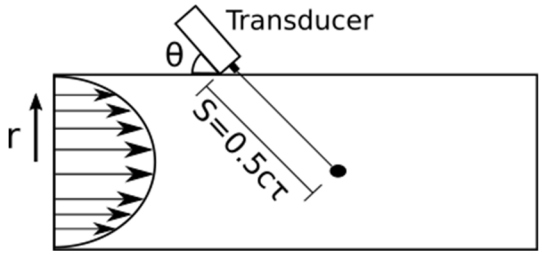

Figure 1-3. The transducer emits ultrasonic waves in a fully developed laminar flow and receives the scattered wave from the particle in the fluid. The distance of the object from the transducer is known by the travel time of the wave [7].

Laser doppler velocimetry (LDV) is also based on Doppler effect. However, instead of ultrasonic waves, radiations such as He-Ne laser are adopted. The laser is scattered by polystyrene spheres which are placed in the fluid to create a dilute colloidal suspension [36]. The method is mostly used in blood flow measurements [37-39].

Bonnecaze and co-workers [8-10] developed EIT that can be used to find the distribution concentrations of particles in a pipe flow, in which 32 electrodes are placed around the pipe and a specific current is applied to two opposite electrodes and the voltage difference at neighboring electrodes are measured. Bonnecaze and co-workers developed a method that, using this data and the surface conductivity, finds the distribution concentrations of suspensions in the fluid [8-10].

Neutron radiography is used specifically to study the two-phase flows of liquid metal with a gas phase which needs a high flux research reactor and a fast speed, sensitive camera [40]. Neutron beam can travel through the liquid metal but is weakened by the gas. A converter changes the neutron beam to visible light and then is captured by the camera. In general, both the X-ray and Neutron radiography techniques provide 2D images which are a projection of the 3D system [7].

Experiments detect and measure the physical phenomena from laboratory facilities or the engineering processes, however, they have some disadvantages and limitations in comparison with numerical modelling. Firstly, either the laboratory or the engineering measurements are costly, including the cost of experiment equipment and the cost of supporting systems, such as MRI, which is currently, with the 1.5 Tesla configuration, sold £120,000-£270,000 on the Internet. Secondly, the equipment usually is not versatile to measure different desired fields such as 3D geometry of phases, velocities, densities, and temperatures. Thirdly, the accuracy of the results of an experiment is limited to the capabilities of the machine which is used, for example, X-ray CT having good spatial but weak temporal resolutions. On the other hand, the numerical simulations relatively cost lower. For example, with a laptop and free open-source packages many different flows can be studied for limited time steps and resolutions. They have the flexibility to be set for heat-transfer flow, isothermal flow, flow in porous media, multiphase flow, and so forth. The uncertainties of numerical simulation can be tested and estimated before further utilization in engineering productions and maintenance. In the following section, we discuss different models for simulating multiphase flows.

1.3 Numerical models for multiphase flows

Scientists are encouraged to develop numerical models due to the need for predicting and analysing the behaviour of multiphase flows in natural processes, such as the eruption of volcanos, the formation of fog and cloud, and the transportation of pollutant particles, and in industrial processes, such as the processes in boiler, evaporators, reactors, and enhanced oil recovery. A multiphase system in its simplest form is liquid and vapour coexistence of a fluid, for example, water and steam. It can be a mixture of multiple immiscible fluids such as air and water which can also be called a

multicomponent system. The system can be even more complex if a solid phase is considered together with fluids. The main characteristic of the multiphase system is the existence of an interface between phases where a sharp jump of properties is seen and the physical/chemical interactions occur. Therefore, to describe the system a new set of parameters such as density ratio and viscosity ratio between phases appear. For example, the oil-water mixture is considered as low-density ratio system in contrast to the water-air mixture.

The characteristic length and time scales of multiphase flows are the primary points for identifying the physics of interfacial interactions and for developing simulation models. The Knudsen, Kn, number can be a good criterion for distinguishing fluid flows at micro-scale from macro-scale. For a liquid jet emerging from a nano-size nozzle the characteristic length can be the diameter of the channel or thermal fluctuation length of the fluid molecules, $Kn \sim 10^{-2}$. Therefore, molecular level models such as MD [3] are a practical choice. Assessing the behaviour of a shell and tube heat exchanger, for which the characteristic length is possibly defined based on the internal diameter of a tube, $Kn < 10^{-7}$, the fluids are continuum and an N-S equation solver is a popular selection. DPD [4] is the method applied in between those scales as a mesoscopic approach $10^{-7} < Kn < 10^{-4}$ (see Figure 1-4). From a computational viewpoint, the scale analysis can help to simplify the system, for instance, it is not necessary to solve the full N-S equations when study the flows in a reservoir at the scale of $100m$ while the pore size is in the order $10\mu m$. In such case, by redefinition of characteristic length, a simplified version of the N-S equations such as Darcy's law is an efficient option.

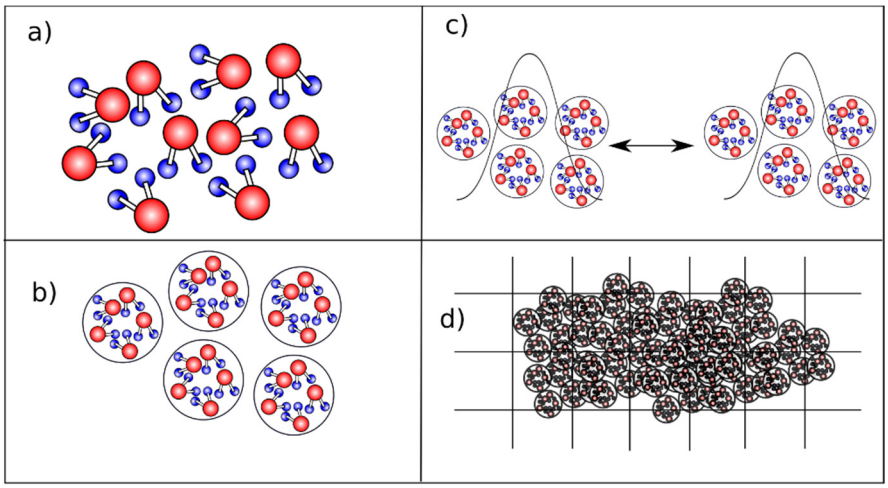

Figure 1-4. Characteristic length of the system helps choosing the right method of simulation: a) molecular dynamics (10^{-9} m to 10^{-7} m) where actual atoms and bonds are simulated, b) DPD where a particle is a cluster of molecules (10^{-7}m to 10^{-4} m), c) LBM where a continuous distribution of particles are focused, d) continuum solution where all constituent elements form a continuous phase.

Lattice Boltzmann methods as an N-S alternative has common characteristics with both Continuum CFD and particle-based CFD methods. The Taylor expansion of LB equation leads to the incompressible N-S equation at small Mach numbers, $Ma \ll 1$, which is explained in section 2.5. Mach number, $Ma = u / c$, is the ratio of fluid flow velocity, u (m/s), to the sound speed in the fluid, c (m/s) [6]. In comparison with particle-based methods, LBM uses particle distribution which removes the noise and fluctuations. The interface of a liquid drop with its vapour is smooth in each time step and doesn't require averaging over many time-steps similar to what we observe in traditional CFD methods. This behaviour implies a scale far bigger than nanoscale.

At the same time, the particle distributions can move very similar to particles. Therefore, interaction potentials and particle boundary conditions can be defined for them. The interaction potential can be the ones originating from the molecular level to model a two-phase, liquid-vapour, coexistence. Such system forms automatically without the need for tracking interfaces.

Another important feature of LBM is being run on a lattice (mesh) like traditional CFD methods, therefore, the distributions can find each other and next position straightforwardly. Therefore, there is no need for algorithms, which search for neighbouring particles, found in MD and DPD. The collisions of particles happen

locally and, usually in multiphase systems, the information only from nearest-nodes are requested. These characteristics make the model suitable for parallel processing.

Overviewing the particle-based and traditional CFD methods helps to understand multiphase models applied in LBM. For example, the model proposed by He et al. [41] is inspired by level-set method (see section 1.4.3) and bounce-back boundary condition, found in MD and DPD, is employed in LBM as well (see 5.2.1). Therefore, to identify the characteristics of existed fluids flow models, a brief discussion is made as follows.

1.3.1 Molecular dynamics

Molecular dynamics models the motion of every single atom or molecule and, the macroscopic and microscopic properties of materials are found from constituent particles [3]. The molecules are moving and interact with each other in the computational domain based on Newton's equations of motion. A system of N molecules is solved with N equations of motion. They are usually discretized with velocity Verlet algorithm or leap frog method which are superior regarding accuracy and stability [42]. Position and velocity of particles, being microscopic quantities, are calculated in each time step. In addition to the temperature, which is defined as a type of kinetic energy of molecules related to velocity, the instantaneous value of macroscopic properties of the system, such as pressure and viscosity fluctuate in time. They are sampled and averaged over a short period of time to be comparable with experimental data.

If the particles are spherical, only transitional motion is considered. In the case of non-spherical particles, the rotational motion is important and must be modelled as well. Particle transitional and rotational velocities are initialized with the aid of Maxwellian distribution. The kinetic temperature of the system is found from these velocities which are scaled through an equilibration procedure to match to desired temperature [43].

The interactions between particles are either bounded or non-bounded. Bounded interactions are intra-molecular bonds between atoms which have three components: interatomic distance, bend angle and torsion angle [44]. The non-bounded interactions originate from potential energy of individual atoms, pairs, triplets and so on [3]

$$V = \sum_i v_1(\mathbf{r}_i) + \sum_i \sum_{j>i} v_2(\mathbf{r}_i, \mathbf{r}_j) + \sum_i \sum_{j>i} \sum_{k>j>i} v_3(\mathbf{r}_i, \mathbf{r}_j, \mathbf{r}_k) + \dots . \quad (1\text{-}3)$$

where $\mathbf{r}$ is the position of particles and i, j, and k are the index of particles. The first term, v_1, is the external field potential such as walls around the domain. The second term v_2 is the pair potential which is only a function of the distance between pair particles. While v_2 is the most significant potential, v_3 share is also considerable, for example, they form 10 per cent of the lattice energy of argon; the share of other potentials is negligible [3]. Calculation of triplet interactions is highly time-consuming on computers, thus, as a workaround, the pair interactions are modified to partially cover the rest [3]

$$V = \sum_i v_1(\mathbf{r}_i) + \sum_i \sum_{j>i} v_2^{eff}(\mathbf{r}_i, \mathbf{r}_j) . \quad (1\text{-}4)$$

A simple but practical choice of potential is Lennard-Jones 12-6 which predicts the properties of argon satisfactorily to replace the second term of Eq (1-3),

$$v^{LJ}(r) = 4\varepsilon \left[(\frac{\sigma}{r})^{12} - (\frac{\sigma}{r})^{6} \right] . \quad (1\text{-}5)$$

where ε is well-depth parameter, r is the distance between particles, and σ is a distance parameter. In the parentheses, the first term represents short distance repulsion and the second term long-range attraction of molecules. For example, by setting $\varepsilon / k_B \approx 120K$ (where the $k_B = 1.38064852 \times 10^{-23}$ J/K is the Boltzmann constant) and $\sigma \approx 0.34nm$, the equation models liquid argon [3]. When there are different molecules (or components) in the system, for example A and B, besides the pair potentials between same molecules A-A and B-B, the interaction potential of different types A-B should be constructed. In this way, the phase separation happens automatically as a consequence of different interactions. The interactions are firstly guessed and by simulations refined to obtain desirable macroscopic properties.

An MD simulation is limited by the number of molecules [45] and time steps in the system. A mole of water, being only $18.015g$, contains 6.022×10^{23} molecules. The current fastest supercomputer, Sunway TaihuLight, has nearly 10^7 computational cores [46]. Therefore, to simulate $1g$ of water, every core should process about 3×10^{15}

molecules which is far beyond capabilities of current computer memories and processors. Secondly, time step should capture the fastest vibrational frequency of molecules which can be extremely small, in the order of femtoseconds i.e. $10^{-15}\,s$.

1.3.2 Dissipative particle dynamics

Dissipative particle dynamics is a mesoscopic particle based technique introduced by Hoogerbrugge and Koelman [47] for predicting hydrodynamic behaviour of fluid in mesoscale. Since then, it has gained significant theoretical supports and refinements [4, 48-50]. Flexibility of the method made it successful in simulating various complex fluids flows [51-54]. DPD particles while showing correct hydrodynamics, move randomly in a computational domain to reproduce the desired temperature, thus, thermal fluctuations are inherent in such system. DPD has been used widely to model hydrodynamic problems in small scales, such as the simulation of micro-drop breakup in a shear flow [55], multiphase fluid flow in microchannels [56], nanojet breakup [57], water flow in a microchannel [58] and electroosmotic flow in nano-fluidic devices [59].

The method has the inherent capability of building a distinct interface between two immiscible fluids, by simply adjusting interparticle forces. Therefore, finding the location of interface and its curvature is not a critical issue. It can be appropriately used for simulation of flows when atomistic fluctuations influence the dynamics of the process, for example, the brake-up of liquid jets at small scales $(Kn \sim 1)$ [60].

DPD constituent elements are coarse-grained particles each of which is a cluster of atoms or molecules that move randomly in computational domain and demonstrate the behaviour of a fluid of interest. Movement of these particles is governed by the Newton second's law

$$\frac{\partial \mathbf{r}_i}{\partial t} = \mathbf{v}_i,\ m_i \frac{\partial \mathbf{v}_i}{\partial t} = \mathbf{f}_i \tag{1-6}$$

where $\mathbf{r}_i$, $\mathbf{v}_i$, m_i are the position, velocity and mass of the particle i, respectively. The mass of a particle as an independent parameter is usually considered to be unity. The total force $\mathbf{f}_i$ acting on each DPD particle i is a combination of three pair-wise forces: conservative, dissipative and random forces [4]

$$\mathbf{f}_i = \sum_j \mathbf{F}_{ij}^C + \mathbf{F}_{ij}^D + \mathbf{F}_{ij}^R \qquad (1\text{-}7)$$

The sum j runs over all neighbouring particles from a particle. The magnitude of interaction forces decreases with the distance and becomes zero beyond cut-off radius, R_c. Therefore, a particle only sees the other ones which are within its R_c. The conservative force can be accounted for long-tail attraction and short distance repulsion of molecules. The dissipative force represents the friction between particles which defines viscosity in the system. The random force is a source of kinetic energy which counteracts the effect of dissipative force to keep the system temperature constant. In contrast to MD which atoms repel each other through hard forces, here they are soft. In other words, even if two particles overlap the repulsion interaction between them is a finite value, similar to "a school of fish" in which the fishes pass through each other where each fish resembles an atom and their group a DPD particle.

Since the method includes random, dissipative and conservative forces, it bears a resemblance to a Brownian-dynamics algorithm. The conservation of momentum is guaranteed naturally due to the pairwise nature of forces, and angular momentum is conserved since all forces are central forces. In order to ensure that the system reaches the correct equilibrium distribution, the dissipative and random forces must obey the fluctuation-dissipation relation: $\sigma^2 = 2\gamma k_B T$, where σ and γ are the amplitudes of random and dissipative forces respectively, T is the system temperature and k_B is the Boltzmann constant [48]. The kinematic energy, $k_B T$, of a stationary fluid is also considered as an independent parameter and it is conventionally set at 1 for the sake of simplicity [4].

In DPD method, the scale of simulations and the number of molecules that each particle is representative of can be considered through dominant non-dimensional numbers which connect the system to the real world. However, the thermal fluctuations and limitation on the number of particles in the domain, due to the random forces and computational resources, keep the scale of simulations between molecular level and continuum. Similar to MD, instant properties, sampled from the system, are noisy and,

to obtain a constant value, averaging them over thousands of time steps is inevitable. This also includes the geometric shapes and boundaries of components such as phase interfaces.

1.3.3 Continuum scale models

The flow of a continuum fluid can be described by the N-S equation, which is derived by applying Newton's second law to a continuum fluid [6],

$$\frac{\partial(\rho\mathbf{u})}{\partial t}+\nabla\cdot(\rho\mathbf{u}\mathbf{u})=-\nabla p+\rho\mathbf{f}+\nabla\cdot\boldsymbol{\sigma} \tag{1-8}$$

where ρ is the density of fluid, $\mathbf{u}$ the velocity, p the pressure, and $\mathbf{f}$ a body force acting to the fluids, and $\boldsymbol{\sigma}$ the stress tensor. In general, the mass conservation is guaranteed by

$$\frac{\partial\rho}{\partial t}+\nabla\cdot(\rho\mathbf{u})=0 \tag{1-9}$$

This set of equations, in principle, can be solved by numerical methods which has dramatically evolved since the early 1930s [61]. Due to the limitation of the computability, the methods proposed during 1930 to 1950 were mostly focusing on how to reconstruct the N-S, linearize the convection term with reasonable assumptions, if unable to exclude it, and reduce it to a potential equation [61].

The scientists of a group in Los Alamos National Lab made the pioneer work on CFD by proposing a set of numerical methods, Particle-in-cell, to describe the original governing equations mathematically using finite difference method [62]. Then the more general CFD frameworks developed by means of finite volume method (FVM) [63], finite element method (FEM) [64] and finite difference method (FDM) [65]. The scheme, called as Semi-Implicit Method for Pressure Linked Equations (SIMPLE), and then the SIMPLER and SIMPLEST, proposed by Brian Spalding and Suhas Patankar [66], fully solved the Naver-Stokes equation by iteration of pressure and velocity.

Multiphase flow in the continuum scale is commonly studied in the "one-fluid" scheme that merely one set of equations govern whole simulation domain [67]. The first successful attempt was the marker-and-cell (MAC) method [68] which presented in the

early 1960s. The marker particles in MAC method are positioned uniformly in the different fluids and the properties of the fluids are rebuilt from them. The MAC method is currently obsolete. However, the one-fluid scheme is developed in various ways.

In the one-fluid scheme, the fluid is solved by the governing equations and a marker function differentiates phases from each other. The flow advects the marker function [67]. Several ideas presented for the scheme such as volume-of-fluid (VOF) method [69], and the level-set method [70]. If the interface between phases is tracked by points and the marker function is constructed from their locations, the method is called front-tracking [71].

The one-fluid's momentum equation, based on the incompressible N-S equation with surface tension force, is [67]

$$\rho\frac{\partial \mathbf{u}}{\partial t}+\rho\nabla\cdot\mathbf{uu}=-\nabla p+\rho\mathbf{f}+\nabla\cdot\mu(\nabla\mathbf{u}+\nabla^{T}\mathbf{u})+\sigma\kappa\delta(n)\mathbf{n} \tag{1-10}$$

where μ is the viscosity, σ is the coefficient of interface tension, $\kappa=\nabla\cdot\mathbf{n}$ is the curvature of the interface, $\mathbf{n}$ is the vector normal to the interface, and n is a normal coordinate to the interface. The variables ρ and μ are the same for each phase but the value skip at the interface. The last term is the surface tension force which is acting only at the phase interface because of the δ-function. The mass conservation for incompressible system stays the same as a single-phase system

$$\nabla\cdot\mathbf{u}=0. \tag{1-11}$$

After knowing the fluid interface, the marker function, α, which is a smooth step function, is determined: 0 in one phase and 1 in the other phase. The α function is then advected with the flow velocity

$$\frac{\partial\alpha}{\partial t}+\mathbf{u}\cdot\nabla\alpha=0 \tag{1-12}$$

Therefore, α can be found at the next time step by integrating equation (1-12). The density and viscosity across the interface are then defined as

$$\rho=\alpha\rho_{1}+(1-\alpha)\rho_{0}, \tag{1-13}$$

$$\mu = \alpha\mu_1 + (1-\alpha)\mu_0 ,$$

where 0 and 1 are two present phases. Solving the integral (1-12) is not straightforward since a first-order scheme such as upwind scheme produces fast artificial diffusion and a second-order scheme such as Lax-Wendroff brings interface fluctuations [67].

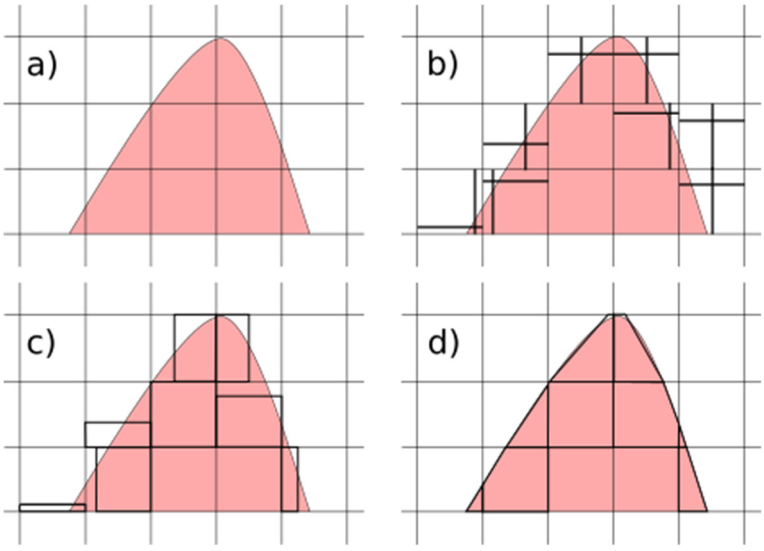

Figure 1-5. Identification of phase interface by VOF method: a) the actual interface, b) SLIC scheme where the horizontal and vertical line define the advection in y and x-direction respectively, c) Hirt-Nichols where advection is only in one direction, d) PLIC where the interface is at optimal orientation [67].

VOF method attempts to solve this problem by finding an interface line or plane in boundary cells. Noh and Woodward [69] introduced a simple scheme for VOF in which the cell at the interface is divided by a vertical line for advection in x direction and a horizontal line for y direction. Hirt and Nichols [72] suggested that either horizontal or vertical slice is chosen based on the information of neighbouring cells. Rudman [73] showed both methods suffer from "flotsam" where the interface elements break apart unrealistically. Youngs [74] proposed a method where the interface line in a cell can have any orientation which is found from the normal vector to the interface. It is approximated by the average value of α at the cell and its neighbours. The quality of the outcome mainly depends on the accuracy of the interface reconstruction. This

strategy called piecewise linear interface calculation (PLIC) [73], see Figure 1-5. Although interface reconstruction in three-dimensional domains becomes complex, VOF method is widely used in free-surface or multiphase flow simulations and adopted in many commercial CFD packages.

Level-set is another marker-function advection method which is presented by Osher and Sethian [70] and the same as VOF method it can model coalescence and breakup of drops intrinsically. However, it sees the evolution of the interface differently. A two-dimensional interface, from the level-set viewpoint, is an x-y slice of a three-dimensional surface at a particular time. In other words, the observer is a camera inside a dark 3D tube which is moving forward with time and only sees a tiny bit ahead. Therefore, a level-set function, $\phi(\mathbf{x},t)$, which is basically a function of the normal distance to the interface, is defined (see Figure 1-6). The function is advected the same as equation (1-12). But ϕ doesn't stay as a distance function which, therefore, Sussman, Smereka and, Osher [75] introduced an iterative method to reinitialize it. After the correction, a smoothed step function, $h(\phi)$, interprets viscosity and density while the curvature is calculated from ϕ function.

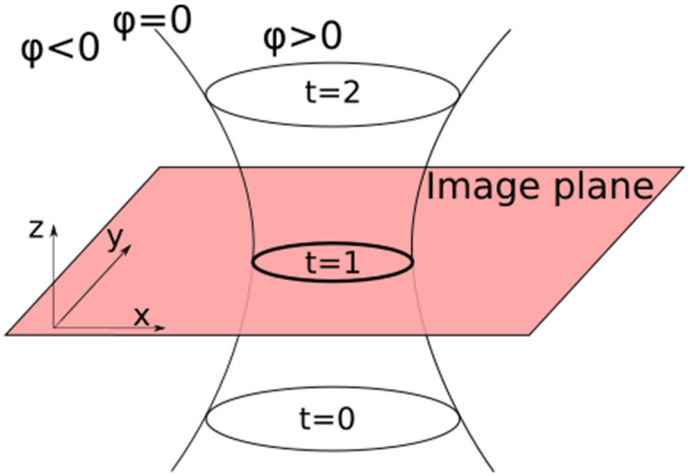

Figure 1-6. Level-set function is a three-dimension function which is defined by the distance to the interface. The slice of the function at desired time and $\phi=0$ is the desired interface in a 2D system.

Front-Tracking methods [71, 76-78] try to track the location of the interface with the aid of an additional moving mesh (see Figure 1-7). They can reproduce sharp front with high resolution [71]. The most popular front-tracking methods are the boundary-fitted

grid method [76], Tryggvason's hybrid method [77] and the Boundary Element Method (BEM) [78].

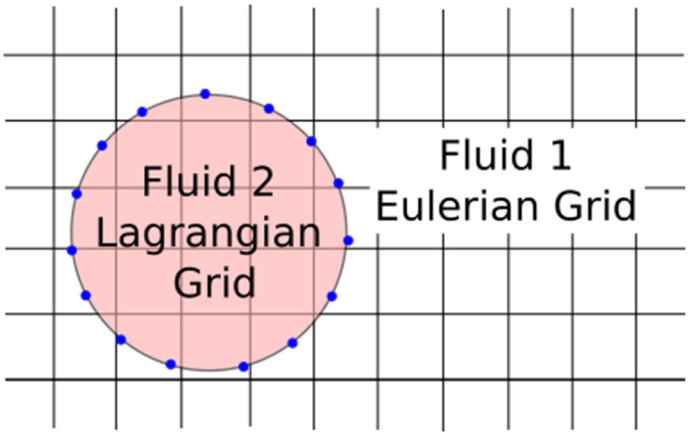

Figure 1-7. Front-tracking considers a moving Lagrangian grid around the suspended phase while the main fluid is solved on a stationary Eulerian grid.

Advecting and tracking the interface have always been challenging in traditional CFD. For example, constructing the interface topology in the VOF method is very complex in a 3D domain. Level-set in each time step uses iterative methods which are computationally expensive. In the case of front-tracking methods, handling a moving mesh within a fixed grid can be sophisticated, especially when drops break up or coalesce. Moreover, in these systems, the efficient traditional Poisson solvers are not applicable anymore as the density is not constant.

Mixture, diffusion, or averaged-equation model [67] is another one-fluid model which, in comparison to VOF and level-set models, the phases can penetrate into each other. Continuum and Momentum equations (without turbulence) for the mixture are written as

$$\frac{\partial}{\partial_t}(\rho_m) + \nabla \cdot (\rho_m \mathbf{u}_m) = 0$$

$$\frac{\partial}{\partial_t}(\rho_m \mathbf{u}_m) + \nabla \cdot (\rho_m \mathbf{u}_m \mathbf{u}_m) = -\nabla p_m + \nabla \cdot (\boldsymbol{\sigma}_m + \boldsymbol{\sigma}_{Dm}) + \rho_m \mathbf{f} + \mathbf{M}_m \tag{1-14}$$

where m is mixture, $\mathbf{M}$ is interface tension forces, $\boldsymbol{\sigma}$ is stress tensor for the mixture and diffusion

$$\boldsymbol{\sigma}_m = \sum_{k=1}^{n} \alpha_k \tau_k$$

$$\boldsymbol{\sigma}_{Dm} = \sum_{k=1}^{n} \alpha_k \rho_k \mathbf{u}_{Mk} \mathbf{u}_{Mk} \tag{1-15}$$

where $\mathbf{u}_{Mk}$ is the velocity of phase k relative to the mixture velocity and the volume fraction parameter $0 \le \alpha \le 1$ determines the phases. The mixture model is viable for the dilute suspension of particles or widely dispersed small bubbles in the main phase [79].

Multifluid model, which commonly called two-fluid model, is a general continuum model which describes all phases/components as continuum fluids penetrating each other with explicit interfaces. The physical and chemical interactions among the phases/components are presented as the source terms in continuum and momentum equations, which are written for a laminar flow (without chemical reactions) as

$$\frac{\partial(\alpha_k \rho_k)}{\partial_t} + \nabla \cdot (\alpha_k \rho_k \mathbf{u}_k) = 0$$

$$\frac{\partial}{\partial_t}(\alpha_k \rho_k \mathbf{u}_k) + \nabla \cdot (\alpha_k \rho_k \mathbf{u}_k \mathbf{u}_k) = -\alpha_k \nabla p + \nabla \cdot \boldsymbol{\sigma}_k + \alpha_k \rho_k \mathbf{f}_k + \sum_{j=1}^{n} R_{jk} \tag{1-16}$$

where k indicates the fluids/phase, n number of phases/fluids, and R_{jk} is the momentum transfer from phase j to phase k. Pressure, p, is the same for all phases/fluids. The application of the full multiphase flow models in engineering depends on efficiency and computational costs of the sub-models of interphase interactions, including the mass and momentum exchanges. The increase of the computation costs by using this model could be estimated by the number of fluids/phases of the system, which means the number of sets of the N-S equations to be solved, in addition to the cost of turbulence modelling for each phase/fluid. The system of equations are not hyperbolic; to overcome that more assumptions should be made [80] such as the interfacial pressure force [81]. For more details, refer to [67].

1.3.4 Lattice Boltzmann method

From the theories of statistical mechanics, a fluid can be described with the aid of distribution function $f(\mathbf{x},\boldsymbol{\xi},t)$ which is defined as the number of molecules at time t are placed between $\mathbf{x}$ and $\mathbf{x}+d\mathbf{x}$, and moving with a velocity between $\boldsymbol{\xi}$ and $\boldsymbol{\xi}+d\boldsymbol{\xi}$. If all these molecules could experience same external force $\mathbf{F}$ and there were no interactions among them, we could have, based on Newton's law of motion, $f(\mathbf{x},\boldsymbol{\xi},t)dx\,d\boldsymbol{\xi} = f(\mathbf{x}+\boldsymbol{\xi}dt,\boldsymbol{\xi}+\mathbf{F}dt,t+dt)dx\,d\boldsymbol{\xi}$ [82]. However, in reality, the interactions of fluid molecules are inevitable and must be taken into account for describing the behaviour of the fluid, therefore,

$$f(\mathbf{x}+\boldsymbol{\xi}dt,\boldsymbol{\xi}+\mathbf{F}dt,t+dt)d\mathbf{x}\,d\boldsymbol{\xi} - f(\mathbf{x},\boldsymbol{\xi},t)d\mathbf{x}\,d\boldsymbol{\xi} = \Omega(f)d\mathbf{x}\,d\boldsymbol{\xi}dt \tag{1-17}$$

where Ω is the collision operator. By finding the limit of the equation at $dt \to 0$, we find $\frac{df}{dt} = \Omega$, i.e. the Boltzmann equation [82]

$$\frac{\partial f}{\partial t} + \boldsymbol{\xi}\cdot\nabla f + \frac{1}{m}\mathbf{F}\cdot\nabla_{\xi} f = \Omega \tag{1-18}$$

where m is the mass of a particle. Boltzmann proved function

$$H(t) := \int d^3\boldsymbol{\xi} d^3\mathbf{x}\, f(\mathbf{x},\boldsymbol{\xi},t)\, \ln f(\mathbf{x},\boldsymbol{\xi},t) \tag{1-19}$$

always satisfies

$$\frac{dH}{dt} \le 0 \tag{1-20}$$

which is called H theorem [83]. The Maxwell distribution can be found from H theorem and, therefore, such equilibrium guarantees increase of entropy and stability [84, 85].

This equation is mapped on a discrete space and momentum domain to be solved computationally, which is called as lattice Boltzmann equation [86]

$$f_i(\mathbf{x}+\mathbf{e}_i\Delta t,t+\Delta t) - f_i(\mathbf{x},t) = -\frac{1}{\tau}\left[f_i(\mathbf{x},t) - f_i^{eq}(\mathbf{x},t)\right] + F_i(\mathbf{x},t), \tag{1-21}$$

where index i shows the discretized velocity directions, F the forcing term, τ the relaxation time and f^{eq} the Maxwell-Boltzmann distribution function. The first term on the right-hand side is the [87] approximation of the collision. LB equation and relative theories will be discussed in section 2.2 in detail.

The LB equation is an outcome of gradual development. McNamara and Zanetti in 1988 [88] presented the LBM as the successor of lattice gas cellular automata (LGCA) and a novel method to simulate hydrodynamic behaviour. Their LBM uses continuous distributions instead of Boolean fields in LGCA models and Fermi-Dirac distribution as the equilibrium function. Higuera et al. in 1989 [89] linearized the collision operator. Individual collisions are replaced with the BGK approximation of coarse-grained collisions by Koelman in 1991 [90] and Qian et al in 1992 [91], independently.

The LBM is a model developed as improvement of many drawbacks associated with LGCA. The motion and collision of a cloud of particles are investigated, instead of each individual particle. Therefore, it removes the intrinsic noise of its predecessor. In LGCA method, pressure is directly a function of velocity which makes no physical sense and transport coefficients are limited in a narrow range of values [92]. Moreover, they lack Galilean invariance [86]. Galilean invariance is explained in section 4.6.5. In principle, LBM has a great potential to overcome those drawbacks.

The Lattice Boltzmann method emerged from the kinetic-theory approach and successfully found many applications in various aspects of CFD such as, turbulent flows [93], flows in porous media [94, 95], blood rheology [96, 97], and biopolymer translocation [98, 99] while having the capability of being combined with the continuum CFD methods [100]. Filling the gap between continuum and molecular levels, the LB method facilitates incorporating mesoscale interaction potentials. An outstanding outcome of that feature is the capability of modelling two-phase flows, which has always been a cutting-edge area of study for scientists and engineers, without the necessity of interface tracking or capturing which are technically cumbersome in traditional CFD methods.

One of the shortcomings of LBM is its instability during simulation of high velocity flows because of the appearance of negative distribution functions on the lattice. This issue limits LBM to the application of the flows at a small range of Reynolds numbers. Since the H theorem is not satisfied by employing quasilinear and BGK collision approach, there are no constraints to enforce distribution functions to have positive values on every node on the lattice all time. This disadvantage triggers a series of studies to define an H theorem on the lattice to make LBM unconditionally stable. Yong and Luo [101] have precisely shown that the LBMs based on polynomial equilibria do not satisfy H theorem. There have been many efforts to find an equilibrium distribution that satisfies H theorem which is non-polynomial, e.g. exponential [102]. The function must have same terms of Taylor expansion at the lowest order as polynomial equilibria. Therefore, these non-polynomial functions always compromise the mass and momentum conservation or make the method implicit which increase computational cost, reduce the accuracy, or create other spurious effects [101].

Once the BGK-LBM is applied to simulate a thermal fluid, Prandtl number ($\mathrm{Pr} = \nu / \alpha$ is the ratio of momentum diffusivity or kinematic viscosity to thermal diffusivity) is unity since BGK-LBM uses single relaxation time (SRT). The Multiple-relaxation-time (MRT) proposed by d'Humières [103, 104] introduced the relaxation times corresponding to the evolution of each macroscopic property. In fact, it is a more general form of LBM reflecting the physics with a collision matrix where moments of distribution functions for density and momentum are relaxed with different time scales. It also removes the limitation of a unity Prandtl number in the SRT. In general, the MRT-LBM is more numerically stable than SRT LBM [103, 105] and changes the limitation of minimum velocity directions of 3D lattices to D3Q13 [104]. Lallemand and Luo [105] and d'Humières et al. [103] developed MRT-LBM equations in two-dimensions (2D) and three-dimensions (3D). MRT method has been widely used in different areas of LBM to enhance its capability to simulate more complex flows, such as turbulence flow [106], flow in porous media [107], two-phase flow [108]. Luo et al. [109] showed that at least three independent relaxation times for shear viscosity, bulk viscosity and bounce-back boundary condition are needed to strengthen the accuracy,

efficiency, and stability of the method [109]. The MRT has introduced more flexibility to the LBM [5] in one hand, meanwhile, brings 10-20% more computational cost [105] and coding difficulties in comparison with the LBM of SRT with BGK collision.

1.4 Lattice Boltzmann for multiphase flow

The lattice Boltzmann equation (LBE) was originally developed for ideal gases [86]. Further efforts have been made to describe the non-ideal gases (i.e., all types of fluid) and model the interfacial interactions of multiphase or multicomponent flows [110-113]. The importance of the work is highlighted when a Van der Waals-like EOS is employed which triggers phase separation in the computational domain. This potential, in fact, is considered as one of advantages of the LBM over the traditional CFD methods which allows defining meaningful kinetic interactions to reproduce multi-phase flows without the need for advecting and tracking the interface. The most significant attempts can be categorised into four branches: RK model, free-energy model, HSD model, and pseudopotential model which are discussed in the following subsections. The models based on RK model define a secondary collision operator which only applies on the interface and separates the phases from each other. Free-energy models incorporate Cahn-Hillard's model. Shan-Chen models employ an explicit interaction force between nodes to trigger phase separation. HSD models define the force as the gradient of a potential field. It should be noted that in this study "interface" means a numerical interface which is diffuse in comparison with a physical interface which is sharp in between two phases at mesoscopic and macroscopic scale.

1.4.1 RK model

The first approach is the RK model by Gunstensen and Rothman [112] for immiscible fluids which is developed based on the work of Rothman and Keller [114]. A perturbation in the collision operator causes the pressure tensor to be anisotropic, i.e., creates surface tension at the interface of two phases. The Blue and Red labels are assigned to the particles of one phase and another; after calculating collisions of each phase separately, a two-phase collision happens to construct the interface between two phases. At the end, a recolouring step is considered to conserve mass of each component. Despite these actions near the interface, it preserves basic lattice

Boltzmann equation in homogeneous regions. Although the model has Galilean invariance, it suffers from a lack of thermodynamic basis and microscopic physics [115]. Moreover, it is computationally inefficient in the 3D domain and only restricted to model fluids with same densities and viscosities. The method has been extended by Grunau et al. [116] to handle different viscosities and densities ratios up to 10. The N-S equations can be recovered from this system with the advantage of setting viscosity, density ratio, and surface tension independently. Reis and Phillips [115], by changing two-phase operator, showed that the model can deal with higher density ratios, reportedly 18.5. However, this approach has the 'lattice pinning' problem which means, in a slow flow regime, recolouring step cannot recognise diffusion from convection and make the interface stagnant. In order to tackle the lattice pinning issue, Latva-Kokko and Rothman [117] proposed a recolouring scheme which establishes a symmetric distribution of red and blue particles around the interface. Leclaire et al. [118] then combined the algorithm Latva-Kokko and Rothman [117] with the two-phase method of Reis and Phillips [115] which provides more improvements in the accuracy of surface tension magnitude and reducing spurious currents. The recent report [115] shows that the method is capable of simulating viscosity ratios as high as 10^4 in the case of the layered Poiseuille flow.

1.4.2 Free-energy model

The second method of the LBM for two-phase flow is the free energy (FE) approach proposed by Swift et al [113, 119]. It benefits from a free energy function that models surface tension in a thermodynamically consistent way. Herein, total density ρ and density difference $\Delta\rho$ are the input parameters of the system, instead of density of each phase separately. Two different distribution functions are assigned to them to calculate the evolution of density distribution in the simulation domain with the SRT LBE. The FE model enjoys physical basis and conserves momentum locally. The primary drawback of FE model is the lack of Galilean invariance which has been addressed by References [120-124], the outcome of these efforts is to recover Galilean invariance to the second order by entering density gradient terms into pressure tensor. Wagner [124] identified the higher order terms which are responsible for thermodynamic consistency

in FE method. Zheng et al. [125] developed a new method based on FE approach which could simulate systems with density ratios as high as 1000.

1.4.3 HSD model

He, Shan and Doolen (HSD) [126] model was developed as a modification of SC model. This model links to kinetic theory of dense gases by mean-field approximation. Therefore, it is thermodynamic consistent and can reproduce Maxwell equal area [127]. The physics of capillary can be incorporated into the model by the gradient of density term, $\kappa\nabla\nabla^2\rho$, and surface tension strength can be adjusted by parameter κ. The main limitation of the scheme is its weak numerical stability [127]. The two-component extension of HSD model was proposed by He, Chen, and Zhang (HCZ) [41] which is applicable to incompressible multiphase flow. Two sets of distribution functions are applied; one for calculating pressure and velocity fields with the aid of artificial compressibility and another for capturing the interface. It is in nature close to front capturing in traditional CFD methods as an index function ϕ, acts similar to VOF or Level set function. Based on these models, Lee and Lin [128] introduced a new discretization scheme to increase the stability of the LBE where could handle the density ratio of 1000.

1.4.4 Pseudopotential (Shan-Chen) model

Among all multiphase approaches for the LBM, pseudopotential or Shan and Chen (SC) model [110, 111] has been extensively used to study two-phase flows, due largely to its straightforward definition and simple implementation, for example, gravitational fall of a drop on a surface [129], flow over structured surfaces including gas bubbles [130], high density ratio systems [131], two-phase flow in porous media [94], the contact angle of a two-phase fluid on a solid surface [132, 133], droplet including nanoparticles and surfactant in shear flow [134], and nucleate boiling [135].

The SC model incorporates a coarse-grained lattice interaction into the LBE model. A potential, which is indirectly a function of spatial coordinate through density, namely pseudopotential, is utilised to calculate the interaction forces. Then, the forces accelerate the fluid particles, which change the equilibrium velocity of a node. The outcome is the phase separation through merely one governing equation or lattice.

1.5 Challenges for pseudopotential model

The original pseudopotential or Shan-Chen model, at first, seemed so promising: simulating two-phase system through only one equation without the need of solving Poisson's equation and finding or approximating the phase interface. However, the model has several shortcomings, such as large spurious velocities, unstable at high density ratios (limited to density ratios of the order of 10) [110], thermodynamically inconsistent with practical EOSs [131], vapour-liquid equilibrium densities are dependent on viscosity [136], and interface thickness and interface tension cannot be tuned independently. Addressing such issues is the core motive for many researchers in the LB community.

When simulating a two-phase LB system, vortex-like currents or spurious velocities at the interface of two phases are observed that have no physical sense. Regardless of the method, they are inherent in all two-phase LB models to various degrees [137]. Spurious velocities are the outcome of an imbalance between discretized forces and they increase with density ratio and interface tension [138]. Shan [139] has proved that the main source of these velocities is the non-isotropic part of the forces on the lattice. Sbragaglia et al. [140] showed that increasing the grid refinement twice can help to reduce spurious velocities 10 times at density ratio of 60.

Yuan and Schaefer [131] packed a practical EOS in a single interaction pseudopotential to utilise the van der Waals loop for setting up a two-phase system. They used several cubic EOSs such as van der Waals (VW), SRK, Carnahan-Starling (CS), and PR. This idea is great as the temperature can be defined implicitly through the EOS in the multiphase system. They showed that the CS EOS and PR EOS can lessen spurious currents significantly, enhance the stability of the model, and reach the density ratios in the order of 1000. Their proposed scheme is the basis for many extensions which are reviewed in the following sections. The details of the scheme are described in section 2.6.1.

Having only one parameter G to set the interaction force, SC model does not have the flexibility of tuning surface tension independent of EOS. In order to overcome this issue, Sbragaglia et al. [140] introduced multirange pseudopotential scheme where two

different amplitudes are employed for calculation of the force: one for nearest neighbours and another one for the next-nearest neighbours. This feature mathematically supported by Shan [141]. Huang et al. [136] found that attraction parameter of CS EOS can control the interface width.

Falcucci et al. [142] proposed a mid-range interaction approach, two-belt model, which could lessen spurious currents by one order of magnitude in comparison with original SC model at density ratio of 50. They could reach a liquid-gas coexistence system with density ratio of 500.

Through an admirable work, Li et al. [143] showed that changing surface tension through multirange pseudopotential causes the equilibrium densities to change. They added a source term to the LB equation that affected only the interface region and could add a tunable surface tension to the pseudopotential model.

1.5.1 The need for a thermodynamically consistent scheme

A major concern about the SC model arises from its thermodynamic inconsistency caused by the discretization effect of the lattice. The simulated systems recover slightly different liquid and vapour densities, in comparison with analytical solutions obtained from the Maxwell equal-area rule. This discrepancy increases as the temperature decreases and recedes from the critical point. The deviation indicates a lack of energy conservation in the SC model [144].

The aforementioned issue was first noticed by Shan and Chen [110], and the pressure tensor on the lattice, they found, gives rise to a mechanical stability that only meets the Maxwell thermodynamic condition if the pseudopotential is set to $\psi = \psi_0 \exp(-\rho_0 / \rho)$, where ρ is density, and ρ_0 and ψ_0 are arbitrary constants. In this study, mechanical stability is the essence of having $\nabla \cdot \mathbf{P} = 0$ along a stationary flat interface where $\mathbf{P}$ is the pressure tensor.

He and Doolen [145] further pointed out that the pseudopotential must be proportional to density, i.e. $\psi \propto \rho$, if the continuum integration approach is applied to calculate the

non-ideal part of the pressure. Such treatment, which attempts to resolve the thermodynamic consistency, stimulates an unrestrained accumulation of density in the liquid phase and leads to mass collapse [132, 145] and, subsequently, a gauge invariance in the pressure tensor [140]. Shan [141] then proposed a more general approach to address the pressure tensor on the lattice and found that the pseudopotential, expressed as $\psi = \psi_0 \exp(-\rho_0 / \rho)$, is thermodynamically consistent. This pseudopotential was then discovered to be associated with increase in numerical instability and spurious velocities in practice [146].

By using Shan's approach [141], Sbragaglia and Shan [147] eventually confirmed that the SC model coincides with a free energy model when the pseudopotential is given by $\psi = \left(\rho / (\varepsilon + \rho)\right)^{1/\varepsilon}$, where ε is a constant depending on the lattice. This function is self-bounded and, hence, the distribution function is prevented from accumulating excessively. It is not difficult to find that the pseudopotential $\psi = \left(\rho / (\varepsilon + \rho)\right)^{1/\varepsilon}$ coincides with the exponential function when only nearest-node interactions are considered. This approach was later introduced to multicomponent systems by Sbragaglia et al. [148].

Numerical tests [141, 147] demonstrated that the exponential-based pseudopotential could successfully simulate the liquid-vapour coexistence. However, it has also been noticed that the pseudopotential lacks sufficient free parameters to represent necessary two-phase properties such as saturation pressure, saturation densities, and speeds of sound in liquid and vapour for an LB system. In other words, the simplicity of its mathematical format and the EOS, which it presents, prevents the approach from covering a wide range of real fluids. In this regard, another approach has been proposed to simulate the real fluids by implementing practical EOSs in the LBE, while attempts were made to satisfy as largely as possible the Maxwell equal-area rule. Yuan and Schaefer [149] examined different EOSs by implementing selected EOSs directly into the SC pseudopotential model and showed that the stability and accuracy of simulations were significantly affected. Assuming the pseudopotential as $\psi \propto \rho$, Zhang and Tian [150] set EOS of the LBE via an equilibrium distribution function; however, the approach created larger spurious velocities in comparison with the original SC model

and does not guarantee the Galilean invariance [151]. Sbragaglia et al. [140] introduced a multirange pseudopotential approach, which, besides the SC forcing term, employs a second forcing term acting on the node of interest in the lattice with the aid of information from the next-nearest neighbours. The approach and its sequels [142, 152-155] are successful in increasing numerical stability and tuning surface tension independent of density ratio and can be considered as an improved scheme of an inconsistent pseudopotential LB framework. Kupershtokh et al. [129] proposed a model that combines two approaches: local approximation and mean-value approximation; the effect of each part is determined by trial and error to remove the thermodynamic inconsistency. Huang et al. [136] used the force calculation scheme of Sbragaglia [140] and, by trial and error analyses, found coefficients of the interaction force that result in an appropriate representation of the system. Colosqui et al. [156] changed the spinodal region of EOS to eliminate the numerical error due to discretization on the lattice, for which, however, an iterative feedback loop (self-tuning procedure) has to be adopted during the simulations. Li et al [143, 151] proposed a new forcing scheme, in addition to recovering correct hydrodynamics, which improved the numerical stability; however, the thermodynamic inconsistency has not been completely removed, and, for each individual case, the mechanical stability solution must be fitted with the solution given by the Maxwell equal-area rule.

In Chapter 3, we propose multipseudopotential interaction scheme for the LB pseudopotential models that is fundamentally consistent with thermodynamics and has a greater flexibility in setting a desired thermodynamic state. We demonstrate the applicability of the scheme in representing thermodynamic states of interest through simulations of planar interfaces and buoyancy-free droplets of two real fluids. Additionally, it is posited that the proposed methodology provides the potential to improve the LBE for modelling multiphase flows by mitigating the unphysical side effects, such as spurious velocities. We also discuss the possible reasons behind the common problems of collapsing simulations in practical applications when an EOS of a real fluid is implemented directly into the SC model. We finally provide the suggestions on setting the boundary conditions for the proposed multipseudopotential interaction scheme.

1.5.2 Multipseudopotential scheme extended

While in the first version of the multipseudopotential scheme, discussed in Chapter 3, the forces are determined to achieve a specific thermodynamic coexistence of interest. The scheme becomes very versatile if they are analytically set to represent cubic equations of state in a wide range of temperatures. This is the motivation for the extension of the multipseudopotential scheme.

It is found that the different forcing schemes (the ways in which the SC force is inserted in the LB equation) affect pressure tensor, thermodynamic consistency, and stability of the simulated system differently [136, 151, 157]. These studies, adopting the CS EOS, showed that the forcing schemes proposed by Guo et al. [158] and He et al. [159] can similarly recover the N-S equations to the second order and they reproduce the predicted interface tensions well. Moreover, these forcing schemes [158, 159] and exact difference method (EDM) [129] could effectively separate VLE densities from the change of viscosity. However, while EDM can reach to the density ratio of about 1000, the forcing schemes of Ref. [158, 159] can reach density ratio of about 100. Wagner [124] compared the two methods of simulating non-ideal fluids: force method [145] and pressure method [120]. After successfully identifying spurious interfacial terms with the aid of Taylor expansion to fifth order and removing them from the pressure tensor in the force method, both pressure method and force method showed similar consistent results. Li et al. [160] showed that the forcing scheme proposed by Wagner [124] is identical to the one proposed by Guo et al. [158]. Li et al [151] successfully identified the effective part of EDM, which improves the instability, and implemented it into forcing scheme proposed by Guo et al. [158] to reach higher density ratios (with the aid of the CS EOS), and then used a free parameter to approximately fit the mechanical stability on the solution of the Maxwell equal-area. They further combined the scheme with Multi-relaxation-time LB to improve the numerical stability [161]. The study showed that the interface thickness can be controlled by attraction parameter of the CS EOS. Lycett-Brown and Luo [162] analysed the LB with a general forcing scheme with the aid of Taylor expansion to the third order and used the third-order errors to counteract the thermodynamic inconsistency. They concluded that the scheme can simulate arbitrary density ratios and increasing interface width can improve the thermodynamic consistency. However, it is inevitable for the methods to fit mechanical

stability on the Maxwell construction for the entire coexistence curve or a specific thermodynamic state.

In Chapter 3, we show that using single pseudopotential to recover practical EOSs can cause non-physical interactions to happen in the simulation domain and, moreover, the mechanical stability of the system is significantly affected by the lattice scaling and type and parameters of EOSs. Such a behaviour can be found in Ref. [162], where increasing the attraction parameter of the EOS while favouring shortening the interface width, the vapour equilibrium density is considerably affected even at relatively low-density ratios. Furthermore, we have introduced a multipseudopotential scheme which is thermodynamically consistent and can be initialized with the desired VLE state, independent of lattice spacing and the type of EOSs being recovered at least at low-density ratios.

In Chapter 4, we propose a multipseudopotential scheme to incorporate most of the popular cubic EOSs into the LB equation consistently. While in Chapter 3 forces are determined to achieve a specific thermodynamic coexistence of interest, in this study they are analytically set to represent cubic equations of state including VW, CS, PR, and SRK in a wide range of temperatures. It is shown that the scheme is numerically stable and high-density ratios are achievable. Assigning each part of EOSs (attraction and repulsion) to the consistent pseudopotentials is discussed. The EOS parameters that govern the interface width are identified and applied to improve the accuracy of VLE simulations at very high-density ratios. The simulation results are supported by theoretical analysis which helps to present them in reduced formats and to link them to real world thermodynamic systems.

1.5.3 Boundary condition for pseudopotential models

Setting up proper treatments at the boundaries of the simulation domain is necessary to achieve the desired correct results while satisfying the given flow conditions, such as velocity, pressure, or periodic planes. The treatments should keep the accuracy of the solution at a minimum computational cost. In the N-S based solvers the boundary conditions are directly imposed on macroscopic quantities. However, in the LBM, similar to particle-based methods such as MD and DPD, the microscopic characteristics

give rise to the desired macroscopic flow conditions. After a streaming process, the distribution functions of a boundary node should be defined. This requires redefining all of them, or only the unknowns, as the node has some defined particle populations, coming from the inside of the domain.

It has been well-studied, and proven, that the conventional LBM has the second order of accuracy, in phase space inside of the flow domain [91, 163]. Therefore, a proper boundary treatment should provide the same, otherwise degrading the entire simulation accuracy. For example, bounce back scheme, implemented in lattice gas automaton method for straightforward treatment of no-slip boundaries, is found to have the first order of accuracy in the LBM [164, 165]. The scheme could be of the second order if the wall line is considered to be halfway between the fluid and solid nodes [166].

The extrapolation treatments are able to provide the second order of accuracy. The finite difference-based scheme of Chen et al.[167] requests information from two neighbouring node layers. The non-equilibrium extrapolation scheme of Zhao-Li et al. [168] needs information from the nearest fluid nodes to determine a new set of distribution functions for the nodes whose pressure or velocity is defined. To keep the great assets of local collision operations which suit parallel processing, an LBM boundary condition better finds the unknown distribution functions of a node, merely by the use of the information available at the node itself.

On the other hand, the on-site boundary condition proposed by Zou and He [169] imposes pressure or velocity condition on the focused node regardless of neighbours. It finds the unknowns with the aid of conservation of mass and momentum, and bounce back rule for the non-ideal part of distributions. Moreover, the method keeps the second order of accuracy for simulations. Inamuro et al. [170] suggested the missed distributions are found from the equilibrium distribution function that is calculated by a fictitious density and velocity. Skordos [171] filled all the distribution functions on the boundary node using the stress tensor which is related to strain rate tensor. The strain rate tensor can be evaluated by second order finite difference approximation of velocity over neighbouring nodes. Latt et al. [172] proposed replacing all the distribution functions of the boundary node by the use of a stress tensor evaluated by bounce back

of the non-equilibrium part of distribution functions. Latt et al. [172] compared boundary treatments proposed by [169-171] and found that despite the fact that they all had a second order of accuracy, the ones which determine the other unknown distributions after streaming step through closure relations have better accuracy at low Reynolds number flows. Additionally, the boundary conditions, which fill all the distributions at the boundary node, demonstrate better numerical stability. Therefore, they are suitable for high Reynolds number flows.

It should be noted that bounce back applicability is not limited by the geometry of the wall. However, the others need to find the vectors tangent and normal to the wall, for which various probable situations should be assessed beforehand. They also require further treatments for corner nodes. Bounce back has been going through considerable extensions; it is combined with spatial interpolations to handle moving boundaries [173]. Junk and Yang [174] modified bounce back to increase the accuracy of velocity and pressure fields whilst keeping the procedure completely local. Nash et al. [175] studied this category of boundary condition treatments regarding accuracy and performance in various types of flow.

In spite of the popularity, the boundary treatments for pseudopotential models have not been studied thoroughly. It has been well studied and known that adjusting the pseudopotential force at the boundaries can help defining wettability of a solid surface. However, in the case of a half-saturated porous geometry, there exist channels where a single-phase fluid is flowing and its interactions with solid should be correctly modelled. The other applications are the simulations of two-phase flows in which some solid walls are merely interacting with one phase such as the flow regimes of slug, annular and dispersed, in a pipe. During this, one phase flows in the center of the pipe and the other one is interacting with the pipe wall.

In Chapter 5, we implement different solid-liquid force interactions into the bounce-back and on-site Zou and He [169] treatments, to build non-slip wall boundary conditions. We assess these methods for a single-phase real fluid (the compressed water) flows in a two-dimensional channel, to recover macroscopic poiseuille flow. The accuracy of simulations, density variation, and velocity profiles due to these treatments

are studied. We demonstrate that the choice of solid-liquid interaction can effectively change the flow behaviour.

1.6 Conclusion and research goal

We reviewed the most popular methods in simulation of multiphase flows at various scales. MD is the paramount choice for modelling individual molecules or atoms where different molecular interactions give rise to phase separation. Each DPD particle simulates a cluster of molecules which moving randomly in computational domain, therefore, they cover a scale between molecules and macroscopic. Continuum scale models mostly employ the N-S equations where phase interface should be identified by a secondary method such as VOF, level-set, and front-tracking method. The LBM shows the characteristics of both macroscopic and molecular levels. The particles are moving on a lattice which produce noise-free results, conserve mass and reproduce the N-S equations to the second order.

The well-known multiphase models in the LBM are the RK, Free-energy, HSD, and pseudopotential model. Among them, pseudopotential model is popular due to ease of use and the meaningful physics based on underlying molecular interactions. While employed in many applications, it suffers from thermodynamic inconsistency, being limited to low-density ratios, and unable to control interface width independent of EOS. Moreover, the model has been studied for modelling wettability phenomena but the effect of solid-fluid interactions on bulk flow is missed in the literature. These shortcomings are the main core motive of this study to develop a new LBM multiphase model, multipseudopotential interaction, with boundary conditions.

Chapter 2 – Pseudopotential model for lattice Boltzmann method

2.1 Introduction

Pseudopotential or SC model in the lattice Boltzmann framework has been a simple and successful route for simulating multiphase flows. In this chapter, firstly Boltzmann equation and its relation to the LBM is studied. Then, the N-S equations are derived from the LBM. After covering the basics, different aspects of the pseudopotential model are studied in detail. The common way in reproducing practical EOSs is described. The isotropy of the SC force, as an element for decreasing spurious velocities and linking to macroscopic equations, is investigated. Thermodynamic consistency of the model from two different points of view is assessed. Multirange pseudopotential as an extension of SC force is studied. Different approaches to implementing an internal or external force to the LBM are explained.

2.2 BGK Boltzmann equation

The Boltzmann equation having the BGK collision is

$$\frac{df}{dt}+\boldsymbol{\xi}\cdot\nabla f=-\frac{f-g}{\tau}, \tag{2-1}$$

where $f(\mathbf{x},\boldsymbol{\xi},t)$ is the single-particle distribution function, τ is the collision relaxation time, $\boldsymbol{\xi}$ is the microscopic velocity, g is the Maxwell-Boltzmann distribution function

$$g\equiv\frac{\rho}{(2\pi RT)^{D/2}}\exp\left(-\frac{(\boldsymbol{\xi}-\mathbf{u})^2}{2RT}\right), \tag{2-2}$$

where R is the ideal gas constant, D is the number of dimensions, ρ is density, $\mathbf{u}$ is macroscopic velocity, T is temperature. The macroscopic properties are linked with microscopic ones through moments of the distribution function [176]

$$\begin{aligned}
&\rho=\int f\,d\boldsymbol{\xi}=\int g\,d\boldsymbol{\xi},\\
&\rho\mathbf{u}=\int \boldsymbol{\xi} f\,d\boldsymbol{\xi}=\int \boldsymbol{\xi}\, g\,d\boldsymbol{\xi},\\
&\rho En=\frac{D_0}{2}RT=\frac{1}{2}\int(\boldsymbol{\xi}-\mathbf{u})^2 f\,d\boldsymbol{\xi}=\frac{1}{2}\int(\boldsymbol{\xi}-\mathbf{u})^2\, g\,d\boldsymbol{\xi},
\end{aligned} \tag{2-3}$$

where ρEn is the energy and D_0 is the number of degrees of freedom a particle.

2.3 The lattice Boltzmann method

The LBM is recurring streams and collisions of a set of finite distribution functions $f_i(\mathbf{x},t)$ which reproduce the hydrodynamic behaviour. These distributions are confined to move from their positions $\mathbf{x}$ along discrete microscopic velocities $\mathbf{e}_i$ to the neighbouring discreet positions $\mathbf{x}+\mathbf{e}_i$. At each node, they collide simultaneously; in a sense, their mass and momentum are conserved. Every node tries to approach local equilibrium by delivering a part of the excess mass to the nearest neighbours. The evolution of the distribution functions is governed by lattice Boltzmann equation

$$f_i(\mathbf{x}+\mathbf{e}_i\Delta t, t+\Delta t) - f_i(\mathbf{x},t) = -\frac{1}{\tau}\Big[f_i(\mathbf{x},t) - f_i^{eq}(\mathbf{x},t)\Big] + F_i(\mathbf{x},t), \tag{2-4}$$

where $\mathbf{x}$ is the position, t the time, τ the nondimensional relaxation time, $\{\mathbf{e}_i : i = 0,...,q-1\}$ discrete microscopic velocity vectors to $q-1$ neighbouring nodes, and F_i is an arbitrary source term to introduce a correction or new capability. The link between the LBM and Boltzmann equation was not clear at first [86] but He and Luo well derived the LBM from Boltzmann equation [176] and showed that equation (2-4) can be considered as the first-order-in-time approximation of the Boltzmann equation. f_i^{eq} is the local equilibrium distribution function

$$f_i^{eq}(\mathbf{x},t) = w_i\rho\left[1 + \frac{\mathbf{e}_i.\mathbf{u}}{RT} + \frac{(\mathbf{e}_i.\mathbf{u})^2}{2(RT)^2} - \frac{\mathbf{u}.\mathbf{u}}{2RT}\right], \tag{2-5}$$

where w_i are the weights. RT is related to the sound speed, $c_s^{\,2} = RT$, in the LBM as it has an ideal gas equation of state. The sound speed depends on the lattice configuration which several examples will be given in the following. ρ and $\mathbf{u}$ are the macroscopic fluid density and velocity given by

$$\rho = \sum_{i=1}^{q} f_i\,, \tag{2-6}$$

$$\rho \mathbf{u} = \sum_{i=1}^{q} f_i \mathbf{e}_i .$$

The Lattice or mesh structure is named as $DnQq$ where n is the number of dimensions and q is the number of discrete velocity vectors. The symmetric 2D and 3D lattices which are widely used in the literature are $D2Q7$, $D2Q9$, $D3Q15$, $D3Q19$, and $D3Q27$. The $D2Q7$ is usually used in the early LB simulations

$$[\mathbf{e}_0, \mathbf{e}_1, \mathbf{e}_2, \mathbf{e}_3, \mathbf{e}_4, \mathbf{e}_5, \mathbf{e}_6] =$$

$$c \begin{bmatrix} 0 & 1 & \frac{1}{2} & -\frac{1}{2} & -1 & -\frac{1}{2} & \frac{1}{2} \\ 0 & 0 & \frac{\sqrt{3}}{2} & \frac{\sqrt{3}}{2} & 0 & -\frac{\sqrt{3}}{2} & -\frac{\sqrt{3}}{2} \end{bmatrix}. \tag{2-7}$$

in which weights are

$$w_a = \begin{cases} 1/2, & \alpha = 0 \\ 1/12, & \alpha = 1,2,...,6 \end{cases} \tag{2-8}$$

and sound speed is obtained from

$$c_s^{\,2} = RT = c^2 / 4 , \tag{2-9}$$

where $c = \Delta x / \Delta t$ is the lattice speed. In the LBM Δt is set to be unity which causes c to be representative of lattice spacing as well. Therefore, microscopic velocities and lattice nodes are coupled.

The uniform square lattices are more popular nowadays where sound speed in them is defined as

$$c_s^{\,2} = RT = c^2 / 3 . \tag{2-10}$$

The $D2Q9$ lattice is described as

$$[\mathbf{e}_0, \mathbf{e}_1, \mathbf{e}_2, \mathbf{e}_3, \mathbf{e}_4, \mathbf{e}_5, \mathbf{e}_6, \mathbf{e}_7, \mathbf{e}_8] = \tag{2-11}$$

$$c\begin{bmatrix} 0 & 1 & 0 & -1 & 0 & 1 & -1 & -1 & 1 \\ 0 & 0 & 1 & 0 & -1 & 1 & 1 & -1 & -1 \end{bmatrix}.$$

where the weights are

$$w_i = \begin{cases} 4/9, & i = 0 \\ 1/9, & i = 1,2,3,4 \\ 1/36, & i = 5,6,7,8. \end{cases} . \tag{2-12}$$

The $D3Q15$ is a lattice in which each element or box has velocities toward 8 corners and perpendicular to 6 faces besides the rest velocity

$$[\mathbf{e}_0, \mathbf{e}_1, \mathbf{e}_2, \mathbf{e}_3, \mathbf{e}_4, \mathbf{e}_5, \mathbf{e}_6, \mathbf{e}_7, \mathbf{e}_8, \mathbf{e}_9, \mathbf{e}_{10}, \mathbf{e}_{11}, \mathbf{e}_{12}, \mathbf{e}_{13}, \mathbf{e}_{14}] =$$
$$c\begin{bmatrix} 0 & 1 & 0 & 0 & -1 & 0 & 0 & 1 & -1 & 1 & 1 & -1 & 1 & -1 & -1 \\ 0 & 0 & 1 & 0 & 0 & -1 & 0 & 1 & 1 & -1 & 1 & -1 & -1 & 1 & -1 \\ 0 & 0 & 0 & 1 & 0 & 0 & -1 & 1 & 1 & 1 & -1 & -1 & -1 & -1 & 1 \end{bmatrix} \tag{2-13}$$

where the weights are

$$w_i = \begin{cases} 2/9, & i = 0 \\ 1/9, & i = 1,2,...,6 \\ 1/72, & i = 7,20,...,14 \end{cases} \tag{2-14}$$

The $D3Q19$ is obtained if, besides the rest velocity, the velocities pointing to the 18 midpoints of box edges and perpendicular to 6 faces are considered

$$[\mathbf{e}_0, \mathbf{e}_1, \mathbf{e}_2, \mathbf{e}_3, \mathbf{e}_4, \mathbf{e}_5, \mathbf{e}_6, \mathbf{e}_7, \mathbf{e}_8, \mathbf{e}_9, \mathbf{e}_{10}, \mathbf{e}_{11}, \mathbf{e}_{12}, \mathbf{e}_{13}, \mathbf{e}_{14}, \mathbf{e}_{15}, \mathbf{e}_{16}, \mathbf{e}_{17}, \mathbf{e}_{18}, \mathbf{e}_{19}] =$$

$$c\begin{bmatrix} 0 & 1 & 0 & 0 & -1 & 0 & 0 & 1 & -1 & 1 \\ 0 & 0 & 1 & 0 & 0 & -1 & 0 & 1 & 1 & -1 \\ 0 & 0 & 0 & 1 & 0 & 0 & -1 & 0 & 0 & 0 \\ -1 & 1 & -1 & 1 & -1 & 0 & 0 & 0 & 0 & \\ -1 & 0 & 0 & 0 & 0 & 1 & -1 & 1 & -1 & \\ 0 & 1 & 1 & -1 & -1 & 1 & 1 & -1 & -1 & \end{bmatrix} \tag{2-15}$$

where the weights are

$$w_i = \begin{cases} 1/3, & i = 0 \\ 1/18, & i = 1,2,...,6 \\ 1/36, & i=7,20,...,18. \end{cases} \tag{2-16}$$

Once all velocities in $D3Q15$ and $D3Q19$ are included, $D3Q27$ is constructed

$$[\mathbf{e}_0, \mathbf{e}_1, ..., \mathbf{e}_{26}] = [\mathbf{e}_0^{D3Q19}, \mathbf{e}_1^{D3Q19}, ..., \mathbf{e}_{18}^{D3Q19}, \mathbf{e}_7^{D3Q15}, \mathbf{e}_8^{D3Q15}, ..., \mathbf{e}_{14}^{D3Q15}] \tag{2-17}$$

with the weights

$$w_i = \begin{cases} 8/27, & i = 0 \\ 2/27, & i = 1,2,...,6 \\ 1/54, & i = 7,8,...,18 \\ 1/216, & i=19,20,...,26 \end{cases} \tag{2-18}$$

2.4 Boltzmann equation to LBM

The local equilibrium distribution function, $f_i^{eq}(\rho, \mathbf{u})$, is obtained from the Chapman-Enskog expansion of Maxwellian to the second-order at constant temperature [176]. The moments of single-particle distribution function (2-3) are approximated by quadrature rule to bridge Boltzmann equation to the LBM one

$$\int \phi(\xi) f(\mathbf{x}, \xi, t) d\xi = \sum_i W_i \phi(\xi_i) f(\mathbf{x}, \xi_i, t) \tag{2-19}$$

where ϕ is a polynomial function of ξ, W_i are the weights, ξ_i are the discrete velocities. For example, from equations (2-3) and (2-19) we have

$$\rho = \int f \, d\xi = \sum_{i=1}^{q} f_i \tag{2-20}$$

in which

$$f_i \equiv W_i f(\mathbf{x}, \xi_i, t) \,. \tag{2-21}$$

when the lattice is selected, the weights can be found from equality of the lattice velocity moments with its corresponding over the Maxwell distribution for particles in rest. The equality of zeroth to the third order moments is necessary to obtain Navier-Stokes equation for isothermal systems. The fourth order equality should be considered

for thermal systems. For example, considering stationary 2D equilibrium for Boltzmann equation

$$g_0 \equiv g(\rho = \rho_0, \mathbf{u} = 0) \tag{2-22}$$

and the LBM $f_{i(0)}^{eq} = f_i^{eq}(\rho = \rho_0, \mathbf{u} = 0)$, the zeroth, second, and fourth order moments are [86]

$$\sum_i f_{i(0)}^{eq} = \int g_0 d\xi = \rho_0$$

$$\sum_i f_{i(0)}^{eq} e_{i\alpha} e_{i\beta} = \int g_0 \xi_\alpha \xi_\beta d\xi = \rho_0 RT \delta_{\alpha\beta} \tag{2-23}$$

$$\sum_i f_{i(0)}^{eq} e_{i\alpha} e_{i\beta} e_{i\gamma} e_{i\delta} = \int g_0 \xi_\alpha \xi_\beta \xi_\gamma \xi_\delta d\xi = \rho_0 (RT)^2 (\delta_{\alpha\beta}\delta_{\gamma\delta} + \delta_{\alpha\gamma}\delta_{\beta\delta} + \delta_{\alpha\delta}\delta_{\beta\gamma})$$

where α and β are Cartesian coordinates. The odd moments are zero due to the symmetry of integrals. By equating very left-hand side with very right-hand side of above equations we obtain

$$\sum_i w_i = 1$$

$$\sum_i w_i e_{i\alpha} e_{i\beta} = RT \delta_{\alpha\beta} \tag{2-24}$$

$$\sum_i w_i e_{i\alpha} e_{i\beta} e_{i\gamma} e_{i\delta} = (RT)^2 (\delta_{\alpha\beta}\delta_{\gamma\delta} + \delta_{\alpha\gamma}\delta_{\beta\delta} + \delta_{\alpha\delta}\delta_{\beta\gamma})$$

Looking at equations (2-24) the dependence of temperature or sound speed to the lattice spacing is clearer. Weights are found by this set of equations.

2.5 LBM to Navier-Stokes equation

Lattice Boltzmann equation leads to the Navier-Stokes equations through multiscale analysis and Taylor expansion. Here, we explain the idea of Wagner [124, 177]. The below conditions are necessary for the derivation of an isothermal system

$$\begin{aligned}
&\sum_i f_i^{eq} = \rho \\
&\sum_i f_i^{eq}(\mathbf{e}_i - \mathbf{u}) = 0, \\
&\sum_i f_i^{eq}(\mathbf{e}_i - \mathbf{u})(\mathbf{e}_i - \mathbf{u}) = \rho\theta\mathbf{I}, \\
&\sum_i f_i^{eq}(\mathbf{e}_i - \mathbf{u})(\mathbf{e}_i - \mathbf{u})(\mathbf{e}_i - \mathbf{u}) = \mathbf{Q},
\end{aligned} \tag{2-25}$$

where $\mathbf{I} = \delta_{\alpha\beta}\mathbf{e}_\alpha\mathbf{e}_\beta$ is the identity matrix, $\mathbf{Q} = Q_{\alpha\beta\gamma}\mathbf{e}_\alpha\mathbf{e}_\beta\mathbf{e}_\gamma$ and $\{\mathbf{e}_\alpha, \mathbf{e}_\beta, \mathbf{e}_\gamma, ...\}$ with Greek indices are unit vectors in Cartesian coordinate (do not confuse them with $\{\mathbf{e}_i, \mathbf{e}_j, \mathbf{e}_k, ...\}$ having English indices which represent lattice vectors). $\mathbf{Q}$ should be a zero tensor to satisfy Galilean invariance which is not the case for many popular LBMs.

It is desirable for forcing term only changes momentum of particles by $\mathbf{F} = F_\alpha\mathbf{e}_\alpha$ but not mass conservation or higher order terms

$$\begin{aligned}
&\sum_i F_i = 0 \\
&\sum_i F_i(\mathbf{e}_i - \mathbf{u}) = \mathbf{F} \\
&\sum_i F_i(\mathbf{e}_i - \mathbf{u})(\mathbf{e}_i - \mathbf{u}) = 0
\end{aligned} \tag{2-26}$$

Comparing the first equation with the second one we immediately find

$$\begin{aligned}
&\sum_i F_i(\mathbf{e}_i - \mathbf{u}) = \sum_i F_i\mathbf{e}_i - \mathbf{u}\underbrace{\sum_i F_i}_{=0} \\
&\sum_i F_i\mathbf{e}_i = \mathbf{F}
\end{aligned} \tag{2-27}$$

and expanding the third one we obtain

$$\begin{aligned}
&\sum_i F_i(\mathbf{e}_i-\mathbf{u})(\mathbf{e}_i-\mathbf{u})=0\\
&\sum_i F_i(\mathbf{e}_i\mathbf{e}_i+\mathbf{uu}-\mathbf{e}_i\mathbf{u}-\mathbf{ue}_i)=0\\
&\sum_i F_i\mathbf{e}_i\mathbf{e}_i+\underbrace{\mathbf{uu}\sum_i F_i}_{=0}-(\sum_i F_i\mathbf{e}_i)\mathbf{u}-\mathbf{u}(\sum_i F_i\mathbf{e}_i)=0\\
&\sum_i F_i\mathbf{e}_i\mathbf{e}_i-(\sum_i F_i\mathbf{e}_i)\mathbf{u}-\mathbf{u}(\sum_i F_i\mathbf{e}_i)=0\\
&\sum_i F_i\mathbf{e}_i\mathbf{e}_i=\mathbf{Fu}+\mathbf{uF}
\end{aligned} \tag{2-28}$$

The Taylor expansion can be written for the distribution function

$$f_i(\mathbf{x}+\mathbf{e}_i\Delta t,t+\Delta t)=\sum_{n=0}^{\infty}\frac{\Delta t^n}{n!}D_i^n f_i(\mathbf{x},t)\,. \tag{2-29}$$

where D_i^n to second order is

$$\begin{aligned}
D_i^1&=(\partial_t+\mathbf{e}_i\cdot\nabla)=\partial_t+e_{i\alpha}\partial_\alpha\\
D_i^2&=(\partial_t+\mathbf{e}_i\cdot\nabla)^2=\partial_t^2+2e_{i\alpha}\partial_t\partial_\alpha+e_{i\alpha}e_{i\beta}\partial_\alpha\partial_\beta
\end{aligned} \tag{2-30}$$

and putting this into (2-4), and setting $\Delta t=1$, we have

$$\sum_{n=1}^{\infty}\frac{1}{n!}D_i^n f_i(\mathbf{x},t)=\frac{1}{\tau}\left[f_i^{eq}(\mathbf{x},t)-f_i(\mathbf{x},t)\right]-F_i \tag{2-31}$$

The order of the derivatives is shown by $O(\partial)=O(D)$. Equation (2-31), expanded to the second order, is

$$D_i^1 f_i+\frac{1}{2}D_i^2 f_i+F_i+O(D^3)=\frac{1}{\tau}\left[f_i^{eq}(\mathbf{x},t)-f_i(\mathbf{x},t)\right] \tag{2-32}$$

As a result, we can approximate f_i from its higher order derivatives and f_i^{eq}

$$f_i(\mathbf{x},t)=f_i^{eq}(\mathbf{x},t)-\tau D_i^1 f_i-\frac{\tau}{2}D_i^2 f_i-\tau F_i+O(D^3) \tag{2-33}$$

Putting this approximation into itself

$$f_i(\mathbf{x},t) = f_i^{eq}(\mathbf{x},t) - \tau D_i^1\left[f_i^{eq}(\mathbf{x},t) - \tau D_i^1 f_i - \frac{\tau}{2} D_i^2 f_i - \tau F_i + O(D^3) \right] \\ -\frac{\tau}{2} D_i^2\left[f_i^{eq}(\mathbf{x},t) - \tau D_i^1 f_i - \frac{\tau}{2} D_i^2 f_i - \tau F_i + O(D^3) \right] - \tau F_i + O(D^3) \tag{2-34}$$

and getting rid of higher-orders we find

$$f_i(\mathbf{x},t) = f_i^{eq}(\mathbf{x},t) - \tau D_i^1\left[f_i^{eq}(\mathbf{x},t) - \tau D_i^1 f_i - \tau F_i \right] \\ -\frac{\tau}{2} D_i^2\left[f_i^{eq}(\mathbf{x},t) - \tau F_i \right] - \tau F_i + O(D^3) \tag{2-35}$$

We still have f_i at right hand side, thus, we put (2-33) again inside (2-35)

$$f_i(\mathbf{x},t) = f_i^{eq}(\mathbf{x},t) \\ -\tau D_i^1\left[f_i^{eq}(\mathbf{x},t) - \tau D_i^1\left\{ f_i^{eq}(\mathbf{x},t) - \tau D_i^1 f_i - \frac{\tau}{2} D_i^2 f_i - \tau F_i + O(D^3) \right\} - \tau F_i \right] \\ -\frac{\tau}{2} D_i^2\left[f_i^{eq}(\mathbf{x},t) - \tau F_i \right] - \tau F_i + O(D^3), \tag{2-36}$$

remove higher order terms at the second line and rearrange

$$f_i(\mathbf{x},t) = f_i^{eq}(\mathbf{x},t) - \tau F_i \\ -\tau D_i^1\left[f_i^{eq}(\mathbf{x},t) - \tau F_i \right] \\ +\tau(\tau - \frac{1}{2}) D_i^2\left[f_i^{eq}(\mathbf{x},t) - \tau F_i \right] + O(D^3) \tag{2-37}$$

By this process, we show the dependency of f_i to itself through higher-order derivatives. Now we are able to find the LBE while its streaming step is approximated with the aid of the equilibrium distribution function and force term at the current time and position.

$$F_i + D_i^1\left[f_i^{eq}(\mathbf{x},t) - \tau F_i \right] - (\tau - \frac{1}{2}) D_i^2\left[f_i^{eq}(\mathbf{x},t) - \tau F_i \right] = \\ \frac{1}{\tau}\left[f_i^{eq}(\mathbf{x},t) - f_i(\mathbf{x},t) \right] + O(D^3) \tag{2-38}$$

By calculating the zeroth order velocity moments, $\sum_i$, the continuity equation is obtained

$$\partial_t \rho + \nabla(\rho \mathbf{u} - \frac{1}{2}\mathbf{F}) = O(\partial^3) \tag{2-39}$$

In which the actual fluid velocity is obtained

$$\mathbf{v} = \mathbf{u} - \frac{1}{2\rho}\mathbf{F} \tag{2-40}$$

From the first order velocity moment, $\sum_i \mathbf{e}_i$, of equation (2-38), we find Navier-Stokes equations

$$\rho \frac{\partial \mathbf{v}}{\partial t} + \rho \mathbf{v} \nabla \cdot \mathbf{v} = -\nabla(\rho\theta) + \mathbf{F} + \nabla \cdot \boldsymbol{\sigma} + \nabla \cdot R + O(\partial^3) \tag{2-41}$$

where $\sigma = \nu\rho\left[\nabla\mathbf{v} + (\nabla\mathbf{v})^T\right]$ is the stress tensor and $R = -3\nu\nabla \cdot \mathbf{Q} + O(\partial^2)$ is the excess part.

$$\nu = c_s^2(\tau - 0.5) \tag{2-42}$$

is the kinematic viscosity.

2.6 Pseudopotential model

Shan and Chen [111] proposed the model where particles experience an internal lattice-interaction force. It, resembling the gravitational force, between node $\mathbf{x}$ and $\mathbf{x}'$ is defined as

$$\mathbf{F}_{\mathbf{x}-\mathbf{x}'} = -Gw\left(\left|\mathbf{c}_{\mathbf{x}-\mathbf{x}'}\right|^2\right)\psi(\mathbf{x},t)\psi(\mathbf{x}',t)\mathbf{c}_{\mathbf{x}-\mathbf{x}'} \tag{2-43}$$

where G is the amplitude of the force, w is the weight function which decreases with distance, $\mathbf{c}$ is the vector from $\mathbf{x}$ to $\mathbf{x}'$, $\psi = \psi(\rho)$ is the potential which is not directly dependent on space but related via density; because of that it's called pseudopotential. Should we focus on node $\mathbf{x}$ having N close neighbours, the force acting on it becomes

$$\mathbf{F}(\mathbf{x},t) = -G\psi(\mathbf{x},t)\sum_{i=1}^{N} w\left(\left|\mathbf{c}_i\right|^2\right)\psi(\mathbf{x}+\mathbf{c}_i,t)\mathbf{c}_i, \tag{2-44}$$

If $G<0$, the force is attractive and if $G>0$, it acts as repulsion force. Hence, for the case of attraction force, if ψ is a function which increases with density, a small noise in a uniform system causes nodes with higher density attract neighbouring distribution functions and form a liquid phase. In contrast, the low-density regions are less eager to attract distribution functions and they form gas phase. ψ must be selected with care, since a monotonic and limitless function leads to an infinite accumulation of distributions. In other words, from a molecular point of view, it seems that hard sphere repulsive part of Lennard-Jones potential is neglected [147].

The interaction forces obey Newton's third law; whatever node $\boldsymbol{x}$ exerts on $\boldsymbol{x}'$ acts in opposite direction on itself. As the force involves neighbouring nodes, by applying that, momentum will be conserved in the whole domain, but, of course, not locally.

The first potential function used by Shan and Chen [111] was

$$\psi(\rho)=\rho_0\left[1-\exp(-\rho/\rho_0)\right] \tag{2-45}$$

and a year after that they [110] proposed a consistent pseudopotential

$$\psi(\rho)=\psi_0\exp(-\rho/\rho_0) \tag{2-46}$$

where both ψ_0 and ρ_0 are arbitrary constants. By choosing one of these potentials, from (2-44) the force exerted on each node is found. In the primitive model, it is assumed that the force simply changes the momentum of the fluid after the collision by $\tau\mathbf{F}$. Because τ is considered as the time scale of the collision. The node finds a new equilibrium velocity

$$\mathbf{u}^{eq}=\mathbf{u}+\mathbf{F}\tau/\rho \tag{2-47}$$

which is used in the LBE (2-4) with $F_i=0$. The pressure of the system at the limit $c\to 0$ was found as

$$p=\rho\theta+\frac{1}{2}G\psi^2 \tag{2-48}$$

As it can be seen $G\psi^2$ defines the equation of state, and there is no other parameter in the interaction force defined for the interface width or surface tension.

The kind of pseudopotential function, the way the force inserted into the LBE, the format of the force is the topics of many research papers. We discuss them in the following subsections.

2.6.1 Single pseudopotential interaction (SPI) for Cubic EOSs

Application of merely one forcing term (herein we name it as the single-pseudopotential-interaction (SPI) force scheme) is a common method of recovering an EOS [129, 131, 136, 151]. Following the Yuan et al. [131], the single pseudopotential, ψ^S, in the SC model can be obtained by EOS directly,

$$\psi^S = \sqrt{\frac{2[p(\rho,T)-\rho c^2/3]}{Gc^2}}, \tag{2-49}$$

where $p(\rho,T)$ can be calculated by the equations of state described in the following section. This selection of pseudopotential makes the magnitude of G non-functional, as it will be cancelled out in the calculation of the interaction force (2-44), though its sign can help to keep the radicand positive. This scheme makes it possible to impose the desired EOS directly on the interaction force and attempts to remove the ideal gas pressure created by streaming and collision of distribution functions. It is demonstrated in section 2.6.4 that, however, no practical EOSs placed into (2-50) could satisfy the thermodynamic condition. Moreover, in this SPI LBE scheme [131], the micro-velocity is usually set to unity, $c=1$, and the temperature is independently set to model different isothermal systems. As we show in the next chapter discussion, the thermodynamic equilibrium state of SPI will change with the value of c, i.e. grid refinement.

2.6.2 Isotropy of the interaction force

For an arbitrary pseudopotential function, the Taylor expansion yields

$$\psi(\mathbf{x}+\mathbf{c}_i)=\psi(\mathbf{x})+c_i^{\alpha}\psi_{,\alpha}(\mathbf{x})+\frac{1}{2!}c_i^{\alpha}c_i^{\beta}\psi_{,\alpha\beta}(\mathbf{x})+\ldots\ , \tag{2-50}$$

where $\psi_{,\alpha}=\partial\psi/\partial x_{\alpha}$. The conservative force in the continuum limit can be found by substituting (2-50) into equation (2-44) [139]

$$F_\alpha = -G\psi\left(E^{(2)}_{\alpha\beta}\psi_{,\beta} + \frac{1}{3!}E^{(4)}_{\alpha\beta\gamma\delta}\psi_{,\beta\gamma\delta} + \frac{1}{5!}E^{6}_{\alpha\beta\gamma\delta\varepsilon}\psi_{,\beta\gamma\delta\varepsilon} + \ldots \right), \tag{2-51}$$

where $\mathbf{E}$ is the rank-n tensor

$$E^{(n)}_{p_1 p_2 \cdots p_n} = \sum_i^N w\left(|\mathbf{c}_i|^2\right) c_i^{p_1} c_i^{p_2} \ldots c_i^{p_n}, \tag{2-52}$$

Isotropy of $\mathbf{E}^{2n}$ ensures the interaction force is isotropic and aligned with gradient of pseudopotential function and its derivatives, i.e.,

$$\mathbf{E}^{(n)} = \begin{cases} 0, & n \ \ odd \\ e_n c^n \Delta^{(n)}, & n \ \ even, \end{cases} \tag{2-53}$$

where e_n are arbitrary constants, c the lattice constant, and $\Delta^{(n)}$ fully symmetric tensor of the rank-n [178]. By adjusting weight function, w, it is possible to make $\mathbf{E}^{(2n)}$ isotropic to some extent, however, reaching a higher order of isotropy needs more neighbouring nodes to be in the range of the force. Shan [139] and Sbragaglia et al. [140] showed that the well-known spurious currents of SC model at the liquid-gas interface are as a consequence of the anisotropic part of the conservative force and their strength will be damped by increasing the order of isotropy.

Here we find $\Delta^{(n)}$ for the isotropy to 8$^{\text{th}}$ order, which can be used to find weights of a designed system or Taylor expansion of the force, equation (2-50). 8$^{\text{th}}$ order isotropy is the maximum isotropy can be obtained if the 2D force extends to next-nearest neighbours. We start from the definition of the function

$$\Delta^{(n)} = \Delta^{(2k)}_{p_1\ p_2 \cdots p_{2k}} = \sum_{j=2}^{2k} \delta_{p_1 p_j} \Delta^{2k-2}_{p_2 \cdots p_{j-1}\ p_{j+1} \cdots p_{2k}} \tag{2-54}$$

where p_j are Cartesian coordinates. For the second order $n=2$ and $k=1$, we find

$$\Delta^{(2)}_{p_1\ p_2} = \delta_{p_1 p_2}. \tag{2-55}$$

In a 2D system, p_j is the repetition of x and y.

$$\begin{aligned}\Delta^{(2)}_{xx} &= \Delta^{(2)}_{x^2} = \delta_{xx} = 1\\ \Delta^{(2)}_{xy} &= \delta_{xy} = 0\\ \Delta^{(2)}_{yy} &= \Delta^{(2)}_{y^2} = \delta_{yy} = 1\end{aligned} \tag{2-56}$$

Therefore, we can write them as

$$\Delta^{(2)} = [1,0,1] \tag{2-57}$$

for the fourth order $n=4$ and $k=2$

$$\begin{aligned}\Delta^{(4)}_{p_1\ p_2\cdots p_4} &= \sum_{j=2}^{4}\delta_{p_1 p_j}\Delta^{(2)}_{p_2\cdots p_{j-1}\ p_{j+1}\cdots p_4} = \delta_{p_1p_2}\Delta^{(2)}_{p_3p_4} + \delta_{p_1p_3}\Delta^{(2)}_{p_2p_4} + \delta_{p_1p_4}\Delta^{(2)}_{p_3p_2}\\ &= \delta_{p_1p_2}\delta_{p_3p_4} + \delta_{p_1p_3}\delta_{p_2p_4} + \delta_{p_1p_4}\delta_{p_3p_2}\end{aligned} \tag{2-58}$$

in the 2D case is

$$\begin{aligned}&\Delta^{(4)}_{xxxx} = \Delta^{(4)}_{x^4} = 3\\ &\Delta^{(4)}_{yxxx} = \Delta^{(4)}_{xyxx} = \Delta^{(4)}_{xxyx} = \Delta^{(4)}_{xxxy} = \Delta^{(4)}_{x^3y}0\\ &\Delta^{(4)}_{yyxx} = \Delta^{(4)}_{xyyx} = \Delta^{(4)}_{xxyy} = \Delta^{(4)}_{yxxy} = \Delta^{(4)}_{x^2y^2} = 1\\ &\Delta^{(4)}_{xyyy} = \Delta^{(4)}_{yxyy} = \Delta^{(4)}_{yyxy} = \Delta^{(4)}_{yyyx} = \Delta^{(4)}_{xy^3} = 0\\ &\Delta^{(4)}_{yyyy} = \Delta^{(4)}_{y^4} = 3\end{aligned} \tag{2-59}$$

where for the ease of reading the index notation $xx = x^2$, $yy = y^2$, $xxx = x^3$, and so forth is adopted. The result can be simply written as

$$\Delta^{(4)} = [3,0,1,0,3] \tag{2-60}$$

For the sixth order $n=6$ and $k=3$

$$\begin{aligned}\Delta^{(6)}_{p_1\ p_2\cdots p_6} &= \sum_{j=2}^{6}\delta_{p_1 p_j}\Delta^{(4)}_{p_2\cdots p_{j-1}\ p_{j+1}\cdots p_6}\\ &= \delta_{p_1p_2}\Delta^{(4)}_{p_3p_4p_5p_6} + \delta_{p_1p_3}\Delta^{(4)}_{p_2p_4p_5p_6} + \delta_{p_1p_4}\Delta^{(4)}_{p_2p_3p_5p_6} + \delta_{p_1p_5}\Delta^{(4)}_{p_2p_3p_4p_6} + \delta_{p_1p_6}\Delta^{(4)}_{p_2p_3p_4p_5}\end{aligned} \tag{2-61}$$

After expanding for 2D case becomes

$$\Delta^{(6)} = 3[\underbrace{5,\quad 0,\quad 1,\quad 0,\quad 1,\quad 0,\quad 5}_{x^6,\ x^5y,\ x^4y^2,\ x^3y^3,\ x^2y^4,\ xy^5,\ y^6}] \tag{2-62}$$

For the eighth order, $n=8$ and $k=4$, we find

$$\begin{aligned}
&\Delta^{(8)}_{p_1\ p_2\cdots p_8} = \sum_{j=2}^{8} \delta_{p_1 p_j} \Delta^{(6)}_{p_2\cdots p_{j-1}\ p_{j+1}\cdots p_8} \\
&= \delta_{p_1p_2}\Delta^{(6)}_{p_3p_4p_5p_6p_7p_8} + \delta_{p_1p_3}\Delta^{(6)}_{p_2p_4p_5p_6p_7p_8} + \delta_{p_1p_4}\Delta^{(6)}_{p_2p_3p_5p_6p_7p_8} + \delta_{p_1p_5}\Delta^{(6)}_{p_2p_3p_4p_6p_7p_8} \\
&+\delta_{p_1p_6}\Delta^{(6)}_{p_2p_3p_4p_5p_7p_8} + \delta_{p_1p_7}\Delta^{(6)}_{p_2p_3p_4p_5p_6p_8} + \delta_{p_1p_8}\Delta^{(6)}_{p_2p_3p_4p_5p_6p_7}
\end{aligned}$$

After expansion, we obtain

$$\Delta^{(8)} = 3\,[\underbrace{35,\quad 0,\quad 5,\quad 0,\quad 3,\quad 0,\quad 5,\quad 0,\quad 35}_{x^8,\ x^7y,\ x^6y^2,\ x^5y^3,\ x^4y^4,\ x^3y^5,\ x^2y^6,\ xy^7,\ y^8}] \tag{2-63}$$

Now we can calculate Taylor expansion, (2-51) to the fourth order of isotropy. Note that in it Einstein summation convention is adopted and terms are adding up.

$$E^{(2)}_{\alpha\beta}\psi_{,\beta} = E^{(2)}_{\alpha x}\psi_{,x} + E^{(2)}_{\alpha y}\psi_{,y}$$

$$\begin{aligned}
&E^{(4)}_{\alpha\beta\gamma\delta}\psi_{,\beta\gamma\delta} = E^{(4)}_{\alpha xxx}\psi_{,xxx} \\
&+E^{(4)}_{\alpha xxy}\psi_{,xxy} + E^{(4)}_{\alpha xyx}\psi_{,xyx} + E^{(4)}_{\alpha yxx}\psi_{,yxx} \\
&+E^{(4)}_{\alpha xyy}\psi_{,xyy} + E^{(4)}_{\alpha yxy}\psi_{,yxy} + E^{(4)}_{\alpha yyx}\psi_{,yyx} \\
&+E^{(4)}_{\alpha yyy}\psi_{,yyy}
\end{aligned} \tag{2-64}$$

We now expand them by α which are components of the force in x and y directions

$$\begin{aligned}
E^{(2)}_{x\beta}\psi_{,\beta} &= E^{(2)}_{xx}\psi_{,x} + \underbrace{E^{(2)}_{xy}}_{=0}\psi_{,y} \\
E^{(2)}_{y\beta}\psi_{,\beta} &= \underbrace{E^{(2)}_{yx}}_{=0}\psi_{,x} + E^{(2)}_{yy}\psi_{,y}
\end{aligned} \tag{2-65}$$

$$
\begin{aligned}
&E^{(4)}_{x\beta\gamma\delta}\psi_{,\beta\gamma\delta} = E^{(4)}_{xxxx}\psi_{,xxx} \\
&\underbrace{+E^{(4)}_{xxxy}\psi_{,xxy} + E^{(4)}_{xxyx}\psi_{,xyx} + E^{(4)}_{xyxx}\psi_{,yxx}}_{=0} \\
&+E^{(4)}_{xxyy}\psi_{,xyy} + E^{(4)}_{xyxy}\psi_{,yxy} + E^{(4)}_{xyyx}\psi_{,yyx} \\
&+\underbrace{E^{(4)}_{xyyy}\psi_{,yyy}}_{=0} \\
&= E^{(4)}_{x^4}\psi_{,x^3} + 3E^{(4)}_{x^2y^2}\psi_{,xy^2}
\end{aligned}
$$

$$
\begin{aligned}
&E^{(4)}_{y\beta\gamma\delta}\psi_{,\beta\gamma\delta} = \underbrace{E^{(4)}_{yxxx}\psi_{,xxx}}_{=0} \\
&+E^{(4)}_{yxxy}\psi_{,xxy} + E^{(4)}_{yxyx}\psi_{,xyx} + E^{(4)}_{yyxx}\psi_{,yxx} \\
&\underbrace{+E^{(4)}_{yxyy}\psi_{,xyy} + E^{(4)}_{yyxy}\psi_{,yxy} + E^{(4)}_{yyyx}\psi_{,yyx}}_{=0} \\
&+E^{(4)}_{yyyy}\psi_{,yyy} \\
&= E^{(4)}_{y^4}\psi_{,y^3} + 3E^{(4)}_{x^2y^2}\psi_{,x^2y}
\end{aligned}
$$

Note that $E^{(2)}_{xx} = E^{(2)}_{yy} = e_2c^2$, $E^{(4)}_{x^4} = E^{(4)}_{y^4} = 3e_4c^4$, and $E^{(4)}_{x^2y^2} = e_4c^4$ can be found by (2-56) and (2-59), therefore (2-51) be

$$
\begin{aligned}
\mathbf{F} &= -G\psi\left(E^{(2)}_{xx}\psi_{,x} + \frac{1}{6}(E^{(4)}_{x^4}\psi_{,x^3} + 3E^{(4)}_{x^2y^2}\psi_{,xy^2}) + \ldots\right)\mathbf{e}_x \\
&-G\psi\left(E^{(2)}_{yy}\psi_{,y} + \frac{1}{6}(E^{(4)}_{y^4}\psi_{,y^3} + 3E^{(4)}_{x^2y^2}\psi_{,x^2y}) + \ldots\right)\mathbf{e}_y \\
&= -G\psi\left(e_2c^2\psi_{,x} + \frac{1}{6}(3e_4c^4\psi_{,x^3} + 3e_4c^4\psi_{,xy^2}) + \ldots\right)\mathbf{e}_x \\
&-G\psi\left(e_2c^2\psi_{,y} + \frac{1}{6}(3e_4c^4\psi_{,y^3} + 3e_4c^4\psi_{,x^2y}) + \ldots\right)\mathbf{e}_y
\end{aligned}
\tag{2-66}
$$

which gives

$$
\mathbf{F} = -Ge_2c^2\psi\nabla\psi - \frac{1}{2}Ge_4c^4\psi\nabla(\nabla^2\psi) + \ldots \tag{2-67}
$$

Where $e_2 = 1$ and e_4 is found as [147]

$$
e_4 = \frac{1}{2}w(1) + 2w(2) + 8w(4) + 25w(5) + 32w(8) + \cdots \tag{2-68}
$$

2.6.3 He's thermodynamic consistency assessment

In the continuum mechanics, the contribution of internal force in the pressure tensor is calculated by

$$\nabla \cdot \mathbf{P}^{non-ideal} = -\mathbf{F}. \tag{2-69}$$

Hence, a straightforward approach to obtain modified pressure tensor is to integrate the above equation and add it to ideal part

$$\mathbf{P} = [\rho\theta + \frac{1}{2}Gc^2\psi^2 + \frac{1}{2}Gc^4(\psi\nabla^2\psi + \frac{1}{2}|\nabla\psi|^2)]\mathbf{I} - \frac{1}{2}Gc^4\nabla\psi\nabla\psi \tag{2-70}$$

The first two terms are the equation of state and the last term stands for surface tension part. It can be shown that this method suffers from gauge invariance, i.e., different pressure tensors can be found that satisfy equation (2-69) [140]. Moreover, the integration is taken over (2-67) which is a continuum approximation of the interaction force for the discrete lattice. Furthermore, if we compare (2-70) with the free energy model

$$\mathbf{P} = (p - \kappa\rho\nabla^2\rho - \frac{\kappa}{2}|\nabla\rho|^2)\mathbf{I} + \kappa\nabla\rho\nabla\rho \tag{2-71}$$

where κ is the surface tension parameter, $p = \rho\psi'(\rho) - \psi(\rho)$ and $\psi' = \partial\psi/\partial\rho$. We see another consequence of that assumption leads to the idea that the pseudopotential function must be proportional to density, i.e. $\psi \propto \rho$, to be thermodynamically consistent [132, 145]. Such pseudopotential can't show excluded volume of molecules, therefore, when used, the density at some point is increased monotonically and two-phase coexistence is not achievable.

2.6.4 Shan's thermodynamic consistency assessment

In order to compute non-ideal part, Shan [141] used the fundamental definition of the pressure tensor, i.e., the total force acting on a volume is equal to pressure felt at its surface

$$\sum \mathbf{P}.\mathbf{A} = \sum_x \mathbf{F}, \tag{2-72}$$

where $\mathbf{A}$ is the vector area. Therefore, the pressure corresponding to every single discreet force can be accurately calculated and the arbitrary gauge will be removed. In the case of D2Q9, if interactions range to the next-nearest neighbours, generally, they can be categorised into five different groups based on their range. The pressure tensors associated with group 1 and 2, which are as consequence of interactions with the nearest neighbours, are

$$\mathbf{P}^{(1)} = \frac{G}{2}\psi(x)\sum_{i=9}^{16} w\left(|\mathbf{c}_i|^2\right)\psi\left(\mathbf{x}+\mathbf{c}_i\right)\mathbf{c}_i\mathbf{c}_i, \tag{2-73}$$

The pressure of groups 4 and 8 includes the effect of pair interactions between the central node with its neighbours and ones between neighbours themselves

$$\begin{aligned}\mathbf{P}^{(2)} = &\frac{G}{4}\psi(x)\sum_{i=9}^{16} w\left(|\mathbf{c}_i|^2\right)\psi\left(\mathbf{x}+\mathbf{c}_i\right)\mathbf{c}_i\mathbf{c}_i \\ &\frac{G}{4}\sum_{i=9}^{16} w\left(|\mathbf{c}_i|^2\right)\psi\left(\mathbf{x}+\frac{\mathbf{c}_i}{2}\right)\psi\left(\mathbf{x}-\frac{\mathbf{c}_i}{2}\right)\mathbf{c}_i\mathbf{c}_i.\end{aligned} \tag{2-74}$$

The group 5 similar to group 4 and 8 includes two parts. The first part which related to interaction of central node is

$$\mathbf{P}^{(3)} = \frac{G}{4}w(5)\psi(x)\sum_{i=17}^{24}\ \psi\left(\mathbf{x}+\mathbf{c}_i\right)\mathbf{c}_i\mathbf{c}_i, \tag{2-75}$$

and the second part which is pair products among the nearest nodes is

$$\begin{aligned}\mathbf{P}^{(4)} = &\frac{G}{4}w(5)\Big[\left(\psi_{(1,1)}\psi_{(-1,0)}+\psi_{(1,0)}\psi_{(-1,-1)}\right)\mathbf{e}_{17}\mathbf{e}_{17} \\ &+\left(\psi_{(1,1)}\psi_{(0,-1)}+\psi_{(0,1)}\psi_{(-1,-1)}\right)\mathbf{e}_{18}\mathbf{e}_{18} \\ &+\left(\psi_{(0,1)}\psi_{(1,-1)}+\psi_{(-1,1)}\psi_{(0,-1)}\right)\mathbf{e}_{19}\mathbf{e}_{19} \\ &+\left(\psi_{(-1,1)}\psi_{(1,0)}+\psi_{(-1,0)}\psi_{(1,-1)}\right)\mathbf{e}_{20}\mathbf{e}_{20}\Big].\end{aligned} \tag{2-76}$$

where $\psi_{(m,n)} = \psi(\mathbf{x}+m\mathbf{e}_x+n\mathbf{e}_y)$.

By substituting (2-50) into Eqs. (2-73)-(2-76) and summing all equations, pressure tensor can be calculated in the continuum limit. For the case of planar liquid-gas interface where all gradients of the pseudopotential function are in one direction, for

example along the x coordinate, one can obtain it to the second order derivatives as below

$$P_{xx} = \frac{GC^2}{2}\psi^2 + \frac{GC^4}{12}\left[a_1 \left(\frac{d\psi}{dx} \right)^2 + a_2 \psi \frac{d^2\psi}{dx^2} \right],$$

$$P_{yy} = \frac{GC^2}{2}\psi^2 + \frac{GC^4}{4}\left[a_3 \left(\frac{d\psi}{dx} \right)^2 + a_4 \psi \frac{d^2\psi}{dx^2} \right], \tag{2-77}$$

$$P_{xy} = P_{yx} = 0,$$

where $a_1 = 1 - 3e_4$, $a_2 = 1 + 6e_4$, $a_3 = -4[w(5) + 4w(8)]$, $a_4 = a_3 + e_4$.

By considering mechanical equilibrium along the interface

$$\partial_x P_{xx} = 0 \tag{2-78}$$

and boundary conditions $\rho(-\infty) = \rho_{gas}$ and $\rho(+\infty) = \rho_{liquid}$, one obtains

$$\int_{\rho_{gas}}^{\rho_{liquid}} \left(p_0 - \rho T - \frac{Gc^2}{2}\psi^2 \right) \frac{\psi'}{\psi^{1+\varepsilon}} d\rho = 0. \tag{2-79}$$

To have a thermodynamic consistency, Maxwell equal area rule yields

$$\int_{\rho_{gas}}^{\rho_{liquid}} (p_0 - p) \frac{d\rho}{\rho^2} = 0, \tag{2-80}$$

where p is the pressure obtained from the equation of state. By equating (2-79) and (2-80) we find

$$\frac{d\psi}{\psi^{1+\varepsilon}} = \lambda \frac{d\rho}{\rho^2} \tag{2-81}$$

where λ is an arbitrary constant. As suggested by [147], we see the only shape of ψ which satisfy both equations at the same time is

$$\psi(\rho) = \left(\frac{\rho}{\lambda\varepsilon + C\rho} \right)^{1/\varepsilon}, \tag{2-82}$$

where C is an arbitrary constant and $\varepsilon = -2a_1 / a_2 = (6e_4 - 2)/(6e_4 + 1)$. We call this as thermodynamically consistent ψ. For the case of nearest neighbours, $\varepsilon = 0$ and

$$\psi(\rho) = e^{-\lambda/\rho}. \tag{2-83}$$

By matching (2-79) and (2-80), the equation of state of such a system is turned out to be

$$p = \rho\theta + \frac{G}{2}\psi^2(\rho). \tag{2-84}$$

2.6.5 Multirange pseudopotential for tuning surface tension

The primitive SC force basically has the minimum range; it only sees the nearest neighbours of the node of interest. What if the range is increased? Sbragaglia et al. [140] defined the following interaction force

$$\mathbf{F}(\mathbf{x},t) = -\psi(\mathbf{x},t)\sum_{i=1}^{N} w\left(|\mathbf{c}_i|^2\right)\left[G_1\psi(\mathbf{x}+\mathbf{c}_i,t) + G_2\psi(\mathbf{x}+2\mathbf{c}_i,t)\right]\mathbf{c}_i, \tag{2-85}$$

where $\psi(\rho) = \sqrt{\rho_0}[1 - \exp(-\rho/\rho_0)]$. In this force, besides the SC force, the interaction between node $\mathbf{x}$ and some of next-nearest nodes are counted as well. The isotropy of the force is not increased as the weight functions are the same for both nearest and next nearest forces. However, it introduces a new free parameter and instead of G we have G_1 and G_2. The main reason for achieving a new parameter was the introduction of tuning surface tension independent of the equation of state. Based on the continuum integration of the force, explained in subsection 0, the pressure tensor is

$$\mathbf{P} = (\rho\theta + A_1\frac{c^2}{2}\psi^2 + A_2\frac{c^4}{12}|\nabla\psi|^2 + A_2\frac{c^4}{6}\psi\Delta\psi)\mathbf{I} - \frac{1}{6}A_2c^4\nabla\psi\nabla\psi \tag{2-86}$$

where $A_1 = G_1 + 2G_2$, $A_2 = G_1 + 8G_2$. The surface tension is

$$\sigma = \int_{-\infty}^{+\infty}(P_{yy} - P_{xx})dx = -\frac{A_2c^4}{2}\int_{-\infty}^{+\infty}\left|\frac{\partial\psi}{\partial x}\right|^2 dx \tag{2-87}$$

where has the independent A_2 coefficient. However, Li et al. [143] with the use of Shan's idea, explained in subsection 2.6.4, found the below pressure tensor

$$\mathbf{P} = (\rho\theta + \frac{A_1 c^2}{2}\psi^2 + \frac{(G_1 + 6G_2)c^4}{12}\psi\nabla^2\psi - \frac{G_2 c^4}{6}\left|\nabla\psi\right|^2)\mathbf{I} + \frac{(G_1 + 6G_2)c^4}{6}\psi\nabla\nabla\psi - \frac{G_2 c^4}{3}\nabla\psi\nabla\psi \tag{2-88}$$

which means not only surface tension cannot get close to zero $G_1, G_2 \to 0$, but also change of A_2 affects the mechanical stability of the system., i.e., equilibrium densities of liquid and vapour.

2.6.6 Forcing term

There are many ways to implement internal or external forces such as the gravity, magnetic, and interparticle forces into the LBE. Here, we bring the most successful ones. The first idea is Shan and Chen [110] which is explained in section 2.6.

The second idea is the one proposed by He et al. [159] where the effect of Boltzmann equation force is interpreted as

$$\mathbf{F}\cdot\nabla_\xi f \approx \mathbf{F}\cdot\nabla_\xi f^{eq} = -\mathbf{F}\cdot\frac{\boldsymbol{\xi}-\mathbf{u}}{c_s^2} f^{eq} \tag{2-89}$$

which gives the following source term

$$F_i = (1-\frac{1}{2\tau})\frac{1}{\rho c_s^2}\mathbf{F}\cdot(\mathbf{e}_i - \mathbf{u}) f_i^{eq} \tag{2-90}$$

where the actual and equilibrium fluid velocity are defined as

$$\mathbf{v} = \sum_i f_i \mathbf{e}_i + \frac{\Delta t}{2\rho}\mathbf{F} \tag{2-91}$$

The third scheme is by Guo et al. [158] which is found by considering lattice effects and conversion of the LBM to Navier-Stokes equations to the second order

$$F_i = (1-\frac{1}{2\tau}) w_i [\frac{1}{c_s^2}(\mathbf{e}_i - \mathbf{u}) + \frac{1}{c_s^4}(\mathbf{e}_i \cdot \mathbf{u})\mathbf{e}_i] \cdot \mathbf{F} \qquad (2\text{-}92)$$

Where the actual and equilibrium fluid velocities are identical and the same as equation (2-91).

The fourth forcing term introduced by Kupershtokh et al. [129] where found from the Boltzmann equation

$$F_i = f_i^{eq}(\rho, \mathbf{u}^{eq} + \mathbf{F}\Delta t / \rho) - f_i^{eq}(\rho, \mathbf{u}^{eq}) \qquad (2\text{-}93)$$

In this scheme, the actual fluid velocity, $\mathbf{v} = \sum_i f_i \mathbf{e}_i + \mathbf{F}\Delta t / (2\rho)$, is different to the equilibrium velocity $\mathbf{u}^{eq} = \sum_i f_i \mathbf{e}_i$.

Huang et al. compared these force terms and found the first and fourth schemes are the same if terms of the order $O(F_\alpha F_\beta \Delta t^2 / \rho)$ are removed. The second and third schemes are the same if terms of the order $O(u^3)$ and higher are neglected. The choice of the forces for single phase flow is negligible. However, when multiphase systems are simulated they show different behaviours. The third scheme, Guo scheme, brings consistent results which are independent of the choice of the relaxation time, τ. For the first scheme, the original SC method, a good stability is seen but equilibrium densities and surface tension are dependent on τ. The fourth scheme, Kupershtokh scheme, causes the density ratio to be slightly affected by the change of τ while showing good stability. However, the Taylor expansion of first and fourth scheme have several extra terms in addition to Navier-Stokes ones [136].

2.7 Conclusion

It is shown that lattice Boltzmann equation can be derived directly from Boltzmann equation and Navier-Stokes equations can be recovered from them. We studied pseudopotential model in detail. SPI model as a popular choice of recovering equations of state is studied.

We showed how isotropic long-range forces, beyond nearest nodes, can be constructed. Based on this topic, the forces in the continuum limit can be found. He's strategy to study thermodynamic inconsistency of pseudopotential models is revisited where the pressure tensor is found by integration of macroscopic shape of the force. Their consistent pseudopotential is proportional to density and unable to simulate liquid-vapour coexistence. On the other hand, Shan's idea is to find pressure tensor from its basic definition on the lattice which gives rises to the different thermodynamic condition. Their consistent potential can simulate phase change. Multirange pseudopotential model as a successful extension of SC model with tunable interface tension is investigated. The most famous ways of implementing an internal and external force are explained.

Chapter 3– Multipseudopotential interaction

3.1 Introduction

Pseudopotential lattice Boltzmann models have been recognised as efficient numerical tools to simulate complex fluid systems, including those at thermodynamic equilibrium states and with phase transitions. However, when the equation of state (EOS) of real fluids is implemented, the existing pseudopotential LB models suffer from thermodynamic inconsistency. In this chapter, we present multipseudopotential interactions scheme, which is fully consistent with thermodynamics and applicable to engineering applications. In this framework, multiple pseudopotentials are employed to represent dominant interaction potentials at different extents of the mean free path of particles. By simulating van der Waals and Carnahan-Starling fluids, it is demonstrated that the MPI scheme can correctly simulate the physical nature of two-phase systems on the lattice including the continuum predictions of liquid-vapour coexistence states and the sound speeds in liquid and vapour phases. It is also shown that the lattice interactions of the MPI scheme represent underlying molecular interactions, as they vary in a broad range from strong short-distance repulsions to weak long-distance attractions during phase transitions. Consequently, MPI is proved to be a reliable LB scheme, as it avoids generating unphysical potentials in implementing the EOSs of real fluids and limiting the spurious velocities at the interface of two-phase systems. Additionally, a straightforward procedure is suggested and discussed to pre-set the MPI system with the two-phase properties of a selected fluid.

3.2 Multipseudopotential interaction scheme

Considering the unique EOS presented by the consistent pseudopotential function (2-82),

$$p = \rho\theta + \frac{1}{2}Gc^2\left(\frac{\rho}{\lambda_j\varepsilon + C_j\rho}\right)^{2/\varepsilon} \tag{3-1}$$

the system is a faithful model for the liquid-vapour coexistence. However, such a consistent system is unable to present experimental data and the practical EOSs such as those of VW and CS. This shortcoming comes, in mathematics, from the fact that only three free parameters $-G$, C, and λ – are not sufficient to describe the desired relations among the properties of real fluids in two-phase coexistence such as pressure,

liquid density, vapour density, and sound speeds in the vapour and liquid phase. To our understanding, this pseudopotential represents one part of molecular potential, and such a system lacks contributions of other parts of interparticle interactions of fluids, and, hence, it is unable to represent a wide variety of experimental data of states of real fluids.

To overcome the above-mentioned shortcoming, here we introduce the concept of the multipseudopotential interaction, in comparison with the single-pseudopotential interaction (see section 2.6.1), as the pair interactions scheme to describe the hydrodynamic properties of real fluids, under the condition that each potential satisfies the thermodynamic requirement (2-82)

$$\begin{aligned}\mathbf{F}^{total} &= \mathbf{F}^{(1)} + \mathbf{F}^{(2)} + ... + \mathbf{F}^{(n)} \\ &= \sum_{j=1}^{n} -G_j \psi_j(\mathbf{x},t) \sum_{i=1}^{N} w\left(|\mathbf{c}_i|^2\right) \psi_j(\mathbf{x}+\mathbf{c}_i,t)\mathbf{c}_i,\end{aligned} \tag{3-2}$$

where n is the number of pseudopotentials, G_j the amplitude, and ψ_j the consistent pseudopotential of the j-th part of the force

$$\psi_j(\rho) = \left(\frac{\rho}{\lambda_j \varepsilon + C_j \rho} \right)^{1/\varepsilon}. \tag{3-3}$$

Here, the interparticle potential is presented with the contributions of different parts. Therefore, as shown in Figure 3-1, for example, the interaction force between node A and its neighbours $(i = 1, 2, ..., 24)$ in a given lattice, $\mathbf{F}_{A-i}^{total}$, is composed of a set of sub-forces at various potentials, which are the functions of particle densities, i.e. the inverse of the mean free path of particles.

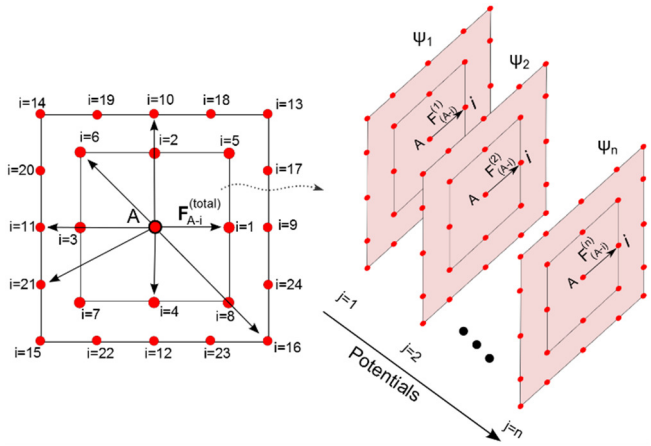

Figure 3-1. Node A and the eight nearest-neighbour nodes $(i=1,2,...,8)$ *and sixteen next-nearest nodes* $(i=9,10,...,24)$ *that it can interact with, on the D2Q9 lattice. The interaction of node A with each neighbour node,* $\mathbf{F}_{A-i}^{total}$*, is composed of a series of consistent sub-forces. Each one represents a part of the interparticle potential.*

It is noteworthy that the concept and physics of multi-pseudopotential interaction are different to those of the multi-range interaction (or pseudopotential with mid-range interactions) model proposed by Sbragaglia et al. [140] in which different set of forces are introduced to the scheme with different ranges (or cut-off radii) linking to the neighbourhood nodes. For instance, one set of forces with amplitude G_1 act on the nearest nodes and the others with amplitude G_2 act on next-nearest nodes. Such a multi-range interaction model provides capabilities for the pseudopotential models, such as flexibility of setting surface tension independent of EOS [140], achieving stable spray-like fluid [152, 154], and increasing numerical stability [142, 153]. However, it has to be noted that the multirange interaction scheme [140] does not take the thermodynamic consistency into consideration, as all of its ranges utilise the same inconsistent pseudopotential $\psi(\rho)=\sqrt{\rho_0}(1-\exp(-\rho/\rho_0))$ where ρ_0 is a constant.

As defined in (3-2) and (3-3), and discussed in subsection 3.3, the MPI scheme we proposed is fully thermodynamically consistent. Meanwhile, in principle, the MPI scheme utilises different pseudopotentials but requires the force interactions within a specific range and order of isotropy. For example, if the nearest-neighbour interactions are considered, all sub-forces only act on nearest nodes $\{\mathbf{F}_{A-i}^{j}: i=1,2,...,8\}$ and have fourth order of isotropy. Once the interactions extend to next-nearest neighbours, all sub-forces act within these lattice nodes $\{\mathbf{F}_{A-i}^{j}: i=1,2,...,24\}$ and have an eighth order

of isotropy (see Figure 3-1). Therefore, the method is grounded on the Shan's theory of calculation of exact pressure tensor in pseudopotential LB systems [141] and its extension by Sbragaglia and Shan [147].

3.3 Thermodynamic consistency analysis

Here we prove that MPI inherently satisfies thermodynamic consistency and begin with the procedure similar to that stated in Refs. [110, 141]. By employing the general rule of the force balance

$$\sum \mathbf{P}\cdot\mathbf{A} = \sum_{x} \mathbf{F} \tag{3-4}$$

[141], the pressure tensor can be exactly expressed by the MPI force on a discrete lattice for the nearest and next-nearest interactions. Taking the D2Q9 lattice, following Ref. [141], and considering the continuum limit where all gradients are in the x direction, the contribution of the total potentials of the MPI force to the pressure tensor can be calculated in the $x-y$ plane

$$\begin{aligned} P_{xx} &= \sum_{j=1}^{n} \frac{G_j c^2}{2}\psi_j^2 + \frac{G_j c^4}{12}\left[a_1 \left(\frac{d\psi_j}{dx}\right)^2 + a_2 \psi_j \frac{d^2\psi_j}{dx^2}\right], \\ P_{yy} &= \sum_{j=1}^{n} \frac{G_j c^2}{2}\psi_j^2 + \frac{G_j c^4}{4}\left[a_3 \left(\frac{d\psi_j}{dx}\right)^2 + a_4 \psi_j \frac{d^2\psi_j}{dx^2}\right], \\ P_{xy} &= P_{yx} = 0, \end{aligned} \tag{3-5}$$

where $a_1 = 1-3e_4$, $a_2 = 1+6e_4$, $a_3 = -4[w(5)+4w(8)]$, $a_4 = a_3 + e_4$, and $\varepsilon = -2a_1/a_2$.

The mechanical stability along a planar interface states that the normal component of the pressure tensor is equal to a constant pressure p_0. Hence, by adding the ideal-gas part of pressure, we find

$$p_0 = \rho\theta + \sum_{j=1}^{n}\left\{\frac{G_j c^2}{2}\psi_j^2 + \frac{G_j c^4}{12}\left[a_1\left(\frac{d\psi_j}{dx}\right)^2 + a_2\psi_j\frac{d^2\psi_j}{dx^2}\right]\right\}. \qquad (3\text{-}6)$$

This equation, unsurprisingly, is the extended version of the pressure for the single pseudopotential force model [141] with the potentials up to n-th part. It is noteworthy that e_2, which is the constant of the second-order isotropy and must appear in front of ψ_j^2 terms, is merged with G_j at a more general format. Equation (3-6) can then be rearranged in the format including only derivatives with respect to density

$$\sum_{j=1}^{n}\frac{G_j c^4\psi_j^{1+\varepsilon}}{8(1-\varepsilon)\psi_j'}\frac{d}{d\rho}\left[(\partial_x\rho)^2\frac{\psi_j'^2}{\psi_j^{\varepsilon}}\right] = p_0 - \rho\theta - \sum_{j=1}^{n}\frac{G_j c^2}{2}\psi_j^2, \qquad (3\text{-}7)$$

where $\psi' = d\psi/d\rho$. Replacing $\psi_j^{1+\varepsilon}/\psi_j'$ with ρ^2/λ_j, we are able to integrate all terms of (3-7) along the interface

$$(\partial_x\rho)^2\sum_{j=1}^{n}\frac{G_j c^4\psi_j'^2}{8(1-\varepsilon)\lambda_j\psi_j^{\varepsilon}} = \int\left(p_0 - \rho\theta - \sum_{j=1}^{n}\frac{G_j c^2}{2}\psi_j^2\right)\frac{d\rho}{\rho^2}. \qquad (3\text{-}8)$$

We can then solve (3-8) to find the density profile $\partial_x\rho$ across the interface under the boundary conditions of $\rho(-\infty) = \rho_v$, $\rho(+\infty) = \rho_l$, and $p_0 = p(\rho_l) = p(\rho_v)$. We further utilise the fact that in both liquid and vapour phases far from the interface, density has a uniform profile $\partial_x\rho$, which makes all terms on the left-hand side of (3-8) zero; therefore, we obtain, in bulk liquid and vapour,

$$\int_{\rho_v}^{\rho_l}\left(p_0 - \rho\theta - \sum_{j=1}^{n}\frac{G_j c^2}{2}\psi_j^2\right)\frac{d\rho}{\rho^2} = 0. \qquad (3\text{-}9)$$

It is obvious that (3-9) is the expression of the Maxwell construction, which means, with the first assumption that each individual force is thermodynamically consistent, the summation of these interparticle forces, therefore, is thermodynamically consistent. The corresponding EOS is

$$p = \rho\theta + \sum_{j=1}^{n} \frac{G_j c^2}{2} \psi_j^2. \tag{3-10}$$

This virial-like EOS (3-10) is the result of the multi-pseudopotential interaction forces (3-2). The MPI pseudopotential proposed in this study can be further applied to predict the interfacial forces in terms of the surface tension. In the case of a planar interface, surface tension can be calculated from

$$\sigma = \int_{-\infty}^{+\infty} (p_N - p_T) dx = \int_{-\infty}^{+\infty} (P_{xx} - P_{yy}) dx, \tag{3-11}$$

where p_N is the local pressure normal to the interface and p_T the local pressure tangential to the interface. Solving Eq. (3-11) with the condition $\partial_x \rho = 0$ again in both liquid and vapour phases far from the interface, we can obtain

$$\sigma = -\frac{c^4 e_4}{2} \int_{\rho_v}^{\rho_l} \left(\sum_{j=1}^{n} G_j \psi_j'^2 \right) (\partial_x \rho) d\rho, \tag{3-12}$$

where $\partial_x \rho$ is solved by (3-8).

Eqs. (3-10) and (3-12) are the general expressions of the EOS and the surface tension for the MPI LBE model, which are thermodynamically consistent. In physics, each potential of MPI forces provides a certain order of interparticle interactions to correct the ideal gas pressure, i.e., the first term of (3-10). In mathematics, each term has a set of free parameters to describe the detailed dynamics of physics. In addition, following the work of Sbragaglia and Shan [147], it can be straightforwardly demonstrated that the proposed MPI has the format that leads to a consistency between the lattice pressure tensor and the free energy density developed from the square gradient theory which is explained in section 3.4.

3.4 Finding free energy density

The aim of this section is to show that the pressure tensor of the MPI scheme in the case of one-dimensional interface Eq. (3-5), matches a free energy density. Following Ref. [147], we start from the free energy density [147]

$$\Xi = \Psi(\rho) + \varphi(\rho)(\partial_x \rho)^2 - l\rho, \tag{3-13}$$

where Ψ is the bulk free energy, l is a Lagrange multiplier, $\varphi(\rho)$ is a function depending only on the density. From the equilibrium equation $\frac{\delta \Xi}{\delta \rho} = 0$, it can be shown that [147]

$$-\rho^2 \frac{d}{d\rho}\left[\frac{\varphi(\partial_x \rho)^2}{\rho}\right] = p_0 - p_b, \tag{3-14}$$

where p_b is the bulk pressure. Equating the left-hand sides of (3-7) and (3-15), we find

$$\sum_{j=1}^{n} \frac{G_j c^4 \psi_j^{1+\varepsilon}}{8(1-\varepsilon)\psi_j'} \frac{d}{d\rho}\left[(\partial_x \rho)^2 \frac{\psi_j'^2}{\psi_j^{\varepsilon}}\right] = -\rho^2 \frac{d}{d\rho}\left[\frac{\varphi(\partial_x \rho)^2}{\rho}\right]. \tag{3-15}$$

By multiplying all terms by $d\rho / \rho^2$ and integrating by parts, we obtain

$$\begin{aligned} &\sum_{j=1}^{n} \frac{G_j c^4}{8(1-\varepsilon)} \left\{ \frac{\psi_j^{1+\varepsilon}}{\psi_j' \rho^2}\left[(\partial_x \rho)^2 \frac{\psi_j'^2}{\psi_j^{\varepsilon}}\right] - \int \left[(\partial_x \rho)^2 \frac{\psi_j'^2}{\psi_j^{\varepsilon}}\right] \frac{d}{d\rho}\left[\frac{\psi_j^{1+\varepsilon}}{\psi_j' \rho^2}\right] d\rho \right\} \\ &= -\frac{\varphi(\partial_x \rho)^2}{\rho}. \end{aligned} \tag{3-16}$$

Rearranging equation (3-16), the $\varphi(\rho)$ function can be determined as

$$\varphi(\rho) = -\sum_{j=1}^{n} \frac{G_j c^4}{8(1-\varepsilon)} \left\{ \frac{\psi_j \psi_j'}{\rho} - \frac{\rho}{(\partial_x \rho)^2} \int \frac{(\partial_x \psi_j)^2}{\psi_j^{\varepsilon}} \frac{d}{d\rho}\left[\frac{\psi_j^{1+\varepsilon}}{\psi_j' \rho^2}\right] d\rho \right\} \tag{3-17}$$

Since Eq. (3-15) was derived with the assumption that φ is a function of the density and not a function of the gradient of the density, the second term in the curly brackets should be zero. To enforce this condition, for all pseudopotentials we set

$$\frac{d}{d\rho}\left[\frac{\psi_j^{1+\varepsilon}}{\psi_j' \rho^2}\right] = 0, \tag{3-18}$$

$$\varphi(\rho) = -\sum_{j=1}^{n} \frac{G_j c^4}{8(1-\varepsilon)} \frac{\psi_j \psi_j'}{\rho} = -\sum_{j=1}^{n} \frac{G_j c^4}{8\lambda_j (1-\varepsilon)} \frac{\rho(\psi_j')^2}{\psi_j^{\varepsilon}}. \tag{3-19}$$

Eq. (3-18) exactly reproduces the thermodynamic condition (2-81), which demonstrates the consistency of the pressure tensor with the Maxwell equal-area rule and the free energy model. In the domain, far away from density gradients, the bulk free energy is

$$\Psi = \rho\theta \ln \rho - \theta + \sum_{j=1}^{n} \frac{G_j c^2 \rho}{2} \int_{r_0}^{\rho} \frac{\psi_j^2(n)}{n^2} dn, \tag{3-20}$$

where r_0 is a constant. Substituting (3-3) into (3-20) and calculating the integration, the bulk free energy simplifies to

$$\Psi = \rho\theta \ln \rho - \theta + \sum_{j=1}^{n} \frac{G_j c^2 \rho}{2\lambda_j (2-\varepsilon)} \psi_j^{2-\varepsilon}. \tag{3-21}$$

The bulk chemical potential can be found from $\mu = \partial_\rho \Psi(\rho)$, i.e.,

$$\mu = \theta(\ln \rho + 1) + \sum_{j=1}^{n} \frac{G_j c^2}{2} \left(\frac{\psi_j^{2-\varepsilon}}{\lambda_j (2-\varepsilon)} + \frac{\psi_j^2}{\rho} \right). \tag{3-22}$$

Therefore, the free energy is

$$\Xi = \Psi - \sum_{j=1}^{n} \frac{G_j c^4}{8\lambda_j (1-\varepsilon)} \frac{\rho(\psi_j')^2}{\psi_j^{\varepsilon}} (\partial_x \rho)^2. \tag{3-23}$$

3.5 Results and discussion

Herein, we practically analyse MPI for two-phase flows by considering a buoyancy-free steady droplet in equilibrium with its vapour and liquid-vapour coexistence with a planar interface, which is the classical case studied previously for testing the interfacial models [131, 136, 139]. The MPI capability in reproducing VW and CS EOS is thoroughly investigated in comparison with another common scheme. The scheme is verified in several ways. Firstly, according to the mechanical stability of a flat interface, the total normal component of the pressure tensor, $p_0 = P_{xx} + \rho\theta$, across the phase interface must be constant which is studied in section 3.5.4. Secondly, we expect the simulated systems give equilibrium vapor-liquid densities the same as analytical

solutions of Maxwell construction which is investigated in section 3.5.5. Thirdly, in section 3.5.8, a liquid-vapor thermodynamic state is considered; an MPI EOS is developed based on the desired system and the results of simulations and expectations are compared.

3.5.1 Equations of state

The fluids are VW and CS fluids. For VW, the EOS,

$$p = \frac{\rho T}{1-b\rho} - a\rho^2, \tag{3-24}$$

exists as the basis of many other EOSs of real fluids. Here its parameters are set as $a = 9/49$ and $b = 2/21$. The fluid's critical point (critical density $\rho_c = 1/3b$, critical temperature $T_c = 8a/27b$, and critical pressure $p_c = a/27b^2$) is deemed to be the reference point for nondimensionalization. The CS EOS,

$$p = \rho T \frac{1+\eta+\eta^2-\eta^3}{(1-\eta)^3} - a\rho^2, \tag{3-25}$$

which modifies the hard sphere repulsion part of the VW equation, is a popular EOS in the pseudopotential LB community. Here $\eta = b\rho/4$, $b = 4$ and for a two values are considered $a = 1, 5.5$. The properties of the critical point are $T_c = 0.18727a/(0.4963b)$ and $p_c = 0.18727T_c/b$. a, b values are adopted from the previous pseudopotential studies [131]. Based on critical points reduced (nondimensional) pressure, $p_R = p/p_c$, reduced density $\rho_R = \rho/\rho_c$, and reduced temperature $T_R = T/T_c$ are defined.

Weight functions are constants $w(1) = 1/3$, and $w(2) = 1/12$ [140]. The nearest-node (nodes $1-8$ in Figure 3-1) interactions are employed such that, according to (2-68), $e_4 = 1/3$ and ε approaches zero; therefore, if we set $c = 1$, from (3-3), we find

$$\psi_j^M(\rho) = \exp(-\lambda_j/\rho), \tag{3-26}$$

where the superscript 'M' indicates the pseudopotential of MPI. The choice of C does not change the shape of the pseudopotential function of (3-26). Therefore, the EOS of such a system is

$$p = \rho\theta + \sum_{j=1}^{n} \frac{G_j c^2}{2} \exp(-2\lambda_j / \rho). \tag{3-27}$$

3.5.2 Single pseudopotential and multipseudopotential interactions

Application of merely one forcing term, SPI scheme, is a common method of recovering an EOS (see subsection 2.6.1). For the SPI, the mechanical stability is characterised by the exact pressure tensor on the lattice, which is obtained from nearest-node interactions. It leads to

$$\int_{\rho_v}^{\rho_l} \left(p_0 - \rho \frac{\varsigma^2}{3} - \frac{Gc^2}{2} \left(\psi^s \right)^2 \right) \frac{(\psi^s)'}{\psi^s} d\rho = 0 \tag{3-28}$$

The thermodynamic consistency in this scheme is characterised by means of the Maxwell construction

$$\int_{\rho_v}^{\rho_l} \left(p_0 - p(\rho, T) \right) \frac{d\rho}{\rho^2} = 0, \tag{3-29}$$

which is considered the benchmark.

For the case of MPI, the mechanical stability and Maxwell thermodynamic condition are the same and identified as

$$\int_{\rho_v}^{\rho_l} \left(p_0 - \rho \frac{\varsigma^2}{3} - \sum_{j=1}^{n} \frac{G_j c^2}{2} \left(\psi_j^M \right)^2 \right) \frac{d\rho}{\rho^2} = 0. \tag{3-30}$$

Eqs. (3-28)-(3-30) are solved numerically along with the conditions $p_0 = p(\rho_l) = p(\rho_v)$, to find ρ_l, ρ_v, and p_0 for each scheme. Examining (3-30), recalling (3-27) for p_0, and knowing $\varsigma \propto c$, it can be realised that c can be crossed out from (3-30). It means that the MPI scheme under grid refinement or scalability, i.e. change of c, shows the same densities in the given equilibrium state. Nonetheless, the

mechanical stability of SPI, Eq. (3-28), is affected by the choice of c, $(\psi^s)'/\psi^s$ as is a nonlinear function of c.

3.5.3 Simulation setup

All simulations are run on a two-dimensional square lattice including nine velocities ($D2Q9$). The computational domain contains 200×200 nodes which is considerably bigger than the drop. The nondimensional relaxation time is set to unity $\tau=1$ which is the default value for most LB tests. Higher τ increases the viscosity of the system. It should be noted that τ should be $\tau>0.5$ based on equation (2-42). The internal forces are embedded in the LBE by the method proposed by Guo et al. [158], which reproduces Navier-Stokes equations to the second order. For the case of the planar interface, half of the domain is filled with liquid density and the other half with the vapour density. For the case of the curved interface, a droplet with the radius $r_0=40$ lattice unit is placed initially in the middle of the domain. The drop radius is chosen big in comparison with the interface width which occupies at least a few lattice sites. The periodic condition is applied at all boundaries. ρ_l and ρ_v are initially set, in a sense, to ensure that the system is in the saturation state. To avoid initial instability, a diffuse interface should be adopted at the beginning of simulations. We utilise the suggestion of Ref. [136]

$$\rho(r)=\frac{\rho_l+\rho_v}{2}-\frac{\rho_l-\rho_v}{2}\tanh\left(\frac{r-R}{W}\right) \tag{3-31}$$

where W controls the interface width and, in all simulations, is set at $W=5$, R is the distance between the interface and the reference point, r, is the variable distance from the reference point. For the case of the circular drop, the reference point is the centre of the drop, and for the case of the planar interface, it can be one of the boundaries parallel to the phase interface. The maximum spurious velocity $|\mathbf{u}|_{\max}$, which is a common parameter to assess the LBM force schemes [131, 136], is measured regularly during the runs of drop simulations. The error of the simulations is calculated from deviation from Maxwell construction results (3-29)

$$Error = \frac{\left|\rho_{simulation} - \rho_{Maxwell}\right|}{\rho_{Maxwell}} \tag{3-32}$$

Here the consistent pseudopotential, (3-26), is used. As the MPI EOS is scalable, as an option, we can simply set lattice temperature as the scale of a simulation and, therefore, EOS temperature T coincides with lattice temperature θ. Such a choice fixes micro-velocity at $\varsigma = \sqrt{3T}$, which is the strategy we selected in the case of the VW fluid. In order to recover VW fluid, we fit MPI EOS on to VW EOS, whereby, by trial and error, we found that four potentials in (3-27) with their free parameters, G_j and λ_j, are needed. For the case of CS fluid, we impose no constraint on ς and disconnect it from system temperature, as in the SPI scheme. We employ it only as another free parameter for fitting. Following this strategy, by trial and error in curve-fitting, we found only $n = 3$ pseudopotentials in (3-27) are needed to implement CS into MPI.

Table 3-1, Table 3-2, and Table 3-3 show the parameters we have used to fit MPI EOS on to VW and CS EOS. The fitting has been done around the two-phase coexistence region. These tables are brought, mainly, to show the capability of MPI in representing EOSs. Therefore, these values can be used directly to achieve the mentioned systems or utilised for an initial guess of curve fittings for other thermodynamic states including other EOSs or experimental data (the interested reader can contact the authors for the details). Here R^2 (R-squared) is the coefficient of determination of the curve fittings. Four potentials are found suitable for VW EOS and three for CS EOS. It should be noted that for VW EOS ς is fixed at system temperature, while it is a free parameter for CS EOS.

Table 3-1. Parameters at which MPI follows VW EOS with $a = 9/49$ *and* $b = 2/21$ *for* $n = 4$

T_R	0.78	0.82	0.86	0.90	0.94	0.98
ς	1.156	1.186	1.214	1.242	1.269	1.296
G_1	15241	8478	5336	3474	1795	1721
G_2	-2.89	-2.94	-2.790	-2.61	-3.03	-2.54
G_3	-17.2	-15.4	-13.7	-12.2	-10.8	-9.32
$G_4 \times 10^3$	-238	-283	-277	-267	-430	-415
λ_1	31.57	29.31	27.56	25.99	23.70	23.44
λ_2	1.719	1.850	1.873	1.885	2.250	2.208
λ_3	5.105	5.185	5.155	5.115	5.415	5.110
$\lambda_4 \times 10^3$	386.2	442.8	452.0	458.8	622.0	605.0
R^2	1.0	1.0	1.0	1.0	1.0	1.0

Table 3-2. Parameters at which MPI follows CS EOS with $a = 1$ *and* $b = 4$ *for* $n = 3$

T_R	0.78	0.82	0.86	0.90	0.94	0.98
$\varsigma \times 10^3$	424.8	444.4	459.0	471.3	472.4	749.6
$G_1 \times 10^3$	-126	-101	-86.1	-75.8	-88.1	-78.9
$G_2 \times 10^3$	-845	-699	-588	-497	-436	-333
G_3	156.1	114.6	85.03	64.40	36.69	577.3
$\lambda_1 \times 10^3$	61.35	56.85	55.00	54.40	64.45	33.18
$\lambda_2 \times 10^3$	196.8	187.7	181.1	175.6	183.4	168.1
λ_3	1.126	1.071	1.015	0.963	0.864	1.289
R^2	1.0	1.0	0.999	0.999	1.0	0.999

Table 3-3. Parameters at which MPI follows CS EOS with $a = 5.5$ *and* $b = 4$ *for* $n = 3$

T_R	0.78	0.82	0.86	0.90	0.94	0.98
ς	0.991	1.015	1.076	1.104	1.102	1.132
$G_1 \times 10^3$	-129.5	-122.2	-86.0	-76.54	-93.68	-88.49
$G_2 \times 10^3$	-850	-722	-588	-498	-439	-377
G_3	155.7	108.5	85.38	64.06	34.58	20.0
$\lambda_1 \times 10^3$	62.65	65.00	55.00	54.8	66.95	68.0
$\lambda_2 \times 10^3$	198	195.7	181.1	176.1	186.6	186.3
λ_3	1.124	1.051	1.016	0.962	0.854	0.777
R^2	1.0	1.0	0.999	0.999	1.0	1.0

3.5.4 Flat phase interface

The first set of simulations is run to build planar interfaces using the MPI scheme and VW EOS. As spelled out in subsection 3.3, according to the mechanical stability of a flat interface, the total normal component of the pressure tensor, $p_0 = P_{xx} + \rho\theta$, across the phase interface must be constant. Here, we can compute P_{xx} from Eq. (3-5) where $a_1 = 0$ and $a_2 = 3$ are constants for nearest interactions [141]. Second spatial derivative of pseudopotential is obtained by use of the second order central difference approximation. Figure 3-2 shows, p_0 nondimensionalized by $p_{Maxwell}$ along the phase interface for $T_R = 0.86, 0.88, 0.90$. Calculating the change of pressure along the interface $\Delta p = \left| p_0 - p_{liquid} \right| / p_{liquid}$, we estimated the maximum error of 0.011%, 0.008%, and 0.008% for each case, respectively, which validates the mechanical stability of the system. The errors are suggested to associate with higher-order terms of the pressure tensor, which are neglected in equation (3-5).

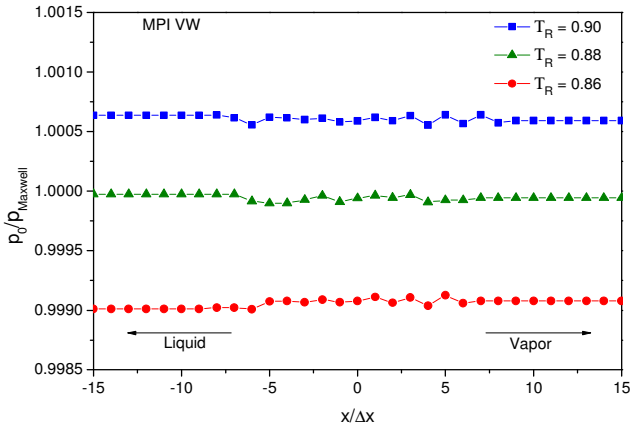

Figure 3-2. Profile of the total normal component of pressure tensor (normalized by $p_{Maxwell}$) along the phase interface for MPI scheme showing VW EOS at different temperatures.

The second set of simulations is run to investigate MPI, using CS EOS, when constructing a planar interface in comparison with SPI. Figure 3-(a) demonstrates the equilibrium (reduced) density versus (reduced) temperature achieved for the liquid branch of the liquid-vapour coexistence curve. For the case of $a=1$, SPI starts deviating from the Maxwell construction as temperature decreases. At $T_R=0.78$, the error is 1.2%. On the other hand, MPI results follow those of the liquid branch very well, where the error at $T_R=0.78$ is 0.3%. If the attraction part of CS EOS increases to $a=5.5$, both SPI and MPI show satisfactory results, though SPI simulations unconditionally collapse if temperature decreases to less than $T_R=0.84$. This is not the case for MPI, which successfully simulates the Maxwell construction at the lower temperature $T_R=0.78$. As the case of CS EOS with parameters of $a=1$ and $b=4$ has been used commonly in the literature, we deliberately have chosen $a=5.5$ and $b=4$ to show a shortcoming of SPI schemes, which will be discussed in subsection 3.5.6. The vapour branch of the coexistence curve of the CS EOS is shown in Fig. 3-(b). In the case of $a=1$, the deviation of SPI from the Maxwell construction is more severe than the liquid branch where the error reaches 79% at $T_R=0.78$. In contrast, the MPI error at that temperature is about 1%. For the case of $a=5.5$, SPI shows improvement where the error at $T_R=0.84$ is 2.6% and MPI shows 1.8%. Nonetheless, as described above, SPI collapses as temperature decreases to less than $T_R=0.84$.

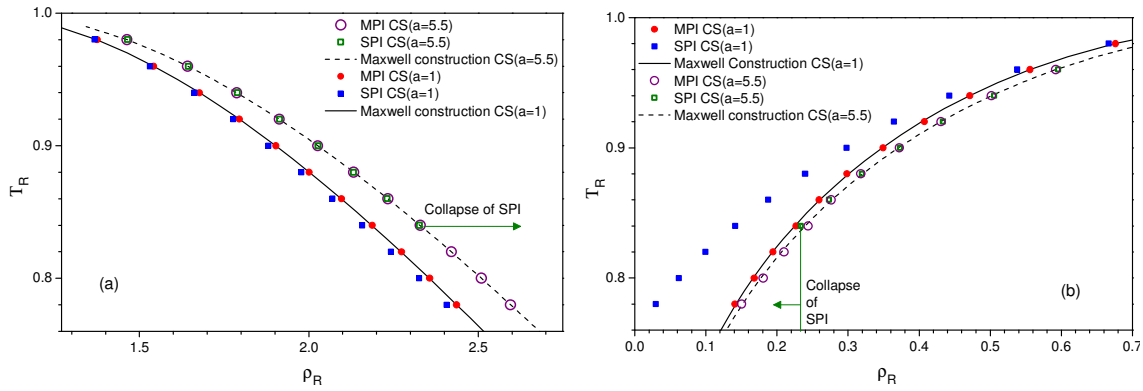

Figure 3-3. Results obtained from MPI and SPI simulations of CS EOS in comparison with analytical results of the Maxwell construction: (a) reduced density of liquid vs. reduced temperature, (b) reduced density of vapour vs. reduced temperature. The thin lines indicate where the SPI simulations collapse.

3.5.5 Circular droplet

The third set of simulations is devoted to the case of the buoyancy-free steady VW droplet. Figure 3-4 shows the reduced density of the saturated liquid and vapour versus the reduced temperature. Both schemes satisfactorily predict the liquid branch of the VW EOS, shown in Figure 3-4(a), whereby the maximum deviation from the Maxwell construction by the SPI scheme is 0.6% at $T_R = 0.92$, and by the MPI scheme, 0.4% at $T_R = 0.98$. On the vapour branch as predicted and shown in Figure 3-4 (b), the SPI scheme exhibits mechanical stability (3-28) and deviates gradually from the Maxwell construction (3-29) with decreasing temperature. It has been noticed that the SPI scheme works well with reduced temperatures larger than 0.83, but collapses when the reduced temperature decreases further the same as for CS EOS. The details on this collapse behaviour, observed as the major shortcoming of the SPI scheme, will be discussed in subsection 3.5.6. In contrast, the MPI scheme, down to lower temperatures, demonstrates good agreement with the thermodynamic condition (3-29).

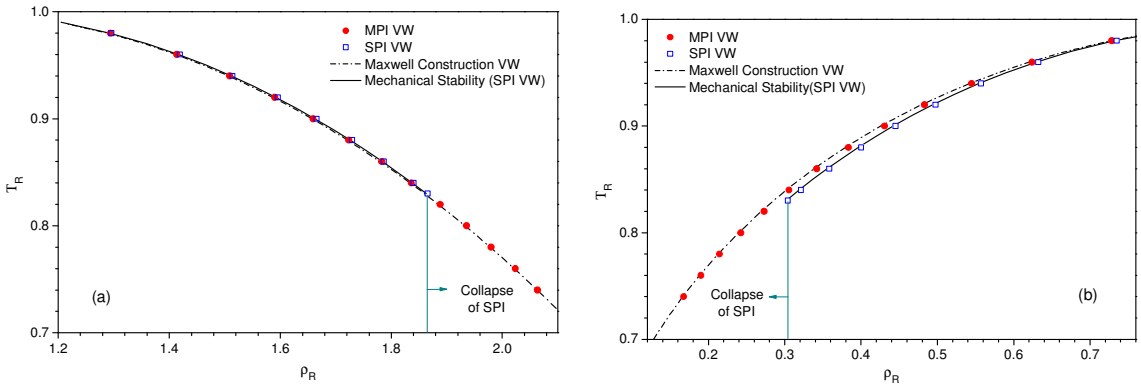

Figure 3-4. Results obtained from MPI and SPI simulations of VW EOS in comparison with analytical results of the Maxwell construction and mechanical stability: (a) reduced density of liquid vs. reduced temperature, (b) reduced density of vapour vs. reduced temperature. The vertical thin lines indicate where the SPI simulations collapse.

This behaviour can be seen clearly in Figure 3-5, which illustrates the error resulting from the deviation from the vapour branch of the Maxwell construction (3-29). Whereas the SPI scheme error increases remarkably with the decrease in temperature, the errors generated by MPI stay consistently under 1.5% and are generally independent of temperature. When temperature decreases, in principle, the liquid-vapour density ratio rises; hence, the MPI predictions are generally steady while the density ratio increases.

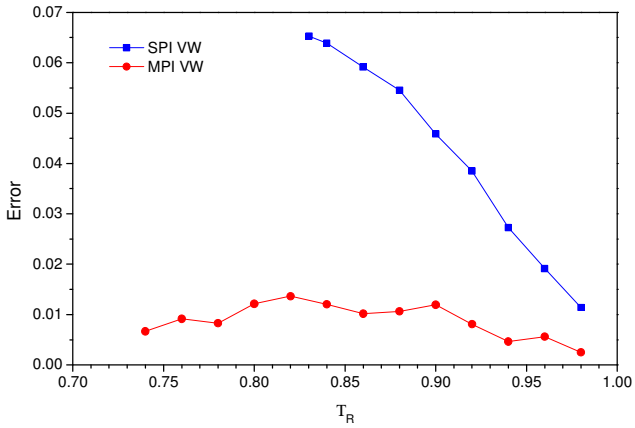

Figure 3-5. Errors due to deviation from the vapor branch of Maxwell construction. Results are obtained from MPI and SPI simulations of VW EOS.

The spurious velocities produced by the SPI (using VW EOS) and MPI (using VW EOS) schemes are examined and the results are shown in Table 3-4. Spurious velocities for both models rise as the saturation temperature decreases. The maximum spurious

velocities observed from the MPI simulations at different temperatures are about 50% of those obtained from SPI. The details are demonstrated by the distribution of spurious velocities in Figure 3-6, where both schemes are applied to simulate the VW fluid at $T_R = 0.84, 0.88, 0.94$, and the results are depicted at the same scale. The spurious velocities generated at left, right, top, and bottom of the SPI droplets are much greater than what are observed at the MPI droplets.

Table 3-4. Maximum spurious velocities of VW drop at various temperatures and their reduction levels by use of MPI over SPI.

T_R	$\lvert\mathbf{u}\rvert_{\max}^{SPI} / c$	$\lvert\mathbf{u}\rvert_{\max}^{MPI} / c$	Reduction
0.74	-	6.85E-02	-
0.78	-	2.48E-02	-
0.84	1.63E-02	8.40E-03	48.57%
0.86	1.26E-02	5.90E-03	53.02%
0.88	9.16E-03	4.45E-03	51.40%
0.90	6.32E-03	2.99E-03	52.67%
0.92	3.93E-03	1.85E-03	52.93%
0.94	2.21E-03	1.03E-03	53.50%
0.96	9.48E-04	4.34E-04	54.24%
0.98	2.19E-04	1.03E-04	52.76%

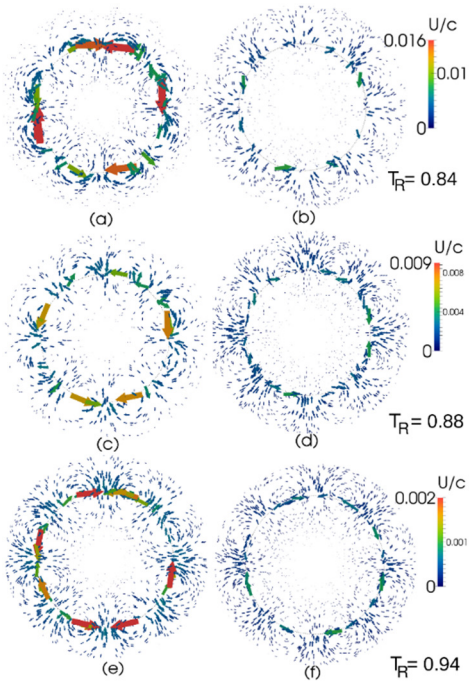

Figure 3-6. Spurious velocities are shown, SPI: (a), (c), and (e) and MPI: (b), (d), and (f), for simulating the VW fluid at different temperatures with droplets having reached the equilibrium state.

3.5.6 Physical analysis of SPI

Running different cases with the SPI scheme, we have found that LBE simulations collapse and the mechanical stability (3-28) integrations tend to diverge at low temperatures (see Figure 3-3 and Figure 3-4), where obviously spurious velocities are not the cause. The collapse of simulations for the VW fluid has been reported by Ref. [131]; however, the reasons for its occurrence was not clarified. It is in fact due to, considering Eq. (2-49), the difficulty in guaranteeing ψ^S to be a real value. For example, by setting $G<0$, ψ^S could only be a real value if $p-\rho/3\le 0$. We discuss the details by using the reduced format of the equation, $p_R-(3b/a)\rho_R$, which is depicted versus the reduced density for VW EOS at three different temperatures in Figure 3-7. It can be seen from Figure 3-7 that there are regions close to the subcooled liquid and superheated vapour where the term above is positive. If only these states are simulated, it is possible to set G as a positive value and make ψ^S physically meaningful. Nonetheless, if a saturated fluid is modelled, the change in sign of G may not be of any help. As shown in Figure 3-7, at the high temperature of $T_R=0.90$, a

physically meaningful ψ^S can be obtained for both liquid and vapour if we set $G<0$; since the term $p_R-(3b/a)\rho_R<0$. However, if temperature is reduced to $T_R<0.83$ ($p_R-(3b/a)\rho_R=0$ at $T_R=0.83$), the term $p_R-(3b/a)\rho_R$ is positive for vapour while being negative for liquid. Lower than this temperature, obviously, the SPI scheme using VW EOS fails to calculate ψ^S by (2-49) either through setting G as a positive or negative value. The threshold temperature, $T_R=0.83$, which is first identified in this study, is found by numerically solving Eq. (3-28) for the case of VW fluid with parameters $a=9/49$ and $b=2/21$. Physically, this is the reason that no results could be illustrated in Figure 3-3 (for case $a=5.5$) and Figure 3-4 from the SPI model for lower temperatures. The threshold temperature depends on the ratio of b/a for VW fluids. This means that the available domain of SPI must be investigated for a given fluid individually in order to preclude the collapse of the simulation.

It should be noted that the difficulty in guaranteeing the real value for ψ^S is a general drawback of the SPI scheme using Eq. (2-49), as long as a VW-like EOS, such as the EOSs of Peng–Robinson, Redlich–Kwong, Carnahan-Starling, is employed.

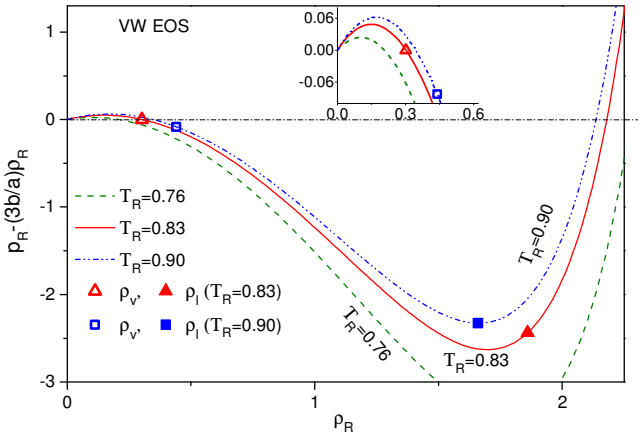

Figure 3-7. Behaviour of $p_R-(3b/a)\rho_R$, which is used to compute ψ^S, as a function of density for the VW equation.

3.5.7 Physical analysis of MPI

The LBE EOS recovers the CS EOS accurately when the proposed MPI scheme is used as shown in the inset graph of Figure 3-8. The contributions of each pseudopotential to the dynamic properties of a CS fluid is examined with the aid of the potential factors,

$$\Pi_j = \frac{1}{\rho T}\frac{G_j c^2}{2}\psi_j^2, \tag{3-33}$$

which are shown in Figure 3-8 at the reduced temperature $T_R = 0.8$ versus reduced density, which can represent the inverse of the mean free path of a particle. As demonstrated in Figure 3-8, when the density approaches zero, all potential factors approach zero and the fluid acts as an ideal gas. As density increases, Π_1, which has the nature of attraction of particles, begins to play a relatively major role in controlling the long-distance-particles (low density) interactions in the vapour region. In the interface region of liquid and vapour, Π_2, which has the nature of additional attraction of particles, gradually becomes more dominant for coupling the long-distance with short-distance (high density) interactions. Finally, approaching the liquid phase, Π_2 becomes saturated, but the relatively powerful Π_3, which has a repulsion nature of particles, dominates in simulating the short-distance interactions. While Π_1 and Π_2 act as the attraction moieties of the interactions, Π_3 reflects the hard sphere model of CS EOS. It should be noted that Π_3 is still a soft force that will be saturated in a place much higher than Π_1 and Π_2. These results demonstrate two important physical characteristics of MPI; firstly, the mass collapse (or over-accumulation of mass) is prevented by powerful repulsive Π_3, which differs from, at least, the original pseudopotential idea that the hard sphere model is achieved by the saturation of pseudopotential. Secondly, considering the fact that, here, the interactions are between nearest nodes only, all the physics of molecular short-distance repulsion and long-distance attraction are achieved without the need for increasing the LB force cut-off radius (i.e. extending the interactions to the next-nearest nodes or more). This advantage comes from the nature of MPI that the total interaction between two specific nodes is not solely attractive or repulsive. On the other hand, the physical meaning of the SPI scheme is unclear as discussed in the subsection 3.5.6. The repulsion part of the original SC model is provided by the ideal pressure created by streaming and collisions of distribution functions. This leads to the two-phase systems in which the speed of sound in liquid is less than the vapour phase and, perhaps, generates instability [129]. As shown in this work, MPI follows VW and CS EOSs well, indicating that MPI

models the sound speed of two fluids appropriately. MPI shows that in two-phase systems, in which a jump of densities exists, the multiple pseudopotentials are necessary to explain the underlying physical molecular interactions in the region of two neighbouring nodes on the lattice. Such an MPI makes it possible that the different forces take the responsibility for interparticle interactions in the different regions of the thermodynamic equilibrium state.

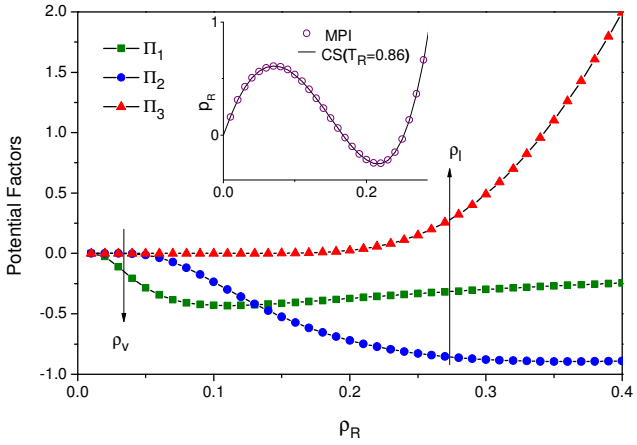

Figure 3-8. The potential factors of the MPI model contributed to the reproduction of the CS isotherm at temperature $T_R = 0.86$. The parameters are listed in Table 3-1.

3.5.8 Pre-set thermodynamic state

In subsections 3.5.5 and 3.5.4, we showed that the equation of state of MPI can be constructed by fitting on the real EOSs such as VW and CS, and, therefore, the LBE simulation system reflects the equilibrium states of those EOSs. Alternatively, a simple method rather than using curve fitting can be developed by implementing the thermodynamic conditions of liquid–vapour phase equilibrium into the MPI. Similar work has been carried out by Colosqui et al. [156], where a piecewise linear EOS is adopted. Because the pseudopotential applied in their study violates thermodynamic consistency, a self-tuning procedure was adopted during the simulations to perturb the unstable branch of the EOS and satisfy the consistency. In contrast, MPI is intrinsically consistent and capable of precisely representing the pre-set pressure tensor, as shown in Figure 3-2, without additional corrections.

Taking the VW EOS as an example, we briefly demonstrate the method of pre-setting MPI as follows. The VW fluid with the parameters $a = 9/49$, $b = 1/21$ is considered, which has the critical point of $p_c = 3$, $\rho_c = 7$, and $T_c = 1.143$. The characteristics of

the saturated fluid at temperature T such as saturation pressure p_{sat}, density of liquid ρ_l, density of vapour ρ_v, sound speed in the liquid phase $\sqrt{(\partial p/\partial\rho)_l}$, and sound speed in the vapour phase $\sqrt{(\partial p/\partial\rho)_v}$ can be determined from the EOS and employed for pre-setting the MPI LB system. Table 3-5 shows these values at $T_R = 0.80, 0.86, 0.90$. To model one of these states in an LB system, we need to impose the five characteristics mentioned above on the MPI EOS (3-27) and thus identify MPI forces.

Table 3-5. Thermodynamic properties of the saturated VW fluid with the parameters $a = 9/49$, $b = 1/21$ *and the critical point of* $p_c = 3$, $\rho_c = 7$, *and* $T_c = 1.143$.

$\frac{T}{T_c}$	p_{sat}	ρ_v	ρ_l	$(\partial p/\partial\rho)_v$	$(\partial p/\partial\rho)_l$
0.80	1.150	1.678	13.529	0.464	2.254
0.86	1.594	2.369	12.457	0.378	1.362
0.90	1.941	2.980	11.601	0.302	0.873

Here we set the lattice temperature at fluid temperature $\theta = T$, i.e. $\varsigma = \sqrt{3T}$. Therefore, the first term of (3-27) is identified. For the sake of simplicity and precluding the non-linearity of equations, only G_j are considered as unknowns in (3-27). Therefore, five pseudopotentials, $n = 5$, are considered. Based on the pattern of λ_j in VW and CS EOSs (see Table 3-1, Table 3-2, Table 3-3), we can set $\lambda_1 = m\rho_c$, $\lambda_j = 4^{j-1}\lambda_1$, and then

$$p = \rho T + \frac{3TG_1}{2}\exp(-2m\rho_c/\rho) + \sum_{j=2}^{5}\frac{3TG_j}{2}\exp(-4^j m\rho_c/2\rho) \qquad (3\text{-}34)$$

where m is a free parameter discussed in the following.

The conditions of pressure and sound speeds can constrain (3-34) and its first derivative. Generally, the pseudopotential models achieve a two-phase coexistence based on the VW loop observed in EOSs. Therefore, to have such a shape in (3-34), the

Maxwell equal-area rule (3-30) and its boundary condition are put into effect. Variable m is chosen to guarantee a VW-like loop with a single maximum pressure point and a single minimum pressure point can be created without singularity in the system of linear equations. Here, we set it as $m = 0.057$.

The system of linear equations of the pre-set MPI is derived by setting the lattice temperature at fluid temperature $\theta = T$, i.e. $\varsigma = \sqrt{3T}$, and imposing the desired conditions on MPI EOS (3-27): the saturation pressure

$$p_{sat} = \rho_v T + \sum_{j=1}^{5} \frac{3TG_j}{2} \exp(-2\lambda_j / \rho_v), \tag{3-35}$$

the sound speed in the vapour phase

$$(\partial p / \partial \rho)_v = T + \sum_{j=1}^{5} \frac{3T\lambda_j G_j}{\rho_v^2} \exp(-2\lambda_j / \rho_v), \tag{3-36}$$

the sound speed in the liquid phase

$$(\partial p / \partial \rho)_l = T + \sum_{j=1}^{5} \frac{3T\lambda_j G_j}{\rho_l^2} \exp(-2\lambda_j / \rho_l)., \tag{3-37}$$

Maxwell equal area rule (3-30)

$$p_{sat}(\frac{1}{\rho_v} - \frac{1}{\rho_l}) - T\ln(\rho_l / \rho_v) = \sum_{j=1}^{5} \frac{3TG_j}{4\lambda_j} \left[\exp(-2\lambda_j / \rho_l) - \exp(-2\lambda_j / \rho_v) \right] \tag{3-38}$$

and the boundary condition, $p(\rho_l) = p(\rho_v)$,

$$\rho_v T + \sum_{j=1}^{5} \frac{3TG_j}{2} \exp(-2\lambda_j / \rho_v) = \rho_l T + \sum_{j=1}^{5} \frac{3TG_j}{2} \exp(-2\lambda_j / \rho_l). \tag{3-39}$$

If we set $\lambda_1 = m\rho_c$ and $\lambda_j = 4^{j-1}\lambda_1$, $\{G_j : j = 1,2,3,4,5\}$ are the unknowns which can be found by solving this system of five linear equations and using the data listed in Table 3-5 for the case of this study. Therefore, MPI forces are determined and can be implemented in the LB system to achieve the desired two-phase system. Figure 3-9 shows the MPI EOS obtained via this method, in comparison with VW EOS at

$T_R = 0.86$. As we expected a VW-like loop is achieved where the MPI curve lays on the VW EOS near saturation liquid density and vapour density.

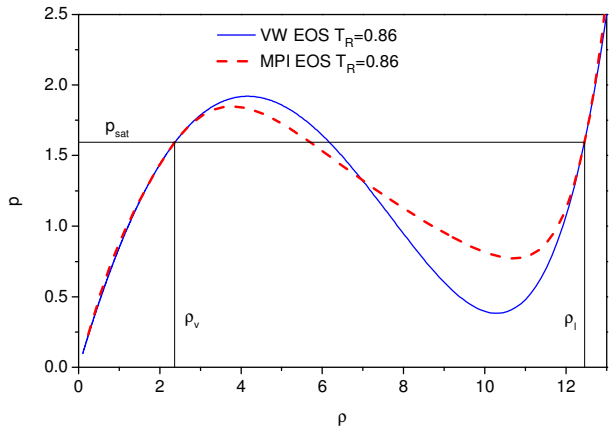

Figure 3-9. The pre-set EOS of MPI versus VW EOS at $T_R = 0.86$. In addition to creating a VW-like loop, the MPI curve mimics the VW curve in the vicinity of the saturation densities.

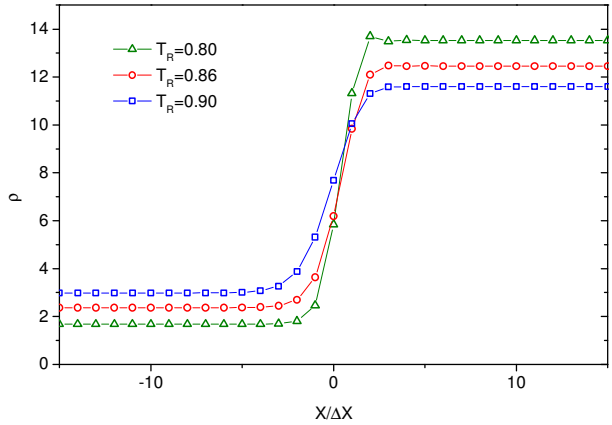

Figure 3-10. Profile of density along flat interfaces for the pre-set MPI at $T_R = 0.80, 0.86, 0.90$.

We further examined the pre-set MPI by performing simulations for the cases of the planar interface. The simulation results are given in Figure 3-10 which show the density profile along the planar interfaces. The MPI satisfactorily reproduces the input parameters. The errors due to the deviation of reproduced ρ_v and ρ_l from the input ρ_v and ρ_l are 0.002% and 0.0002% for the case of $T_R = 0.90$, 0.02% and 0.0009% for the case of $T_R = 0.86$, 0.06% and 0.001% for the case of $T_R = 0.80$, respectively. The errors should be associated with the higher-order terms of Eq. (3-5), which are

neglected, along with spurious velocities because of the lack of higher degrees of isotropy.

3.6 Conclusion

In summary, we have developed a new scheme based on the original SC model [110, 111] to eliminate the numerical errors as a consequence of the discretization effect of the lattice. In this framework, the real EOSs and experimental data can be consistently implemented into the LB system. The fundamental ingredients of the original method are preserved, while the forcing scheme is further developed to include different portions of particle interactions. The outcome EOS of the MPI scheme has a virial-like shape with an arbitrary number of terms and free parameters. Each term is assigned to a pseudopotential whose effect is dependent on the mean free path of particles.

The proposed model is compared with the commonly used SPI scheme in reproducing VW and CS EOSs and other major characteristics of two-phase flows. It is found that, first of all, in contrast to the SPI scheme, the MPI scheme is scalable and shows the independency of equilibrium densities under grid refinement. In other words, its mechanical stability condition is not influenced by the choice of the lattice spacing. Secondly, when reproducing the Maxwell construction, both methods show small discrepancies at the saturated liquid branch. Regarding the vapour branch, the SPI prediction deviates significantly with a decrease in temperature, whereas the MPI scheme shows much better results, and their accuracies are independent of temperature, the density ratio, and the type of chosen EOS.

The MPI scheme used in this work only considers the nearest-node interactions, but the interaction between two nodes is not solely attractive or repulsive. The MPI scheme adjusts the interactions automatically according to local densities. Such a behaviour can effectively reflect the underlying molecular interactions.

A shortcoming of the SPI scheme in recovering the VW-like EOSs is addressed. There exist the thermodynamic states where the SPI pseudopotential has real values in the

liquid (vapour) region and imaginary values in the vapour (liquid) region, thereby causing the collapse of simulations. This problem could be resolved by constraining the parameters of simulations by decreasing the degree of freedom for engineering applications. The nature of the MPI scheme is free from this shortcoming.

An alternative procedure in simply achieving a specific MPI two-phase system is suggested using only the properties of pressure, liquid density, vapour density, and sound speeds in vapour and liquid phase. The simulated system only knows the MPI EOS (not liquid and vapour densities). The liquid-vapour densities found from the simulated system show good agreement with the desired values.

Chapter 4 – Multipseudopotential interaction for cubic EOSs

4.1 Introduction

A method is developed to analytically and consistently implement cubic equations of state into the multipseudopotential interaction scheme in the class of two-phase Lattice Boltzmann models [179]. An MPI forcing term is applied to reduce the constraints on the mathematical shape of the thermodynamically consistent pseudopotentials; this allows the parameters of the MPI forces to be determined analytically without the need of curve-fitting or trial and error methods. Attraction and repulsion parts of EOSs, representing underlying molecular interactions, are modelled by individual pseudopotentials. Four EOSs, van der Waals, Carnahan-Starling, Peng-Robinson, and Soave-Redlich-Kwong, are investigated and the results show that the developed MPI-LB system can satisfactorily recover the thermodynamic states of interest. The phase interface is predicted analytically and controlled via EOS parameters independently and its effect on the vapour-liquid equilibrium system is studied. The scheme is highly stable to very high-density ratios and the accuracy of the results can be enhanced by increasing the interface resolution. The MPI drop is evaluated with regard to surface tension, spurious velocities, isotropy, dynamic behaviour, and the stability dependent on the relaxation time.

4.2 Analysis of MPI

It has been shown that the MPI scheme is intrinsically consistent with thermodynamics to the second order of spatial derivatives [179]. The pressure tensor of the MPI system can be exactly expressed by the MPI force on a discrete lattice for the nearest and next-nearest interactions. In the case of D2Q9 lattice and continuum limit where all gradients are in the x direction, the contribution of the all potentials of the MPI force to the normal component of the pressure tensor can be found on the $x-y$ plane (to the second order) [179] equation (3-5). The system results in bulk pressure of

$$p = \rho\theta + \sum_{j=1}^{n} \frac{G_j c^2}{2} \left(\frac{\rho}{\lambda_j \varepsilon + C_j \rho}\right)^{2/\varepsilon} . \tag{4-1}$$

In this equation of consistent pressure, G_j, λ_j, C_j are free parameters, however, ε is constrained by the order of isotropy of the interaction force on the lattice, see Eqs. (2-68) and (2-82). Therefore, as discussed in the previous study [179] the functions in the

formats, such as ρ^h and $(\rho/(1+C\rho))^h$, where h is an arbitrary number, are not accepted in the MPI EOS while they are the necessary parts of well-known cubic equations of state including the VW, CS, SRK, PR. To eliminate this constraint, in the following section, the forcing scheme is modified to make ε flexible.

4.3 A more flexible MPI scheme

To incorporate the lattice force, shifting the particles momentums in the equilibrium distribution functions was proposed by Shan and Chen [111]. However Guo et al. [158] demonstrated that the following forcing term is necessary to consider the discrete effects of the lattice,

$$F_i = 3w_i\Delta t\left[\frac{\mathcal{B}_\alpha e_{i\alpha}}{c^2}+\frac{\mathcal{C}_{\alpha\beta}(3e_{i\alpha}e_{i\beta}-\delta_{\alpha\beta}c^2)}{2c^4}\right], \tag{4-2}$$

where the Einstein summation convention is adopted. This equation gives rise to the stress tensor in the continuum limit, as follows,

$$\sigma_{\alpha\beta}=\frac{c^2}{3}(\tau-\frac{1}{2})\Delta t\rho(\delta_\alpha v_\beta+\delta_\beta v_\alpha)+\Delta t\left[(\tau-\frac{1}{2})(v_\alpha F_\beta+v_\beta F_\alpha)-\frac{\tau}{2}(\mathcal{C}_{\alpha\beta}+\mathcal{C}_{\beta\alpha})\right], \tag{4-3}$$

where v is the actual fluid velocity, applied in the equilibrium distribution function, and defined as

$$v_\alpha = u_\alpha + F_\alpha\Delta t/2\rho, \tag{4-4}$$

where $u_\alpha=\sum_i f_i e_{i\alpha}/\rho$. If $\mathcal{B}_\alpha=(1-\frac{1}{2\tau})F_\alpha$, and $\mathcal{C}_{\alpha\beta}$ is set at $\mathcal{C}^{NS}_{\alpha\beta}=(1-\frac{1}{2\tau})(2v_\beta F_\alpha)$, Navier-stokes stress tensor is recovered [158] as,

$$\sigma^{NS}_{\alpha\beta}=\frac{c^2}{3}(\tau-\frac{1}{2})\Delta t\rho(\delta_\alpha v_\beta+\delta_\beta v_\alpha)\ . \tag{4-5}$$

Li et al. [151] showed that considering the additional term $F_\alpha F_\beta/\psi^2$ to the stress tensor can effectively modify ε which appears in the thermodynamic consistency condition (2-81). The leading term of $F_\alpha F_\beta/\psi^2$ is [151]

$$\frac{F_\alpha F_\beta}{\psi^2} = -G^2 c^4 \partial_\alpha \psi \partial_\beta \psi + O(\partial^4) \ . \tag{4-6}$$

Here, for the MPI, we use a similar term and set tensor $\mathcal{C}_{\alpha\beta}$ as

$$\mathcal{C}_{\alpha\beta}^{MPI} = (1-\frac{1}{2\tau})(2v_\beta F_\alpha^{total}) + \sum_j^n \frac{s_j F_\alpha^{(j)} F_\beta^{(j)}}{\tau \psi_j^2}, \tag{4-7}$$

where s_j are arbitrary constants. Substituting (4-7) into (4-2), we obtain

$$\begin{aligned} F_i = 3w_i \Delta t (1-\frac{1}{2\tau}) \left[\frac{e_{i\alpha} - v_\alpha}{c^2} + \frac{3v_\beta e_{i\beta} e_{i\alpha}}{c^4} \right] F_\alpha^{total} \\ + \frac{3w_i \Delta t}{2c^4} \sum_j^n \left[\frac{s_j}{\tau \psi_j^2} (3F_\alpha^{(j)} F_\beta^{(j)} e_{i\alpha} e_{i\beta} - c^2 F_\alpha^{(j)} F_\alpha^{(j)}) \right]. \end{aligned} \tag{4-8}$$

As a result, the macroscopic approximation of the MPI-LB equation leads to

$$\partial_t(\rho v_\beta) + \partial_\alpha(\rho v_\alpha v_\beta) = -\partial_\beta p + \partial_\alpha \sigma_{\alpha\beta}^{NS} + F_\beta - \Delta t \partial_\alpha \sum_j^n \frac{s_j F_\alpha^{(j)} F_\beta^{(j)}}{\psi_j^2}, \tag{4-9}$$

where p is the ideal gas pressure. The excess terms on the right-hand side of (4-9) can be considered a part of the pressure tensor

$$P_{\alpha\beta} = P_{\alpha\beta}^{original} + \Delta t c^4 \sum_{j=1}^n s_j G_j^2 \partial_\alpha \psi \partial_\beta \psi \, . \tag{4-10}$$

where equation (4-6) is used. For the case of a one-dimensional planar interface, the component of the pressure tensor which is normal to the interface now takes the form (compare with Eq. (3-5))

$$P_{xx} = \sum_{j=1}^n \frac{G_j c^2}{2} \psi_j^2 + \frac{G_j c^4}{12} \left[(a_1 + 12\Delta t s_j G_j) \left(\frac{d\psi_j}{dx} \right)^2 + a_2 \psi_j \frac{d^2 \psi_j}{dx^2} \right]. \tag{4-11}$$

Therefore, ε in equation (4-1) now becomes

$$\psi_j(\rho) = \left(\frac{\rho}{\lambda_j \varepsilon_j + C_j \rho} \right)^{1/\varepsilon_j}, \tag{4-12}$$

$$\varepsilon_j = -2(a_1 + 12\Delta t s_j G_j)/a_2, \tag{4-13}$$

which is the relation derived to release the constraint of the MPI as by which $\{\varepsilon_j : j = 1,2,...,n\}$ become flexible and independent of each other in the pseudopotentials of the MPI. The MPI EOS is, therefore, defined as

$$p = \rho\theta + \sum_{j=1}^{n} \frac{G_j c^2}{2} \left(\frac{\rho}{\lambda_j \varepsilon_j + C_j \rho}\right)^{2/\varepsilon_j}. \tag{4-14}$$

As expected, in comparison with (4-1), the additional term in (4-7) modifies the thermodynamic condition only through ε_j and the rest stays intact. In other words, ε_j is a function of the free parameter s_j. To obtain the interface shape, the equation (3-8) becomes

$$(c\partial_x \rho)^2 \frac{a_2}{12\rho^4} \sum_{j=1}^{n} \lambda_j \psi_j^{\varepsilon_j} \frac{G_j c^2 \psi_j^2}{2} = \int_{\rho_v}^{\rho} \left(p_0 - \rho\theta - \sum_{j=1}^{n} \frac{G_j c^2}{2} \psi_j^2 \right) \frac{d\rho}{\rho^2}. \tag{4-15}$$

The surface tension of the two-phase MPI system can be presented by the mechanical route definition; in the case of a planar interface, it is calculated from $\sigma = \int_{-\infty}^{+\infty} (p_N - p_T) dx$, where p_N is the local pressure normal to the interface and p_T the local pressure tangential to the interface,

$$\sigma = \frac{c^4}{12} \sum_{j=1}^{n} \int_{\rho_v}^{\rho_l} G_j K_j (\psi_j')^2 (\partial_x \rho) d\rho \tag{4-16}$$

where $K_j = -6e_4 + 12\Delta t G_j s_j$ and $\partial_x \rho$ is solved by (4-15). Considering Eq. (4-13), we have

$$K_j = -\varepsilon_j (3e_4 + \frac{1}{2}) - 3e_4 - 1. \tag{4-17}$$

4.4 Mapping cubic equations of state onto the MPI scheme

Here we show how the cubic equations of state such as the VW, CS, SRK, and PR can be implemented analytically and consistently into the MPI-LB system.

For the VW, the EOS,

$$p = \frac{\rho T}{1-b\rho} - a\rho^2, \tag{4-18}$$

exists as the basis of many other EOSs of real fluids. The fluid's critical point (critical density $\rho_c = 1/3b$, critical temperature $T_c = 8a/27b$, and critical pressure $p_c = a/27b^2$) is deemed to be the reference point for normalisation. It should be noted that, based on critical points, reduced (nondimensional) pressure, $p_R = p/p_c$, reduced density $\rho_R = \rho/\rho_c$, and reduced temperature $T_R = T/T_c$ are defined.

According to (4-14), the functions such as ρ^h or $(\rho/(1+C\rho))^h$ are thermodynamically consistent as pseudopotentials, and the parameters of pseudopotentials of the MPI can be adjusted, in a sense, the MPI EOS matches the VW EOS. We describe the procedures step by step as follows by means of three pseudopotentials $(n=3)$. Considering (4-14), firstly we remove the lattice ideal pressure $(\rho\theta)$ from the MPI EOS; therefore, the first pseudopotential $(j=1)$ is assigned to it

$$\frac{G_1 c^2}{2}\psi_1^2 = \frac{G_1 c^2}{2}\left(\frac{\rho}{\lambda_1\varepsilon_1 + C_1\rho}\right)^{2/\varepsilon_1} = -\rho\theta \ . \tag{4-19}$$

From this equality, we find $G_1 = -2/3$, $C_1 = 0$, $\varepsilon_1 = 2$, and $\lambda_1 = 1/2$. The second pseudopotential $(j=2)$ represents the repulsion term of the VW EOS,

$$\frac{G_2 c^2}{2}\psi_2^2 = \frac{G_2 c^2}{2}\left(\frac{\rho}{\lambda_2\varepsilon_2 + C_2\rho}\right)^{2/\varepsilon_2} = \frac{\rho T}{1-b\rho}, \tag{4-20}$$

from which, we obtain $G_2 = 2T/c^2$, $C_2 = -b$, $\varepsilon_2 = 2$, and $\lambda_2 = 1/2$. The third pseudopotential $(j=3)$ demonstrates the attraction term of the VW EOS,

$$\frac{G_3 c^2}{2}\psi_3^2 = \frac{G_3 c^2}{2}\left(\frac{\rho}{\lambda_3\varepsilon_3 + C_3\rho}\right)^{2/\varepsilon_3} = -a\rho^2, \tag{4-21}$$

then we find $G_3 = -2a/c^2$, $C_3 = 0$, $\varepsilon_3 = 1$, and $\lambda_3 = 1$. It should be noted that s_j can be found from (4-13) and applied in Eq.(4-8). Consequently, it can be seen that each pseudopotential is assigned to the physics, one describes the dynamics of an individual molecule, the second creates solely short-range repulsion interactions, and the third

mimics the long-range attraction of particles. All parameters are listed in Table 4-1 for reference. Because the procedure of determining the MPI forces parameters for the VW EOS, conditions (4-19)-(4-21), is the same as those to be used for the other EOSs, no details will be given in the following discussions.

The CS EOS,

$$p = \rho T \frac{1+\eta+\eta^2-\eta^3}{(1-\eta)^3} - a\rho^2 \ , \tag{4-22}$$

which modifies the hard sphere repulsion part of the VW equation, is an EOS widely used in the pseudopotential LB community. Here $\eta = b\rho/4$, $a = \Omega_a T_c^2 / P_c$, $b = \Omega_b T_c / P_c$, $b\rho_c/4 = \Omega_c$, $\Omega_a = 0.496388$, $\Omega_b = 0.187295$, $\Omega_c = 0.130444$. The reduced form of the CS EOS is

$$p_R = (4\Omega_c/\Omega_b)\rho_R T_R \frac{1+(\Omega_c\rho_R)+(\Omega_c\rho_R)^2-(\Omega_c\rho_R)^3}{(1-\Omega_c\rho_R)^3} - \Omega_a(4\Omega_c/\Omega_b)^2\rho_R^2 . \tag{4-23}$$

The CS EOS can be rewritten as

$$p = \rho T + bT\frac{\rho^2}{(1-(b/4)\rho)^2} + \frac{b^2T}{8}\frac{\rho^3}{(1-(b/4)\rho)^3} - a\rho^2 . \tag{4-24}$$

Therefore, the CS EOS is in accordance with the MPI EOS. The relevant parameters of the MPI EOS are listed in Table 4-1. It should be noted that the first pseudopotential has two parts: the first part is utilised to remove the lattice ideal pressure ($\rho\theta$) while second part exerts the CS fluid ideal pressure (ρT).

The SRK EOS is the well-known two-parameter cubic equation of state and the first modern EOS which is widely applied to design of hydrocarbon-treatment plants [180]. The SRK is the significant modification of RK EOS proposed by Soave [181]

$$p = \frac{\rho T}{1-b\rho} - \frac{\alpha a\rho^2}{1+b\rho}, \tag{4-25}$$

where $a = \Omega_a T_c^2 / P_c$, $b = \Omega_b T_c / P_c$, $\rho_c T_c / P_c = 3$, $\sqrt{\alpha} = 1+m(1-\sqrt{T_R})$, $\Omega_a = 0.427480$, $\Omega_b = 0.086640$, $m = (0.480+1.574\omega-0.176\omega^2)$, and ω is Pitzer's acentric factor. α

is determined from experimental vapour pressures of non-polar substances. The properties of the critical point can be found from the fact that the first and second derivatives of pressure with respect to density at the critical point are zero. In contrast to RK EOS, the reduced format of the SRK depends on the acentric factor ω, which helps to treat non-polar substances $(p_R = 3\rho_R T_R/(1-3\Omega_b\rho_R) - 9\Omega_a\alpha\rho_R^2/(1+3\Omega_b\rho_R))$. By decomposing the second term of the SRK EOS, we obtain

$$p = \frac{\rho T}{1-b\rho} - \frac{\alpha a}{b}\rho + \frac{\alpha a}{b}\frac{\rho}{(1+b\rho)}. \tag{4-26}$$

Now, the SRK EOS is well consistent with the MPI EOS. The relevant parameters of pseudopotentials of the MPI scheme are listed in Table 4-1.

The PR EOS [182] is devised to overcome the weakness of the SRK in predicting liquid phase density [183]

$$p = \frac{\rho T}{1-b\rho} - \frac{\alpha a\rho^2}{1+2b\rho-b^2\rho^2}, \tag{4-27}$$

where $a = \Omega_a T_c^2/P_c$, b=$\Omega_b T_c/P_c$, $b\rho_c = \Omega_c$, Ω_a=0.457236, $\Omega_b = 0.077796$, $\Omega_c = 0.253077$ and α is similar to that in the SRK equation but m is correlated with the aid of vapour pressure data from normal boiling point to the critical point

$$m = 0.37464 + 1.54226\omega - 0.26992\omega^2. \tag{4-28}$$

The reduced form of the PR EOS is

$$p_R = (\frac{\Omega_c}{\Omega_b})\frac{\rho_R T_R}{1-\Omega_c\rho_R} - \frac{\alpha\rho_R^2}{1+2\Omega_c\rho_R-\Omega_c^2\rho_R^2}\Omega_a(\frac{\Omega_c}{\Omega_b})^2. \tag{4-29}$$

The PR EOS can be rearranged into the following shape

$$p = \frac{\rho T}{1-b\rho} + \left(\frac{\alpha a}{2b\sqrt{2}}\right)\frac{\rho}{1+b\left(1+\sqrt{2}\right)\rho} - \left(\frac{\alpha a}{2b\sqrt{2}}\right)\frac{\rho}{1+b\left(1-\sqrt{2}\right)\rho}. \tag{4-30}$$

Therefore, each term of the PR EOS now agrees with the MPI EOS. The corresponding pseudopotential parameters are listed in Table 4-1.

Table 4-1. The MPI forces parameters which reproduce the selected EOSs in the LB system

EOS	j-th pseudopotential	G_j	ε_j	λ_j	C_j
VW	1	$-\frac{2}{3}$	2	$\frac{1}{2}$	0
	2	$T\frac{2}{c^2}$	2	$\frac{1}{2}$	$-b$
	3	$-a\frac{2}{c^2}$	1	1	0
CS	1	$-\frac{2}{3}+\frac{2T}{c^2}$	2	$\frac{1}{2}$	0
	2	$bT\frac{2}{c^2}$	1	1	$-\frac{b}{4}$
	3	$\frac{b^2T}{8}\frac{2}{c^2}$	$\frac{2}{3}$	$\frac{3}{2}$	$-\frac{b}{4}$
	4	$-a\frac{2}{c^2}$	1	1	0
SRK	1	$-\frac{2}{3}-\frac{\alpha a}{b}\frac{2}{c^2}$	2	$\frac{1}{2}$	0
	2	$T\frac{2}{c^2}$	2	$\frac{1}{2}$	$-b$
	3	$\frac{\alpha a}{b}\frac{2}{c^2}$	2	$\frac{1}{2}$	b
PR	1	$-\frac{2}{3}$	2	$\frac{1}{2}$	0
	2	$T\frac{2}{c^2}$	2	$\frac{1}{2}$	$-b$
	3	$\left(\alpha a / 2b\sqrt{2}\right)\frac{2}{c^2}$	2	$\frac{1}{2}$	$b\left(1+\sqrt{2}\right)$
	4	$-\left(\alpha a / 2b\sqrt{2}\right)\frac{2}{c^2}$	2	$\frac{1}{2}$	$b\left(1-\sqrt{2}\right)$

It is worth mentioning that in contrast to many other studies [129, 136, 151, 162], where thermodynamic consistency is sought by trial and error methods, curve-fitting, or solving a nonlinear equation, the consistent MPI forces proposed here, exactly represent the selected EOSs. Moreover, for the sake of brevity only the abovementioned cubic EOSs are focused on, but the principle of the method is not limited to the cubic EOSs, it is applicable to the EOSs in other function formats, such as polynomial and virial functions, and the versions of EOSs developed based on them (see section 4.5).

Using the MPI scheme, the interaction force between two nodes is calculated by summation of n (number of pseudopotentials) sub-forces. For the case of the two-dimensional nearest-node interactions, a node experiences $8n$ interactions. Therefore, increasing the number of pseudopotentials, we expect more computational costs, for example, the MPI code running the SRK or VW EOSs is faster than the one implementing the PR or CS EOS (see Table 4-1), however, it is slower than a non-modified SPI code [131] running the SRK, VW, PR, or CS.

4.5 Mapping VW-like and virial EOSs

We illustrate that the virial equation and the general form of the VW-like EOSs can be incorporated into the MPI-LB. The virial EOS is defined based on the theories of statistical mechanics as an unlimited series of molar density [183]

$$p = \rho T + B_2\rho^2 + B_3\rho^3 + \cdots , \tag{4-31}$$

where B_2, B_3, etc., are functions of temperature only, and are the second, third, and so on virial coefficients. The virial EOS is well in conformity with the MPI EOS with the corresponding parameters listed in Table 4-2.

Almost all VW type EOSs, such as Schmidt-Wenzel EOS [184], Patel-Teja EOS[185], can be expressed in the general form of [183]

$$p = \frac{\rho T}{1-b\rho} - \frac{a\rho^2}{1+2u\rho-w^2\rho^2} , \tag{4-32}$$

where a, u, and w don't depend on density but, possibly, other parameters such as critical point specifications and the acentric factor. After some lengthy but simple algebra, we can rewrite the EOS as

$$p=\frac{\rho T}{1-b\rho}-\frac{a}{2\sqrt{u^2+w^2}}\frac{\rho}{\left[1+\left(u-\sqrt{u^2+w^2}\right)\rho\right]} \\ +\frac{a}{2\sqrt{u^2+w^2}}\frac{\rho}{\left[1+\left(u+\sqrt{u^2+w^2}\right)\rho\right]}. \tag{4-33}$$

Now, we can straightforwardly set the MPI forces to consistently implement the general form of VW-like EOSs as shown in Table 4-2. The first force is used to remove ideal gas pressure which is automatically made by lattice Boltzmann. The other forces are assigned to attraction and repulsion part of cubic equations of state and higher order terms of virial equation of state.

Table 4-2. The MPI forces parameters which reproduce virial and VW-like EOSs in the LB system

EOS	j-th pseudopotential	G_j	ε_j	λ_j	C_j
virial	1	$-\frac{2}{3}+\frac{2T}{c^2}$	2	$\frac{1}{2}$	0
	$j>1$	$B_j\frac{2}{c^2}$	$\frac{2}{j}$	$\frac{j}{2}$	0
VW-like	1	$-\frac{2}{3}$	2	$\frac{1}{2}$	0
	2	$T\frac{2}{c^2}$	2	$\frac{1}{2}$	$-b$
	3	$-\frac{a}{2\sqrt{u^2+w^2}}$	2	$\frac{1}{2}$	$u-\sqrt{u^2+w^2}$
	4	$\frac{a}{2\sqrt{u^2+w^2}}$	2	$\frac{1}{2}$	$u+\sqrt{u^2+w^2}$

4.6 Results and discussion

To verify the theoretical derivations and demonstrate how the proposed method works, simulations of planar interfaces are carried out. In subsection 4.6.1 the parameters and details of simulations are described. The thermodynamic consistency and interface shape are discussed in subsection 4.6.2, and the mechanism of the scheme in controlling

the interface width is studied in subsection 4.6.3. The capability of the method in reproducing Maxwell construction curves is investigated in subsection 4.6.4. The MPI droplet is thoroughly studied in 4.6.5.

4.6.1 Simulation setup

All simulations are run on a two-dimensional square lattice including nine velocities (D2Q9). The computational domain for one-dimensional planar interfaces contains 1×500 nodes and for two-dimensional cases contains 300×300 in most of the simulations, while, for the simulations of very wide interfaces a larger number of lattice nodes are utilised, for which the details will be given individually. The nondimensional relaxation time is set to unity $\tau=1$ unless otherwise stated. It should be noted that increase of τ increases viscosity and based on (2-42) $\tau>0.5$. The nearest-node interactions are considered which set $w(1)=1/3$, $w(2)=1/12$, $a_1=0$, $a_2=3$ [141]. The MPI forces are calculated by use of Eqs. (3-2), and (4-12) whose parameters, for the selected EOSs, can be found in Table 4-1. The internal forces are embedded in the LBE using Eq. (4-8), which reproduces Navier-Stokes equations to the second order. For the case of the planar interface, half of the domain is filled with liquid and the other half with the vapour. The periodic condition is applied at all boundaries. ρ_l and ρ_v (the densities of liquid and vapour) are initially set, in a sense, to ensure that the system is in the saturation state. To avoid an initial instability, a diffuse interface should be adopted at the beginning of simulations. We utilise the suggestion of Ref. [136] for initializing interfaces

$$\rho(r)=\frac{\rho_l+\rho_v}{2}-\frac{\rho_l-\rho_v}{2}\tanh\left(\frac{r-R}{W}\right), \tag{4-34}$$

where W controls the interface width and, in all simulations, is set at $W=5$ which gives a stable initial state, R is the distance between the interface and the reference point, and r, is the variable distance from the reference point. For the case of the planar interface, it can be one of the boundaries parallel to the phase interface. Unless otherwise stated, lattice spacing parameter is set to unity $c=1$ and EOS parameters for all types are set at $a=0.01$ and $b=0.2$ (the effect of the change of a,b,c will be studied in section 4.6.3). The simulations are run for at least 10^5 steps and pressure

tensor profile in VLE systems are monitored to verify that the equilibrium state is reached.

4.6.2 Thermodynamic consistency

To investigate the thermodynamic consistency, the first set of simulations is performed to measure the total normal component of the pressure tensor, $p_0 = P_{xx} + \rho\theta$. Based on the mechanical stability of the flat interfaces, p_0 must be constant across the phase interface (for more details refer to [124]).

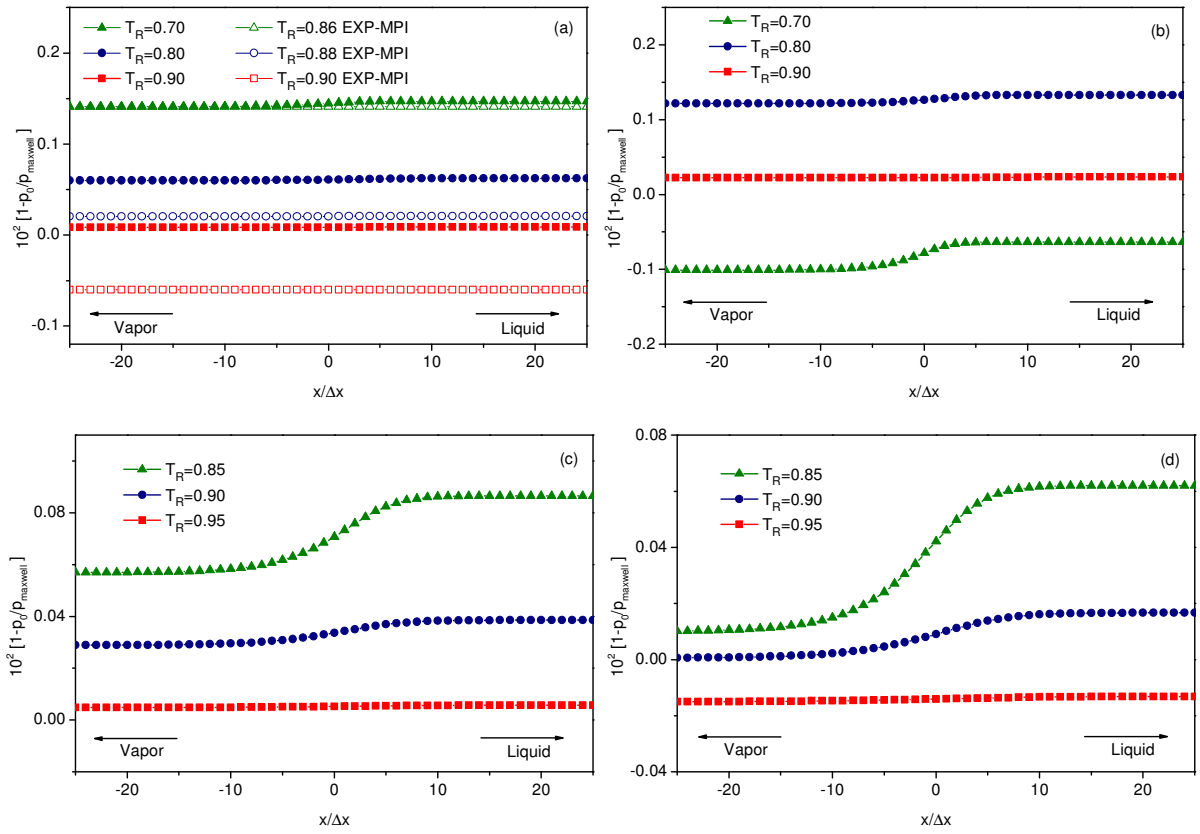

Figure 4-1. Error due to the change of the normal component of pressure tensor along flat interfaces at different temperatures for the selected EOSs: (a) VW, (b) CS, (c) SRK, and (d) PR. Pressure is normalised with the aid of the saturation pressure predicted by the Maxwell equal-area rule. In graph (a) EXP-MPI symbols represent the MPI made of exponential functions from Chapter 3.. The errors are smoothly changing from one phase to the other one.

P_{xx} is calculated from Eq. (4-11) where both first and second spatial derivatives of pseudopotentials are computed by use of the second order central difference approximations. The results are shown in Figure 4-1. For the selected EOSs and specified temperatures, the errors are small and less than 0.15% which validates the

mechanical stability of the proposed scheme. The errors increase with the decrease of temperature which will be discussed in 4.6.4.

The gradient of density along the phase interface can be calculated analytically from Eq. (4-15) as the right-side integral has an analytical solution. Then, by numerically solving $x=\int_{(\rho_v+\rho_l)/2}^{\rho}(\partial_x\rho)^{-1}d\rho$, the spatial profile of density can be achieved. Figure 4-2 depicts the phase interfaces for the selected EOSs and the comparisons of the simulation results with the theoretical predictions. The main graphs of Figure 4-2 are focusing on liquid phase densities and inset graphs put emphasis on vapour phase densities; the simulations are in good agreement with the theory which means the interface shape can be ably predicted.

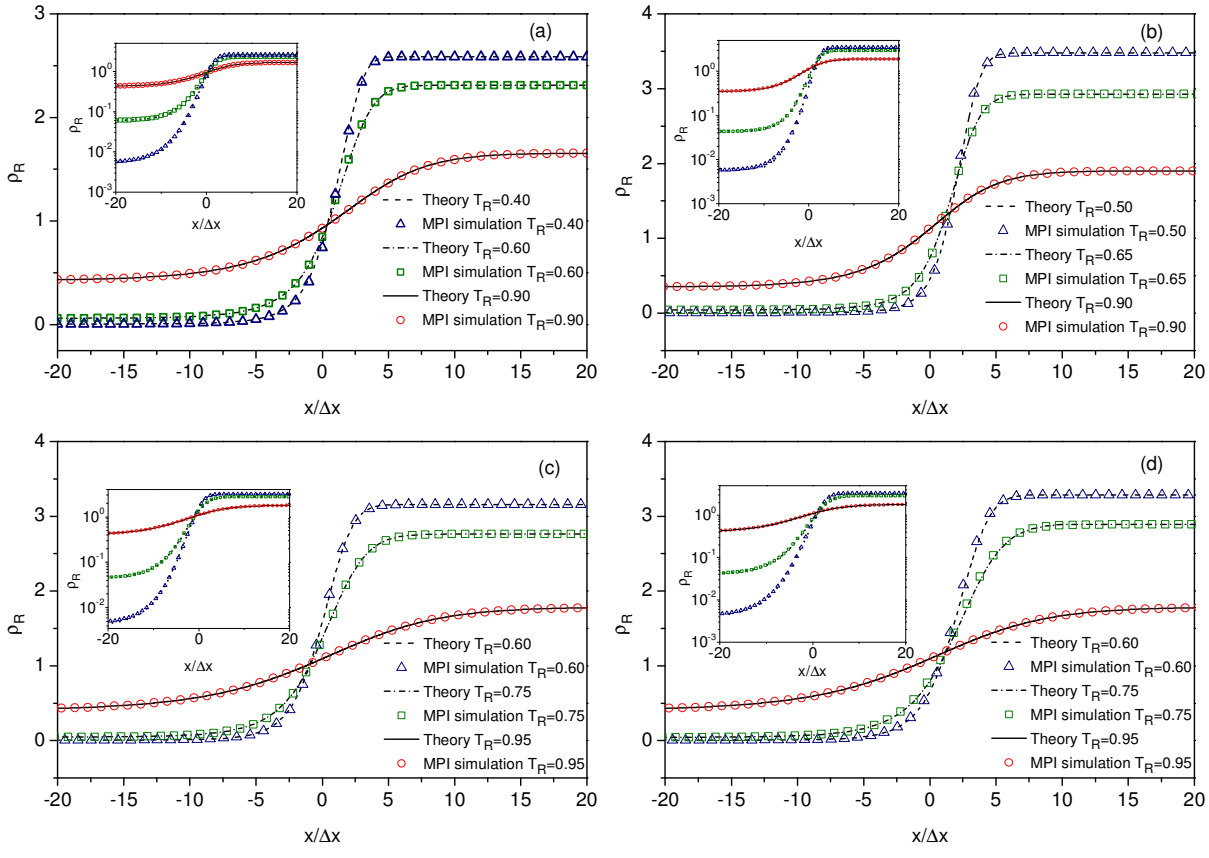

Figure 4-2. The Phase interfaces found from MPI simulations and the theoretical predictions, Eq. (4-15), at different temperatures for the selected EOSs: (a) VW, (b) CS, (c) SRK, and (d) PR.

When a high-density ratio system is desired an initial guess of equation (4-34) may not be of help and the simulation crashes because of instabilities generated at the interface.

Therefore, knowing the equilibrium interface shape in advance can effectively enhance the starting point stability of the system in practical cases.

4.6.3 Scalability and interface width control

Herein, for the sake of brevity, we merely focus on the SRK EOS and investigate EOS parameters thoroughly. If we divide both sides of Eq. (4-15) by p_c / ρ_c and use the MPI SRK pseudopotentials of Table 4-1, the equation could be normalised. Therefore, after some lengthy but simple algebra, we obtain

$$(c\partial_x \rho_R)^2 \frac{a_2}{24\rho_R^2}\left[-\frac{bc^2}{a}\frac{\Omega_a}{\Omega_b}-\frac{3\alpha\Omega_a}{\Omega_b}+\frac{3T_R}{(1-3\Omega_b\rho_R)^2}+\frac{3\alpha\Omega_a}{\Omega_b(1+3\Omega_b\rho_R)^2}\right] = \int_{\rho_{v(R)}}^{\rho_R}\left(p_{0(R)}-p_R^{SRK}\right)\frac{d\rho_R}{\rho_R^2}. \tag{4-35}$$

It can be seen that the right-hand side of (4-35), which is the Maxwell construction integral, is in the reduced format which means it is independent of EOS parameters a and b, and lattice scaling parameter c. Therefore, the reduced VLE densities are not affected by the change of those parameters. It is understood that the terms, which are multiplied by the gradient of density, are impacting the interface shape. In the left-hand side of (4-35), all terms are in the reduced format as well, except the first term in the brackets which is a function of ratio parameter $\chi = bc^2 / a$. Therefore, it is expected that this parameter, χ, is the sole parameter responsible for the change in the width of the phase interface. As the VLE system is independent of χ in Eq. (4-35), the sound speed in liquid and vapour is independent of χ as well and is consistent with the EOS.

Four simulations are run for the different attraction parameter values $a = 0.001, 0.01, 0.09, 0.25$ while the SRK EOS is set at $T_R = 0.80$, $b = 0.2$, and $c = 1$. The results are shown in Figure 4-3. It is found that the increase of parameter a (decrease of χ) can effectively reduce the interface width. Another set of simulations have been run by keeping $a = 0.01$, $c = 1$ and changing b to have the same χ values as the previous simulations; the results are exactly the same as those of Figure 4-3 where the interface width increases as parameter b rises.

It is worth to mention that changing χ from 200 to 2.2 the interface is perfectly predicted by (4-15), however, for the case of $\chi = 0.8$ a very thin interface is partly predicted from vapour phase to liquid phase (see Figure 4-3). This can be understood by checking the right-hand side of Eq. (4-15), which is the Maxwell construction integral and is always negative for $\rho_v < \rho < \rho_l$. To have a meaningful gradient of density, the left-hand side of Eq. (4-15) should be negative throughout the given density interval. Therefore, in the case of $\chi = 0.8$, we cannot predict interface shape near the liquid phase as the left-hand side of Eq. (4-15) becomes positive there. Moreover, slight oscillations of density near the liquid phase of the simulated system are observed. We only experienced the partial prediction of the interface in very sharp and thin interfaces.

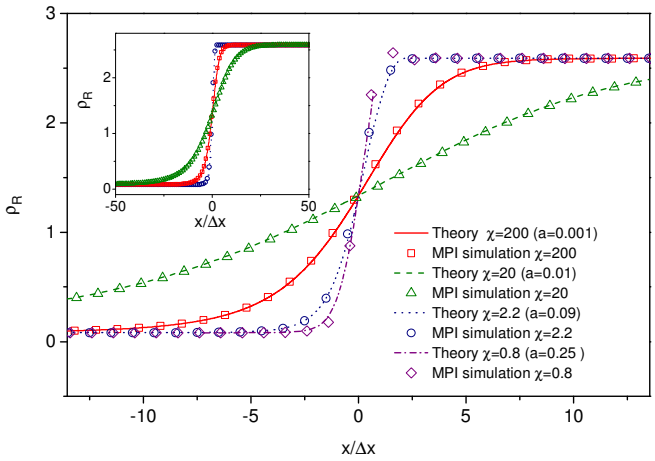

Figure 4-3. The phase interface is widened by decreasing $\chi = bc^2 / a$ for a particular VLE, the SRK EOS at $T_R = 0.80$. Parameters are set at $b = 0.2$, $c = 1$, and $a = 0.001, 0.01, 0.09, 0.25$. The theoretical profiles are obtained from Eq. (4-15). The theoretical profile of density at $\chi = 0.8$ is incomplete that is explained in section 4.6.3.

In χ another parameter, c, being the numerical resolution to capture the physical details, contributes to the interface width. For the pseudopotential LB models, it is predicted that the interface width is varied directly as the lattice scaled by means of c. This behaviour might not be of interest as the interface width of the fluids such as liquid water with its vapour is in the scope of molecular scale and LB simulations aim micro-scale phenomena, therefore scaling an LB simulation domain in the interval of micro-scale, a change in the interface shape should not be seen. The results shown in Figure

4-4 are those from the simulations with the domain being scaled at $c = 0.1,1,10$ but parameters a and b are utilised to keep $\chi = 20$. It is demonstrated that the same interface shape is obtained. The simulation results are supported by the prediction of theory (4-35).

It should be noted the VW, CS, and PR EOSs have the same behaviour as the SRK EOS and a normalised governing equation like (4-35) for the phase interface. Therefore, from the simulations and theoretical analysis, the parameter χ is identified as the only parameter that governs the interface width for the selected cubic EOSs.

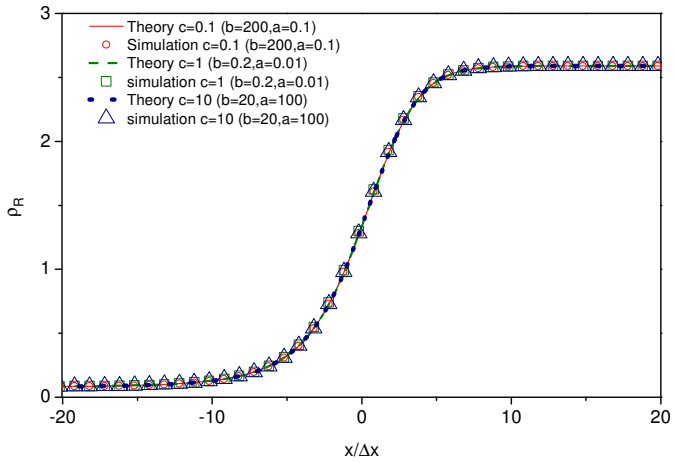

Figure 4-4. The phase interface preserves its shape through lattice scaling by keeping $\chi = 20$. The theoretical profiles are obtained from Eq. (4-15).

In addition to the discussion on the effects of EOS parameters a and b, and lattice spacing parameter c on the numerical simulations of the phase interface, it is also important to investigate the effects of those parameters on the VLE state of interest. Such a discussion, in our previous study [179], through examining the single pseudopotential scheme recovering cubic EOSs showed that the mechanical stability condition is remarkably sensitive to the changes in these parameters. Figure 4-5 shows the errors for vapour density deviation of simulations, using the MPI scheme proposed in this study, from Maxwell construction due to the change of a, b, and c. It can be seen from Figure 4-5 that error in simulating vapour density is increasing with the increase of lattice scaling parameter, c, increase of a, and decrease of b. However, all the simulations errors are less than 0.6% for the SRK EOS at $T_R = 0.80$ which means at

relatively low-density ratios (high temperatures) the thermodynamic state is satisfactorily independent of the change of those parameters.

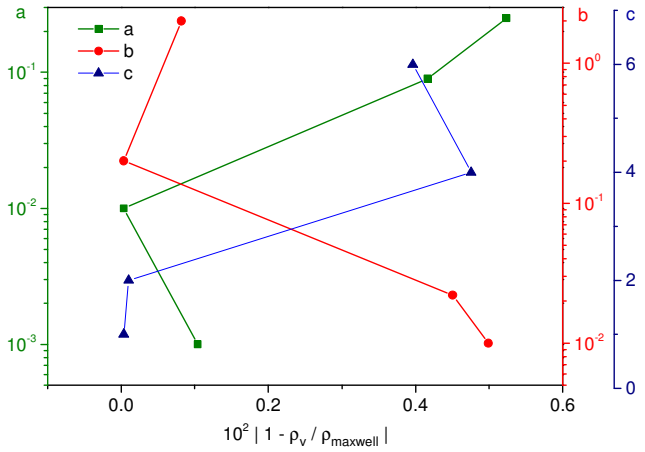

Figure 4-5. Error in vapour density due to change of EOS parameters a and b, and lattice spacing parameter c. The SRK EOS at $T_R = 0.80$ is applied.

4.6.4 Liquid-vapour saturation curves

To further test the proposed scheme, VLE systems are simulated from a temperature near the critical point to the lowest stable temperature for planar interfaces whose width are controlled via parameter χ. As the interface width theoretically goes to infinity in the case of diffuse interfaces, the non-dimensional interface width is defined as $l_{2\%} = \left| x_{\rho=0.98\rho_l} - x_{\rho=1.02\rho_v} \right| / \Delta x$. The one-dimensional domain is long enough to make sure the vapour and liquid densities reach plateau profiles. The VW, CS, SRK, and PR EOSs are examined in a sense that parameter χ is changed at each temperature to have constant interface widths of $l_{2\%} = 20, 30, 60$. The χ values are listed in Table 4-3 and Table 4-4. Figure 4-6 compares the MPI simulations of VLEs with the predictions of the Maxwell construction. It can be found that all EOSs almost perfectly simulate the liquid phase. Regarding the vapour branch, in all cases, we have satisfactory results at high temperatures and different interface widths. In the case of short interface width $l_{2\%} = 20$ the increase of error is more obvious by decreasing temperature. Widening interface width $l_{2\%} = 30, 60$, the error significantly decreases which is more apparent at lower temperatures. Therefore, at lower temperatures a higher-resolution interface is necessary for the MPI to be in accordance with the thermodynamic requirement.

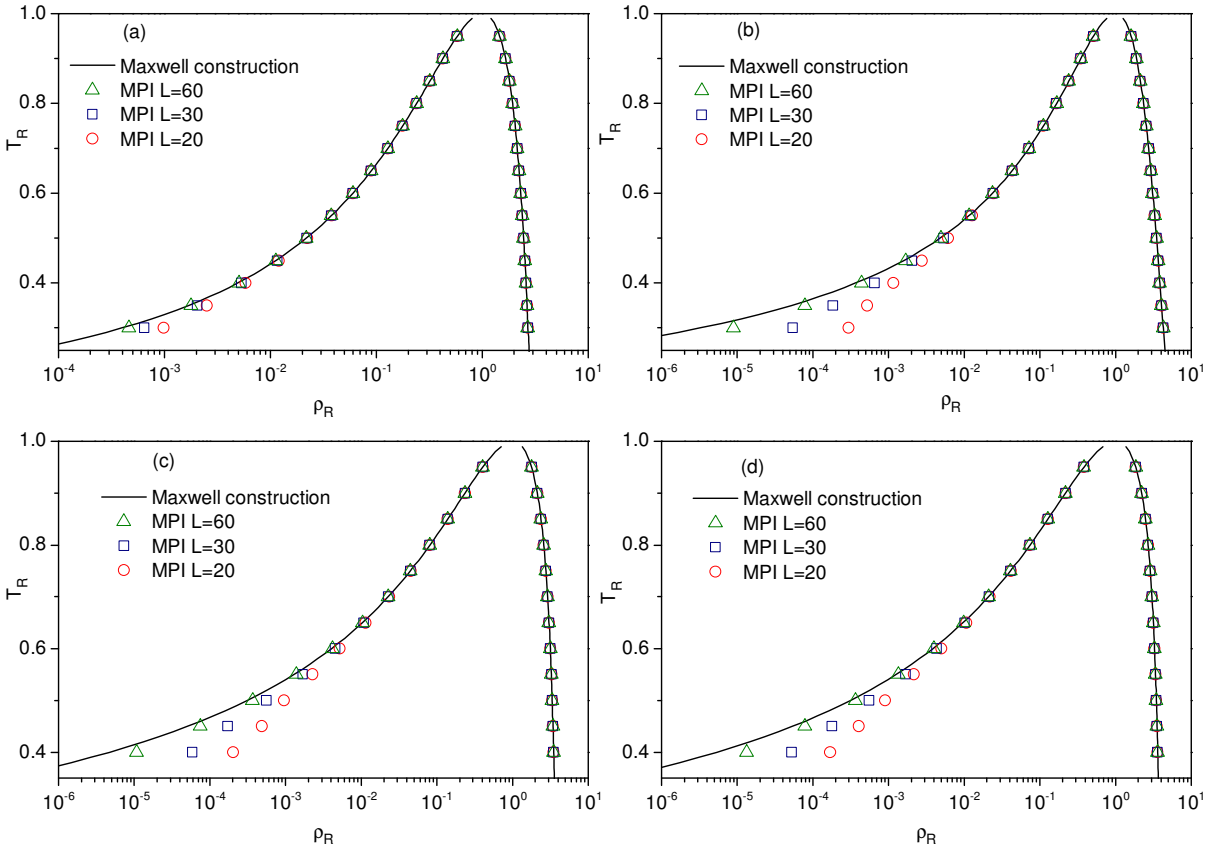

Figure 4-6. MPI results at different interface widths $l_{2\%} = 20, 30, 60$ in comparison with Maxwell construction curves for (a) VW, (b) CS, (c) SRK, and (d) PR EOSs.

The errors due to the deviation of the vapour and liquid branch from the Maxwell construction are plotted versus temperature for the selected EOSs in Figure 4-7 (a), and (b). The errors of the liquid branch for all cases are less than 0.01% and generally decrease to a local minimum and, after a rise, decrease continuously again by decrease of temperature. In general, the errors at liquid branch decrease as the interface widens at a given temperature, however, there are some exceptions such as SRK EOS at $T_R = 0.80$. Regarding the vapour branch shown in Figure 4-7 (a), in all cases the error increases but faces a fall immediately and then again increases limitlessly when temperature recedes from the critical point. Widening the interface, the vapour branch error can be effectively reduced but it might not be very helpful near the local minimum errors, such as for VW and CS at $T_R = 0.7$, and SRK and PR at $T_R = 0.8$.

When checking the liquid branch error versus density ratio in Figure 4-7 (d) the local minimum errors can be identified, which are located around density ratio of 20 for all EOSs (except PR EOS) at $l_{2\%} = 20, 30$. The local minimum errors move to density ratio

of 500 when interface width broadens to $l_{2\%} = 60$. Concerning the vapour branch, errors are shown in Figure 4-7 (d), for all cases, the local minimum errors are at density ratio around 25. Beyond the density ratio of 50, regardless of the type of the EOS, the errors are only a function of the interface width whose increase reduces the error significantly.

Considering Eqs. (4-35) and (4-15), and knowing different EOSs having different VW-loop shape, the geometrical shape (or $\partial_x \rho$) of the interfaces should vary even at the same interface width. Therefore, we expect the different EOSs at the same density ratios and interface widths show relatively different behaviour.

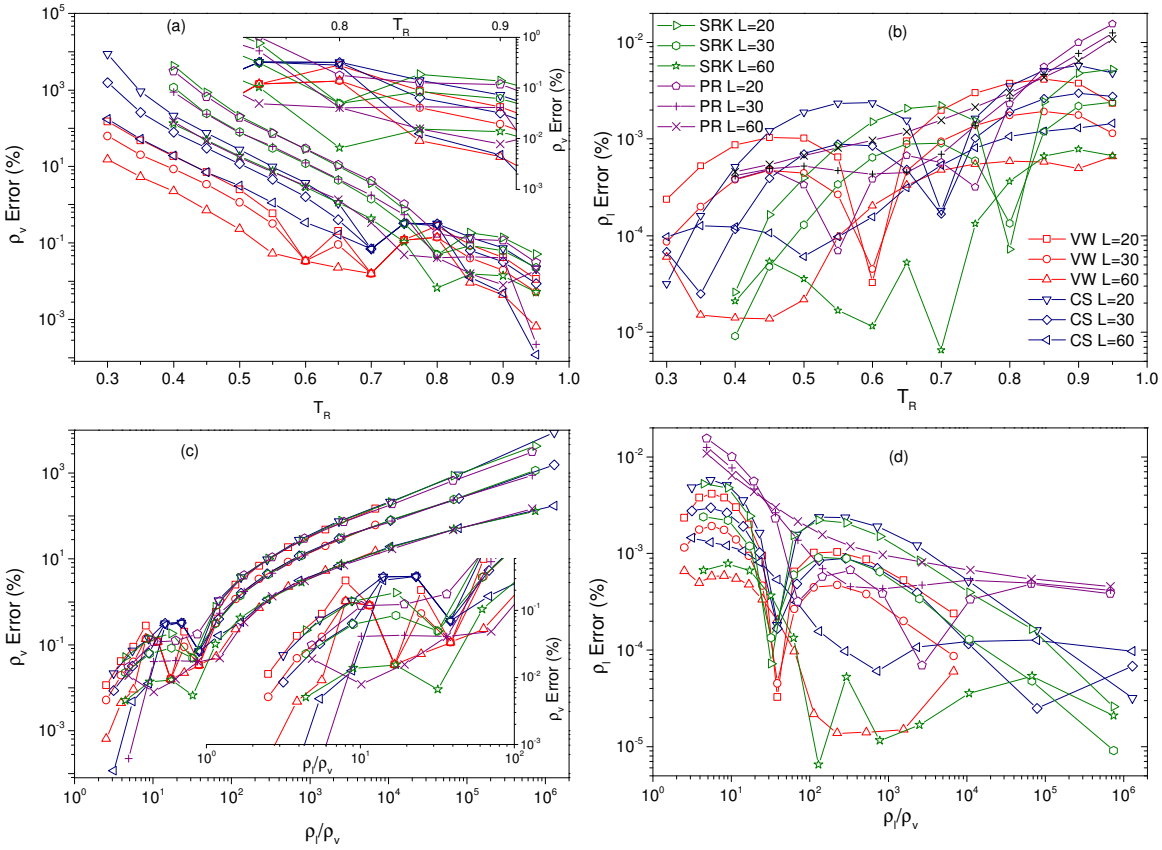

Figure 4-7. The errors due to deviation of MPI results, the saturation densities, from Maxwell construction predictions at interface widths $l_{2\%} = 20, 30, 60$ for the VW, CS, SRK, and PR EOSs: (a) the vapour branch errors vs. reduced temperature, (b) the liquid branch errors vs. reduced temperature, (c) the vapour branch errors vs. density ratio, and (d) the liquid branch errors vs. density ratio. The inset graphs are for clarifying some regions of the graphs. All graphs have the same symbol legend which is shown in graph (b).

The current MPI scheme is basically constructed on the previous idea [179]. However, from the stability viewpoint, in comparison to that, the current scheme provides an independent parameter χ, to control the interface width which helps us

straightforwardly enhance the stability of simulations. Therefore, the maximum achievable density ratio from order 10 in Chapter 3 could successfully reach to 10^6. The values of the χ parameter used in reproducing the Maxwell construction curves at different interface widths are shown in Table 4-3, and Table 4-4.

Table 4-3. The χ parameter values to obtain interface widths of $l_{2\%} = 20, 30, 60$ with VW and CS EOSs at different temperatures.

EOS	VW			CS		
T_R	χ for $l_{2\%} = 20$	χ for $l_{2\%} = 30$	χ for $l_{2\%} = 60$	χ for $l_{2\%} = 20$	χ for $l_{2\%} = 30$	χ for $l_{2\%} = 60$
0.95	5.26	11.76	46.95	7.35	16.39	65.57
0.90	8.23	18.35	73.26	11.49	25.64	102.04
0.85	10.42	23.26	92.59	14.49	32.15	128.21
0.80	12.05	26.81	106.38	16.53	36.70	145.99
0.75	13.16	29.28	116.28	17.86	39.45	156.25
0.70	13.79	30.72	121.95	18.35	40.57	161.29
0.65	14.08	31.20	123.46	18.18	40.08	158.73
0.60	13.89	30.82	121.95	17.09	38.46	150.38
0.55	13.33	29.54	116.96	16.39	36.04	142.86
0.50	12.58	27.10	106.95	14.71	32.36	120.48
0.45	11.83	24.63	96.15	12.99	28.57	111.11
0.40	10.20	21.62	84.03	12.20	25.97	92.59
0.35	9.09	20.10	74.63	10.81	22.47	68.97
0.30	7.69	15.38	60.98	9.30	18.18	66.67
0.25	-	-	-	7.87	14.71	52.63

Table 4-4. The χ parameter values to obtain interface widths of $l_{2\%} = 20, 30, 60$ with SRK and PR EOSs at different temperatures.

EOS	SRK			PR		
T_R	χ for $l_{2\%} = 20$	χ for $l_{2\%} = 30$	χ for $l_{2\%} = 60$	χ for $l_{2\%} = 20$	χ for $l_{2\%} = 30$	χ for $l_{2\%} = 60$
0.95	4.58	10.20	40.65	3.62	8.10	32.15
0.90	7.19	16.00	63.49	5.71	12.74	50.51
0.85	8.97	20.00	79.05	7.19	16.00	63.29
0.80	10.10	22.32	88.50	8.16	18.02	71.68
0.75	10.58	23.36	92.59	8.62	19.05	75.47
0.70	10.58	23.34	89.69	8.66	19.05	75.47
0.65	10.15	21.88	83.33	8.37	18.35	68.97
0.60	9.52	20.20	83.33	7.75	16.95	66.67
0.55	8.70	19.05	74.07	7.55	14.60	62.50
0.50	8.33	16.95	64.52	7.27	14.60	57.14
0.45	7.14	15.04	57.14	6.67	12.50	45.45
0.40	6.45	12.50	50.00	5.88	11.43	38.46

4.6.5 Circular droplet

MPI drops are analysed regarding measuring surface tension, spurious velocities, isotropy, dynamic behaviour, and assessing the stability dependent on the relaxation time.

To understand the effect of χ on surface tension, the SRK EOS is considered. Therefore, by substituting the SRK MPI parts from Table 4-1 into Eq. (4-16) and normalising surface tension by $\sigma_R = \sigma / (c\, p_c)$, we obtain

$$\sigma_R = \int_{\rho_v}^{\rho_l} \frac{-5}{24\rho_R} \left(c \frac{d\rho_R}{dx}\right) \times \left(-\frac{\Omega_a}{\Omega_b}\frac{bc^2}{a} - 3\alpha\frac{\Omega_a}{\Omega_b} + \frac{3T_R}{\left(1-3\Omega_b\rho_R\right)^3} + \frac{\Omega_a}{\Omega_b}\frac{3\alpha}{\left(1+3\Omega_b\rho_R\right)^3} \right) (d\rho_R) \tag{4-36}$$

where $K_1 = K_2 = K_3 = -5$ is used. All terms depend only on SRK constant parameters except $cd\rho_R / dx$ and the first term inside the brackets which are functions of $\chi = bc^2 / a$. In fact, while widening the interface, χ helps attraction interaction forces around the interface.

We make use of the Laplace test to validate equation (4-36). For measuring the surface tension in the Laplace test, it is necessary to find the accurate radius of drops in simulations. We consider a domain where density at the centre ($r = 0$) is ρ_l and it continuously declines to reach ρ_v at $r = R$; we assume it is equivalent to a domain where a drop of the radius R_m with a homogenous density of ρ_l is immediately in contact with a vapour phase with density ρ_v. By use of the mass equality, we obtain the mean radius $R_m^2 = \dfrac{2\int_0^R \rho r dr - \rho_v R^2}{\rho_l - \rho_v}$. The simulations are run in a 300×300 domain and SRK EOS at $T_R = 0.80$ is employed. Figure 4-8 shows the results of the Laplace test for drops with different radii. The surface tensions of the drops with interface widths $\chi = 2.5, 10, 25$ are satisfactorily predicted by Eq.(4-36). As it can be seen, surface tension increases with a slow rate proportional to χ, thus we advise χ is better used for adjusting the interface width rather than tuning surface tension, which will be investigated in future.

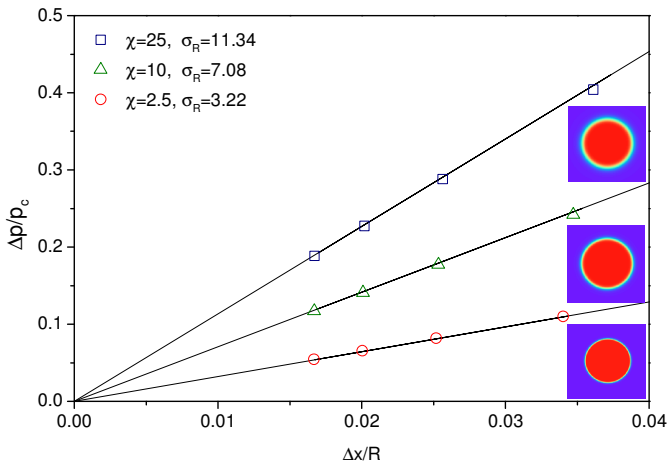

Figure 4-8. Laplace test for MPI SRK drops at $T_R = 0.80$. The interface width is widened by increasing $\chi = 2.5, 10, 25$. The solid lines show the theoretical predictions of Eq. (4-36).

As it had been discussed in the previous study [179], the MPI scheme reduces the spurious velocities as the MPI is thermodynamically consistent. In this study, the effects of interface width, which can be adjusted freely by χ, on the generation of spurious velocity are further discussed. Two 2D drops with density ratio of 1000 are set up using CS EOS at $T_R = 0.486$ and VW EOS at $T_R = 0.37$. Similar to Ref. [162], we define the distortion ratio $DR_{45} = \left|1 - r_0 / r_{45}\right|$ where r_0 is the radius of the drop along the horizontal line (0°) and r_{45} is that at 45°. The interface shapes are created by setting $\chi = 200, 20, 4$ for both the VW and CS drops which are demonstrated in Figure 4-9 where the interface becomes sharper with the decrease of χ. The maximum spurious velocities for both VW and CS EOSs drops increase about 1000 times in the order of magnitudes. The drops distortions are quite negligible as CS drops give $DR_{45} = 1.6\times10^{-4}, 1.6\times10^{-3}, 1.7\times10^{-3}$ shown in Figure 4-9 (d),(e),(f) respectively, and VW drops give $DR_{45} = 3.3\times10^{-4}, 1.1\times10^{-3}, 7\times10^{-3}$ shown in Figure 4-9 (a),(b),(c).

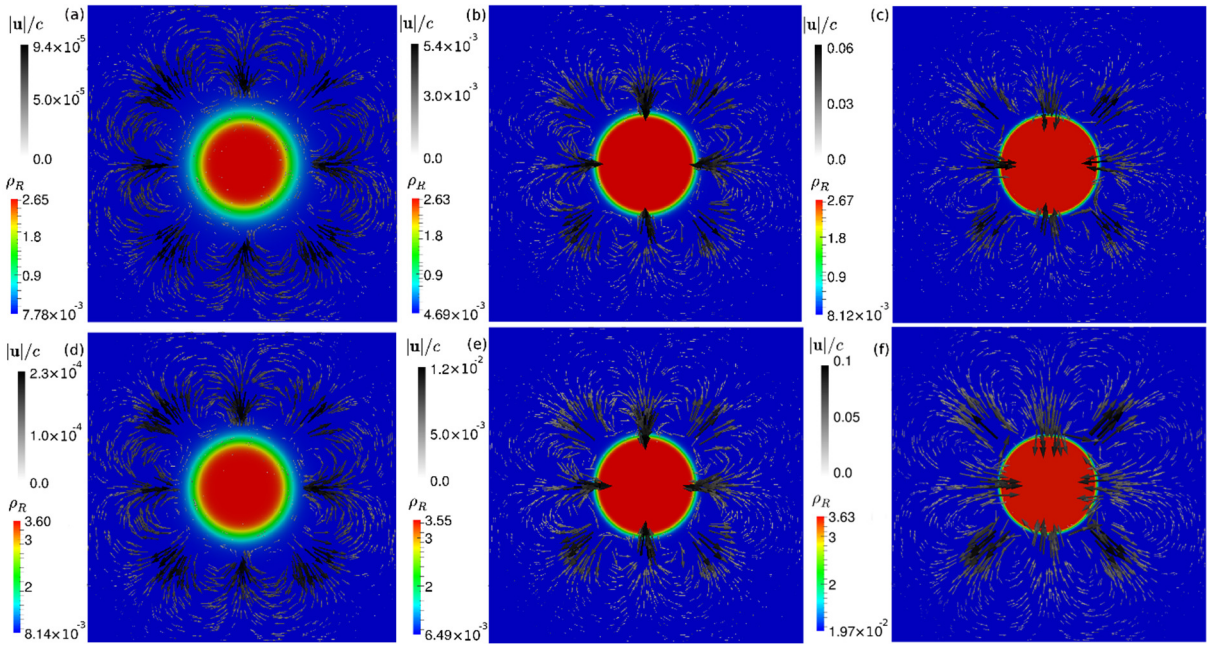

Figure 4-9. Effect of interface shortening on spurious velocities and isotropy of the VW drop at (a) $\chi = 200$, (b) $\chi = 20$, and (c) $\chi = 4$ and CS drop at (d) $\chi = 200$, (e) $\chi = 20$, (f) $\chi = 4$.

A system has Galilean invariance if Newton's law of motion is not changing in different inertial frames. With regards to fluid flows, one consequence of Galilean invariance is

that the viscose forces in a stationary frame $\mathbf{u}_{origin} = \mathbf{0}$ must be the same in a moving frame with constant velocity $\mathbf{u}_{origin} = \mathbf{u}_0$. This is valid for N-S equations as the viscose term, $\mu\nabla\cdot(\nabla\mathbf{u}+\nabla\mathbf{u}^T)$, depends on relative velocity. Simulations are run for moving circular drops to study the dynamic behaviour and assess the Galilean invariance of the proposed scheme using SRK EOS.

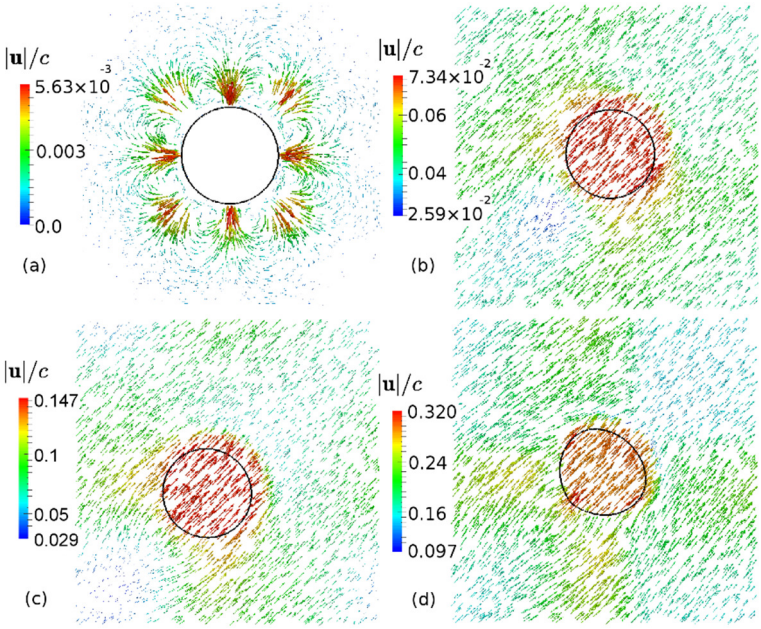

Figure 4-10. Testing Galilean invariance of an MPI SRK drop at different diagonal bulk velocities (a) $|\mathbf{u}_b| = 0$, *(b)* $|\mathbf{u}_b|/c = 7.071\times10^{-2}$, *(c)* $|\mathbf{u}_b|/c = 1.414\times10^{-1}$, *and (d)* $|\mathbf{u}_b|/c = 2.818\times10^{-1}$.

For all three cases, the MPI SRK drop is set with an initial density ratio of approximately 1000 at the thermodynamic state of $T_R = 0.59$, $p_R = 5.762\times10^{-3}$, $\rho_l^R = 3.177$, and $\rho_v^R = 3.288\times10^{-3}$. The SRK parameters are set as $a = 0.01$ and $b = 0.2$ which leads to $\chi = 20$. With radius $r = 30\Delta x$ the drop is initialized in the centre of a two-dimensional domain with 200×200 nodes and the periodic boundary condition is applied in both horizontal and vertical directions. To access the Galilean invariance, the distortion ratio is defined, DR_{90}, as the ratio of the longest diameter of a drop to the diameter perpendicular to the longest one [186]. The MPI SRK drop experienced three stages: the rest, acceleration, and the long rest for each case run. In the beginning, the drop is kept staying at the rest state for 5×10^4 steps to ensure it reaches the equilibrium shape. Then the drop is accelerated diagonally by

$a_x = a_y = 0.0001$ for period of $500\Delta t$ (case 1), $1000\Delta t$ (case 2), and $2000\Delta t$ (case 3), respectively. The accelerated drop is then released for 5×10^5 time steps, for all three cases, to remove the transit effects and enable the drop along with its surroundings to move diagonally at constant velocities. The simulation results are discussed as follows.

At equilibrium state, the MPI SRK drop keeps a perfect circle drop with $DR_{90} = 1.0$ and has density of $\rho_l^R = 3.195$ in contact with vapour density of $\rho_v^R = 5.505\times10^{-3}$. The MPI drop and the pattern of its spurious velocities are shown in Figure 4-10 (a).

As the drop and its surroundings reach higher velocities, the shape eventually distorted from the circle to $DR_{90} = 1.004$ (case 1), $DR_{90} = 1.018$ (case 2), to $DR_{90} = 1.087$ (case 3), which is demonstrated in Figure 4-10 (b),(c),(d). The changes in densities are neglectfully small, in comparison with those of equilibrium case, for all cases smaller than 0.03% for liquid and 3.2% for vapour. The flow pattern, however, is more sensitive to the changes in bulk velocity whose increase from $|\mathbf{u}_b|/c = 7.071\times10^{-2}$ (case 1) to $|\mathbf{u}_b|/c = 1.414\times10^{-1}$ (case 2) and then to $|\mathbf{u}_b|/c = 2.818\times10^{-1}$ (case 3) causes the flow to deviate more from the uniform distribution.

Considering case 3, which is a critical case demonstrated in Figure 4-10 (d), the drop is disfigured noticeably and the system highly violates Galilean invariance as the fluid is unable to damp spatial velocity differences by time. This means that the proposed MPI scheme is well Galilean invariant for $|\mathbf{u}|/c < 0.15$ but violates Galilean invariance beyond this ratio.

As had been discussed in [123, 187, 188], the mechanism of violation of Galilean invariance for the LBM is due to the insufficiency of the equilibrium distribution function, which is Maxwellian expansion to the second order at constant temperature. It introduces the cubic velocity term, $\tau\nabla.(\rho\mathbf{uuu})$, to the viscous momentum flux of the LB system. In this study, the equilibrium distribution function is employed without any modification, therefore the term, $\tau\nabla.(\rho\mathbf{uuu})$, is the only term which violates the second-order Galilean invariance. If $|\mathbf{u}|^2/\theta$ or $|\mathbf{u}|/c$ is very small the cubic velocity

term is negligible in compare with Naiver-Stokes viscous term. That is why when the bulk velocity is increased, the spatial velocity differences are not dissipated by time and the drop shape is distorted.

The MPI SRK drop is tested to obtain its minimum stable relaxation time $\tau_{\min}$. The drop, at different temperatures and interface widths, is located at the centre of the computational domain. The relaxation time is set at $\tau = 1$ initially; after the drop reaches its equilibrium state, τ is gradually and in a quasi-equilibrium process decreased to achieve new lower viscose systems. The process is monitored to record the point before the system crashes at which the relaxation time is taken as the minimum possible relaxation time $\tau_{\min}$. As shown in Table 4-5, the decrease of the temperature and interface width weaken the τ-related stability.

Table 4-5. The minimum possible relaxation time of the MPI SRK drop at different temperatures and interface widths. The interface width is measured from the flat interface simulations and can be obtained by setting χ at a given temperature found in Table 4-4.

T_R	Interface width (Δx)	$\tau_{\min}$
0.60	20	0.562
	30	0.546
	60	0.523
0.75	20	0.526
	30	0.518
	60	0.514
0.90	20	0.514
	30	0.514
	60	0.513

4.7 Conclusion

To summarise, the MPI scheme is extended, which is based on original SC model, in order to eliminate the numerical errors as a result of the discretization effect of the lattice when cubic equations of state are implemented. The thermodynamic consistency

condition has been made more flexible by modifying the forcing scheme by which in addition to cubic EOSs other types such as virial EOS can be employed analytically and consistently in pseudopotential models. In such a way, different pseudopotentials can be identified by the attraction and repulsion parts of cubic EOSs without the need for curve-fitting or trial and error methods.

The most basic and popular cubic EOSs are adopted including the VW, CS, PR, and SRK to demonstrate the validity of the proposed MPI scheme by performing a set of simulations of planar interfaces. For all the cases, the normal component of the pressure tensor is satisfactorily constant along the flat interfaces.

The LB system is analysed in a reduced format which can be compared to real physical systems. The equilibrium interface shapes are predicted from mechanical stability condition and found in good agreement with the simulations. Interface width could be systematically adjusted with the aid of the EOS parameters, while they can positively affect the accuracy of the VLE densities. Such a feature helps to control the interface width in the case of grid refinements.

The proposed MPI scheme provides stable two-phase systems even for very high-density ratios. The liquid branch of the Maxwell construction curve is almost perfectly achieved. Regarding the vapour branch, the errors are negligible and small at low and midrange density ratios (less than 1000) but, at higher density ratios, exponentially grow. The errors can be suppressed by broadening the interface width, i.e. increasing the interface resolution.

We have shown that the isotropy of the circular drops are satisfactorily preserved in the process of shortening the interface width. An MPI SRK drop is moved diagonally in a periodic domain which showed its Galilean invariant at relatively low bulk velocities in addition to being stable. The minimum available relaxation time for the stationary MPI drop is obtained which increases with the decrease of temperature and interface width.

Chapter 5- Boundary conditions for non-ideal fluid flow

5.1 Introduction

Pseudopotential lattice Boltzmann has been viable in modelling intricate non-ideal fluid behaviours such as multiphase flow in porous media. The method, in comparison with the conventional LB, offers the flexibility of dealing with solid-fluid potential interactions. This capability has been well utilised and studied for the purpose of defining wettability of the solid surfaces, where a contact angle can be defined, but not in each phase separately. In this study, we investigate the effect of solid-fluid interactions on the hydrodynamics of non-ideal single-phase fluids, due to wall boundary conditions. We introduce the interaction forces, simulated by pseudopotentials, into two on-site boundary conditions: standard bounce-back (SBB) and Zou and He (ZH) [169] to determine the distributions functions of the boundary nodes. Three different interaction forces are tested: pseudopotential-based interaction (ψ-BI), modified pseudopotential-based interaction (mψ-BI), and a ZH-based interaction (ZH-BI), which is proposed by this study based on the ZH method. The criterion is the achievement of macroscopic poiseuille flow of real fluids which is simulated by the recent multipseudopotential interaction scheme [189]. It is found that the scheme of ψ-BI coupled with SBB creates a relatively high variation and fluctuation of density across the channel. Whilst, the schemes of mψ-BI with SBB, m ψ-BI with ZH, and ZH-BI with ZH generate much less density variation across the channel. Among them, ZH-BI with ZH treatment is superior regarding density fluctuation and the error associated with the resolution, relaxation time, and compressibility.

5.2 Boundary conditions

We begin with a brief discussion on the Standard bounce back scheme which will be tested. We then demonstrate how the fluid-solid interaction forces can be implemented into Zou and He scheme [169] for the pseudopotential model. Finally, the various schemes of solid-fluid interactions are discussed.

5.2.1 Standard bounce back

The standard bounce back is the simplest but popular LBM scheme to treat non-slip boundary conditions. It reverses and sends back the distribution functions penetrated to

the stationary solid surface. For a fluid node in contact with the wall, the unknown distribution functions, f_i, coming from the solid surface can be found from

$$f_i(\mathbf{x}, t+1) = f_{i'}(\mathbf{x}, t^+), \tag{5-1}$$

where i' is the opposite direction to i and t^+ is a post-collision time but before streaming. If the nearest solid nodes are the solid surface especially in complex boundaries, the method is of first-order accuracy [164, 165]. However, if the surface line drawn at halfway between the solid and fluid nodes, the second order of accuracy is achieved [166]. It should be noted in the case of a moving boundary, SBB can be applied straightforwardly by taking into account solid to fluid momentum transfer [5].

5.2.2 Zou and He (ZH) treatment with interaction force

Zou and He [169] proposed a boundary condition scheme, which can be used to set density or velocity at a particular node. The idea is to find unknown distribution functions with the aid of macroscopic values and known distribution functions. Here, we focus on the D2Q9 lattice. For a solid or boundary node, A, at the bottom of a domain shown in Figure 5-1, the distribution functions f_2, f_5, and f_6 have to be defined after every collision-and-stream step.

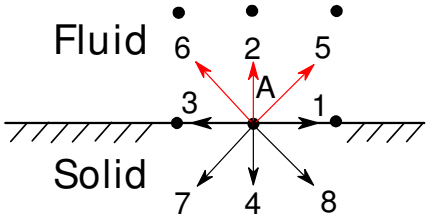

Figure 5-1. After a collision-and-stream step in D2Q9 lattice, the boundary node A placed at the bottom of simulation domain has five known distribution functions f_1, f_3, f_4, f_7, and f_8 and three unknown distribution functions as f_2, f_5, and f_6.

For the pseudopotential LBM and two-dimensional flows, we consider interaction forces acting on node A, namely F_x and F_y. We can set three neighbouring nodes at the bottom as three ghost nodes. Ghost nodes are the nodes which are not a part of the physical domain but form a virtual layer around the boundary of the domain. The densities of wall surface nodes are copied on to the nearest ghost nodes to calculate

interaction force through equation (3-2). The velocity of node A is related to distribution functions via equation (4-4),

$$\rho v_x - \frac{1}{2}F_x = f_1 + f_5 + f_8 - f_3 - f_6 - f_7 \ , \tag{5-2}$$

$$\rho v_y - \frac{1}{2}F_y = f_2 + f_5 + f_6 - f_4 - f_7 - f_8 \ , \tag{5-3}$$

and the density of the node is

$$\rho = f_0 + f_1 + f_2 + f_3 + f_4 + f_5 + f_6 + f_7 + f_8 . \tag{5-4}$$

Therefore, we have three equations for four unknowns as the density is not set as a condition. It should be noted even if density is defined along with the velocity, the system of equations doesn't have a unique solution as f_2, f_5 , and f_6 have the same coefficients in (5-4) and (5-3).

To close the system of equations, we follow the Zou and He [169] that the bounce back rule is valid for the non-equilibrium part of the distribution function perpendicular to the wall,

$$f_2 = f_4 + \frac{2}{3}\rho v_y . \tag{5-5}$$

As a result, the equations are found with solutions

$$\rho = \frac{2(f_0 + f_1 + f_3) + 4(f_4 + f_7 + f_8) - F_y}{2(1 - v_y)} \ , \tag{5-6}$$

$$f_5 = f_7 + \frac{1}{6}\rho v_y + \frac{1}{2}\rho v_x + \frac{1}{2}(-f_1 + f_3) - \frac{1}{4}(F_x + F_y) \ , \tag{5-7}$$

$$f_6 = f_8 + \frac{1}{6}\rho v_y - \frac{1}{2}\rho v_x + \frac{1}{2}(f_1 - f_3) - \frac{1}{4}(-F_x + F_y) . \tag{5-8}$$

For a stationary solid node, velocity in the above equations are set to $u = v = 0$. It should be noted that since the pseudopotential LBM pressure is directly related to density via EOS, the pressure boundary condition can be applied straightforwardly.

However, the velocity component tangent to boundary surface, in this example v_x, should be defined along with the density, or a relation between velocity components should be given, for example, the angle of the velocity vector is known. In such a case, equation (5-6) can be solved for velocity and equation (5-5), (5-7), and (5-8) are treated the same as velocity boundary condition to find f_2, f_5, and f_6.

These solutions can be generalised for all four directions of boundaries of a $D2Q9$ lattice domain. Let's define $\mathbf{n}$ as vector normal to a boundary plane toward outside domain, O the summation of distribution functions that are toward the outside of the domain $\mathbf{e}_i.\mathbf{n} > 0$, and T the summation of the ones which are tangent to the boundary $\mathbf{e}_i.\mathbf{n} = 0$. Then, the density-velocity relation can be expressed as,

$$\rho = \frac{2T + 4O + n_\alpha F_\alpha}{2(1 + n_\alpha v_\alpha)}, \tag{5-9}$$

The general form of the solution for three unknown distribution functions is

$$f_i = f_{i'} + |\mathbf{t}_i| \left[\mathbf{e}_i \cdot (\frac{m}{6}\rho v_x, \frac{1}{2m}\rho v_y) + \sum_{j=1}^{4} f_j \mathbf{t}_j \cdot \mathbf{e}_i - \frac{1}{4}\mathbf{e}_i \cdot \mathbf{F} \right] + \frac{2}{3}\left\|\mathbf{t}_i\right| - 1 |\mathbf{e}_i \cdot \rho \mathbf{v}, \tag{5-10}$$

where $f_{i'}$ is the distribution function opposite to f_i, $m = |\mathbf{n} \cdot (1,3)|$ and $\mathbf{t}_i$ is the tangent of $\mathbf{e}_i$ vector on the boundary surface $\mathbf{t}_i = \mathbf{e}_i - (\mathbf{e}_i \cdot \mathbf{n})\mathbf{n}$.

In addition to the intersection of a solid wall and periodic boundary, corner nodes are almost inevitable situations. For a D2Q9 lattice, a corner node leaves five unknown and three known distribution functions. For example, node B placed at the bottom left of the domain in Figure 5-2 has f_1, f_2, f_5, f_6, and f_8 as unknowns and f_3, f_4, and f_7 as known values. To calculate the interaction force on this node, the densities of solid surface nodes are considered for nearby ghost nodes. We set $v_x = v_y = 0$ and assume the density of the node is known due to the side pressure (density) boundary or extrapolation over nearby nodes. Moreover, we make use of the bounce back rule of non-equilibrium part of both perpendicular distribution functions, equation (5-5) and

$$f_1 = f_3 + \frac{2}{3}\rho v_x , \tag{5-11}$$

where give $f_2 = f_4$, $f_1 = f_3$. The others f_5, f_6, and f_8 now can be found from the system of equations (5-2), (5-3), and (5-4) for which determinant is nonzero, equal to 4. Therefore, we obtain

$$f_5 = f_7 - \frac{1}{4}F_x - \frac{1}{4}F_y , \tag{5-12}$$

$$f_6 = \frac{1}{2}\rho - \frac{1}{2}f_0 - f_3 - f_4 - f_7 + \frac{1}{4}F_x , \tag{5-13}$$

$$f_8 = \frac{1}{2}\rho - \frac{1}{2}f_0 - f_3 - f_4 - f_7 + \frac{1}{4}F_y , \tag{5-14}$$

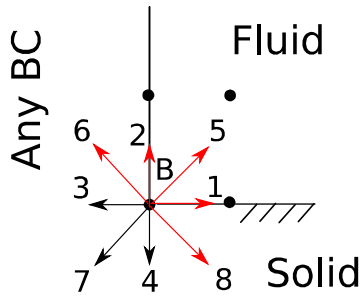

Figure 5-2. After a collision-and-stream step in the D2Q9 lattice, the boundary node B which is placed at the bottom left corner, the intersection of the solid wall and another boundary condition such as pressure or velocity condition, has three known distribution functions f_3, f_4, and f_7 and five unknown distribution functions to be found f_1, f_2, f_5, f_6, and f_8.

It should be noted for complex geometries where the surface is rugged, ZH condition is not as straightforward as SBB.

5.3 Solid-Fluid interactions

In the pseudopotential LBM, the interaction between solid and fluid is considered to control the wettability of a solid surface in contact with two-phase fluid. This idea, in fact, mimics the interactions observed at the molecular level and scales up to macro-scale. However, here we focus on the cases where pseudopotential fluid is in single phase such as compressed liquid and is in contact with stationary solid boundaries. In

such cases, the wettability is less focused but obtaining correct density and velocity profiles along and across the channel are of importance.

The most well-known pseudopotential fluid-solid interactions can be formalised as

$$F_{fs} = -G_{fs}\phi_f(x)\sum_i \phi_s(\mathbf{x}+\mathbf{e}_i)w_i s(\mathbf{x}+\mathbf{e}_i)\mathbf{e}_i \ , \tag{5-15}$$

where G_{fs} is the amplitude, ϕ_f and ϕ_s are fluid and solid potentials respectively, s is a switch function gives 0 for fluid-fluid interactions and 1 for fluid-solid interactions. If a non-wetting fluid is simulated G_{fs} should be positive otherwise negative. Martys and Chen [190] defined a fluid-solid interaction force setting $\phi_f(\mathbf{x}) = \rho(\mathbf{x})$ and $\phi_s = 1$ for a single component system. Raiskinmäki et. al [191] and Sukop et. al [192] proposed to replace the fluid density factor with pseudopotential as $\phi_f(\mathbf{x}) = \psi(\mathbf{x})$ and $\phi_s = 1$. Kang et al. [193] consider a constant density for solid nodes $\phi_f(\mathbf{x}) = \rho(\mathbf{x})$ and $\phi_s = \rho_s$ where ρ_s is an imaginary density set for a solid node. The pseudopotential version of this model is introduced by Benzi et. al [132] where $\phi_f(\mathbf{x}) = \psi(\mathbf{x})$ and $\phi_s = \psi(\rho_s)$. Li et al. [133] assumed the solid node has a density equal to the fluid node which it is interacting with, $\phi_f(\mathbf{x}) = \psi^2(\mathbf{x})$ and $\phi_s = 1$. In this way, the fluid-solid force has the same order of magnitude as fluid-fluid interactions if G and G_{fs} are in the same order. They called their interaction model modified pseudopotential-based interaction (mψ-BI).

Martys and Chen [190] and Kang et al. [193] models are the same because ρ_s is a constant and can be merged with G_{fs}; they are called density-based interactions. The same applies to versions of Raiskinmäki et. al [191] and Benzi et. al [132], pseudopotential-based interactions, where $\psi(\rho_s)$ can be considered as the amplitude of the force. Li et al. [133] assessed all these forces regarding static contact angles and found that pseudopotential-based interaction is more suitable for modelling small contact angles and mψ-BI performs better than the others for achieving greater contact angles.

When using the ZH boundary condition to construct solid nodes, i.e., imposing no-slip boundary condition, a density, ρ_{ZH}, for the solid node is calculated by (5-9). As such, we define the fluid-solid interaction, ZH-based interaction (ZH-BI),

$$F_{fs} = -G_{fs}\psi(\mathbf{x})\sum_i w_i \psi(\mathbf{x}+\mathbf{e}_i, \rho_{ZH}) s(\mathbf{x}+\mathbf{e}_i)\mathbf{e}_i \tag{5-16}$$

This force similar to modified ψ-based force keeps the order of magnitude as fluid-fluid interactions which is the most important point of defining such an interaction force [192].

In this study, we investigate the effects of boundary condition treatments on real fluid flow dynamics. The treatment schemes are the schemes of ψ-based interaction, modified ψ-based interaction, and ZH-based interaction in combinations with either the bounce-back or the ZH boundary treatments.

5.4 Result and discussion

Simulations are performed to assess boundary treatments discussed in section 5.2 for non-ideal fluid flow in 2D Poiseuille flow. The results from simulations are discussed in comparison with the analytical incompressible solution.

5.4.1 Simulation setup

All simulations are run on a two-dimensional square lattice including nine velocities ($D2Q9$). The detail of domain sizes for each case will be given individually. The general setting, unless otherwise stated, is listed as follows. The nondimensional relaxation time and lattice spacing parameter are set to unity $\tau = 1,\ c = 1$. It should be noted that based on (2-42) τ should be $\tau > 0.5$. c represents the scale of the simulation which is not focused here. ZH pressure boundaries opt for driving force of walled poiseuille flow. The MPI forces are calculated by use of Eqs. (3-2) and (4-12) whose parameters, for the SRK EOS, can be found in Table 4-1. The internal forces are embedded in the LBE using Eq. (4-8) which reproduces Navier-Stokes equations to the second order. The thermodynamic values of SRK EOS at the saturation state $T_R = 0.7$ are listed in Table 5-1. $T_R = 0.7$ is selected as middle value in the stable range of MPI-

LB for SRK EOS $0.40 \le T_R < 1$ (see section 4.6.4). The amplitudes of fluid-solid interaction are kept at fluid-fluid interactions $G_j = G_{sf}^j$.

The simulations are run for at least 10^5 steps and velocity of nodes all over the system is monitored to verify that the equilibrium state is reached by

$$\frac{v_{\max}(t) - v_{\max}(t-1)}{v_{\max}(t-1)} \le 10^{-10}. \tag{5-17}$$

where $v_{\max}$ is the velocity magnitude of the node which has the maximum value in the computational domain. The equilibrium time depends on viscosity, domain size, and type of boundary conditions.

Table 5-1. Pressure, density, and temperature of SRK EOS for water at $T_R = 0.7$ for at $a = 0.01$ and $b = 0.2$ and $\omega = 0.344$. The numbers are in lattice unit. β_R is reduced compressibility.

T $\times 10^3$	T_c $\times 10^2$	p_{sat} $\times 10^4$	p_c $\times 10^3$	ρ_l^{sat}	ρ_v^{sat} $\times 10^2$	ρ_c	α	$\beta_R(\rho_l^{sat})$ $\times 10^2$
7.0936 90	1.0133 84	1.9867 63	4.3899 98	3.7860 23	2.9481 38	1.2996 05	1.3535 99	1.5548 78

We assess the results in comparison with the analytical solution of poiseuille flow in a no-slip channel. It is assumed that the flow is fully developed and uniform in x direction and pressure drop is linear along the channel $dp/dx = \Delta p / L_x$,

$$u = \frac{L_y^2}{2\mu}\left(\frac{\Delta p}{L_x}\right)\left[\frac{y}{L_y} - \left(\frac{y}{L_y}\right)^2\right]. \tag{5-18}$$

where L_y is the height of the channel, L_x is the width of the channel, μ is the dynamic viscosity, Δp is the pressure drop along the channel (see Figure 5-3). If a body force, $\mathbf{F}_b$, is exerted on the fluid with the acceleration of $\mathbf{a}$, the term $\Delta p / L_x$ is replaced by $|\mathbf{F}_b| = |\rho \mathbf{a}|$.

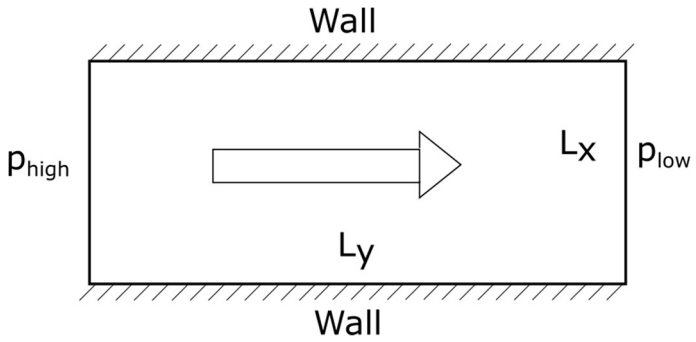

Figure 5-3. Sketch of the poiseuille flow. The fluid is driven by either pressure difference $\Delta p = p_{high} - p_{low}$ *or body force* $\mathbf{F}_b$ *and it has zero velocity at top and bottom boundary. The flow profile is described by equation (5-18).*

5.4.2 Periodic poiseuille flow

The first set of simulations are run for poiseuille flow where no solid boundary condition is applied [194] as an ideal test case that the fluid itself creates a poiseuille profile. To do so, we charge MPI fluid in a fully periodic rectangular domain and exert two equal but opposite body forces. The first one only acts on the top half and the other one moves the bottom half. The sketch of the simulation domain is shown in Figure 5-4. The body force is added to equation Eq. (4-8), thus, $\mathbf{F}_{total} = \mathbf{F}_b + \mathbf{F}_{MPI}$.

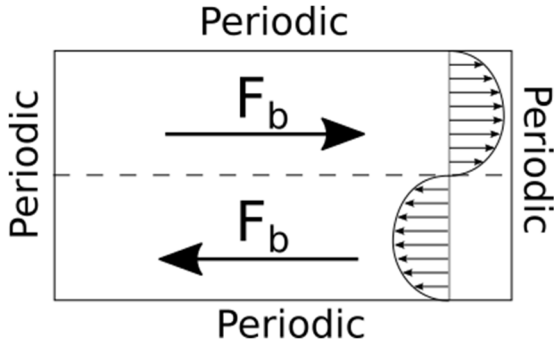

Figure 5-4. Sketch of the periodic poiseuille domain.

Figure 5-5 shows the velocity profile for half of the periodic domain. Different results are coming from various channel resolutions $N_y = 4,8,16$. The errors against resolutions for different relaxation times $\tau = 0.6, 0.8, 1.1$ are shown in Figure 5-6. It should be noted based on (2-42), increase of τ increases the viscosity of the system. The errors show that the pseudopotential LBM has the second order of accuracy same as

the conventional LBM. In fact, after inspection of density throughout the domain, we found that no density change is observed in the whole domain in all simulations. It means the pseudopotential forces are neutralising each other since pseudopotentials are calculated by node density and, therefore, the model acts similar to the conventional LBM.

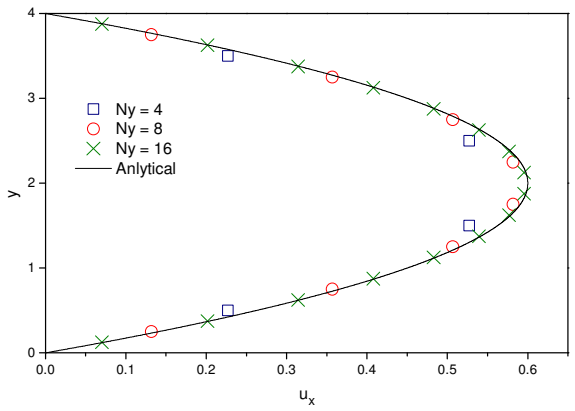

Figure 5-5. The poiseuille profile of velocity across the channel for half of the periodic box for different channel sizes $N_y = 4,8,16$ *compared with analytical solution (5-18).*

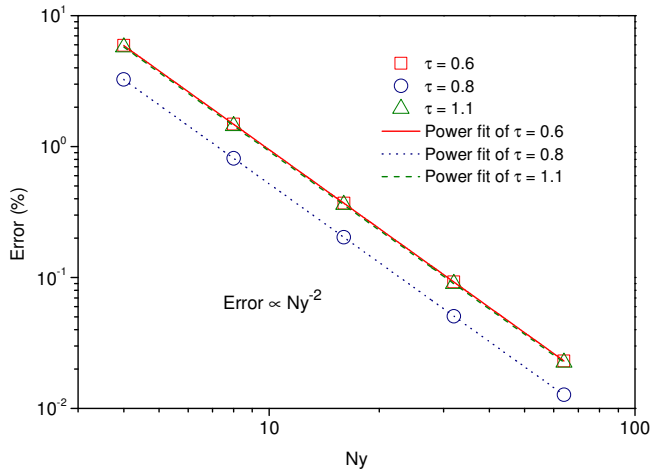

Figure 5-6. The errors of periodic box simulations due to the deviation of velocity from analytical solution (5-18) at various channel sizes. The errors show the second order of accuracy.

5.4.3 Pseudopotential-based interaction

To simulate poiseuille flow in between two stationary plates, we first employ ψ-based interaction and set SBB, Eq. (5-1), at top and bottom of the channel, abbreviated as ψ-SBB. The MPI fluid at density $\rho_{initialization} = 1.03\rho_l^{sat}$ is initially charged in the channel

which is equivalent to 3% compressed water at $T_R = 0.7$. The domain size is 120×16 which is considered long enough to reach a steady state and wide enough to create poiseuille flow based on results of section 5.4.2. The flow is driven by pressure (or density) difference at left and right boundaries with the aid of ZH boundary treatment. Densities at left and right boundaries are set as $\rho_{left} = 1.03\rho_{initial}$ and $\rho_{right} = \rho_{initial}$ respectively. A virtual density should be considered for the walls from which the pseudopotential can be calculated. We consider three scenarios, large density $\rho_s = 1.1\rho_{left}$, average density $\rho_s = (\rho_{left} + \rho_{right})/2$, small density $\rho_s = 0.9\rho_{right}$ for all solid nodes. The sketch of the simulation domain is demonstrated in Figure 5-7. The interaction between the fluid and solid nodes are found from equation (5-15) which is calculated for each potential of MPI scheme.

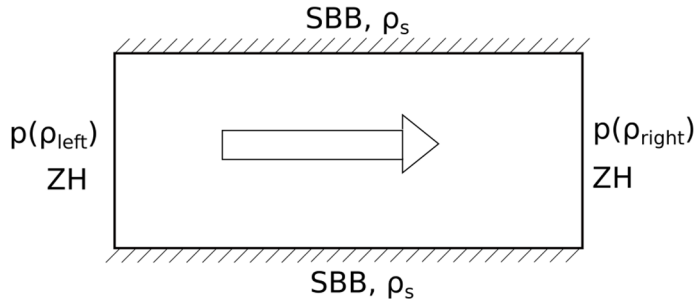

Figure 5-7. The sketch of simulation domain for the ψ -based interaction. For top and bottom boundaries SBB is considered while left and right boundaries are ZH pressure condition at ρ_{left} and ρ_{right}. As $\rho_{left} > \rho_{right}$ the fluid flows from left to right. ρ_s is the virtual density of solid surface.

Figure 5-8 (a) depicts profiles of density across the channel at $x = L_x/2$ with $\rho_s = 1.1\rho_{left}$ for $a = 0.1, 0.01, 0.001$, and $b = 0.2$ i.e. $\Upsilon = b^2/a = 0.4, 4, 40$. Because $\Upsilon = b^2/a$ changes the compressibility here we only change a without losing the generality of studying the effect of b. In the case $\Upsilon = 40$, which repulsion part of SRK EOS is dominant and the fluid acts more compressible, the density of fluid from wall decreases smoothly in a parabolic distribution to a minimum density slightly lower than the average density. By increasing the attraction parameter or decreasing Υ, where the fluid is more approaching to incompressible fluid, the density forms a plateau in the centre closer to average density but density fluctuations near the wall increases. The

velocity profile of these cases are shown in Figure 5-8 (d). The best agreement with analytical results (incompressible fluid flow) comes from $\Upsilon = 0.4$, but with increase of Υ the fluid moves faster than incompressible one.

The relatively same results are observed when $\rho_s = 0.9\rho_{right}$ which are demonstrated in Figure 5-8 (c). The density of liquid increases from wall density to the average density at the centre and decrease of Υ moves the profile of density from smooth parabolic shape to flat profile at the centre with fluctuations close to the wall. The associated velocity profiles are shown in Figure 5-8 (f). The best consistency between simulation and the incompressible theory (5-18) is for $0.4 < \Upsilon < 4$. The worse deviation is seen at the highly compressible fluid, $\Upsilon = 40$.

According to Figure 5-8 (b), the less density gradient is seen across the channel if wall density is set to average density $\rho_s = \rho_{ave}$. However, we show in section 5.4.4 that this only happens here because the sample is taken at the halfway along the channel. The velocity profiles, seen in Figure 5-8 (e), stays relatively the same as previous cases.

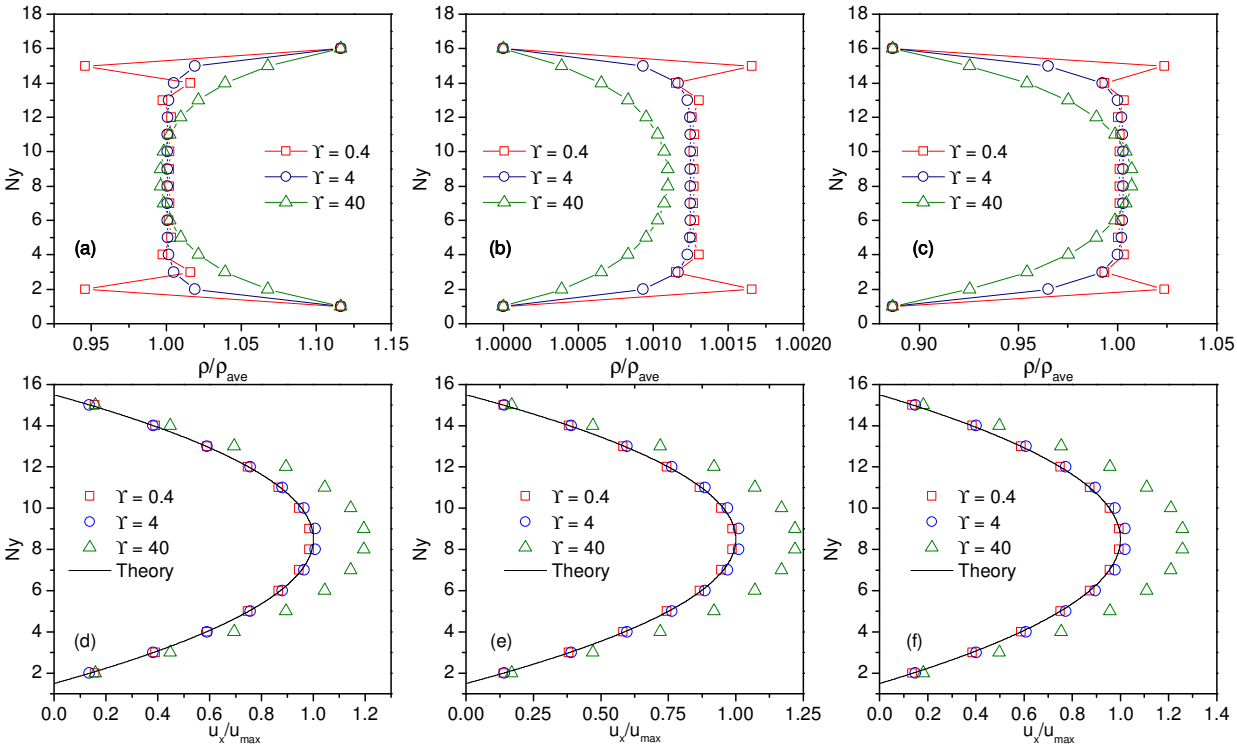

Figure 5-8. The profile of density and velocity across the poseuille flow channel for ψ -SBB treatment (a),(d) $\rho_s = 1.1\rho_{left}$, (b),(e) $\rho_s = \rho_{ave}$ and (c),(f) $\rho_s = 0.9\rho_{right}$.

5.4.4 ZH-based and modified Pseudopotential-based interaction

To simulate walls in poiseuille flow, here, we investigate three cases of fluid-solid treatment: ZH-based solid-fluid interaction coupled with ZH zero velocity (ZH-ZH), modified ψ-based interaction with bounce-back (mψ-SBB), and modified ψ-based interaction with ZH zero velocity (mψ-ZH). The MPI fluid and inlet (or left), and outlet (or right) boundaries are set the same as Section 5.4.3. The tests focus on density fluctuations across the channel and errors due to resolution, relaxation time, and parameter Υ. The error is defined as a deviation from macroscopic poiseuille flow, equation (5-18).

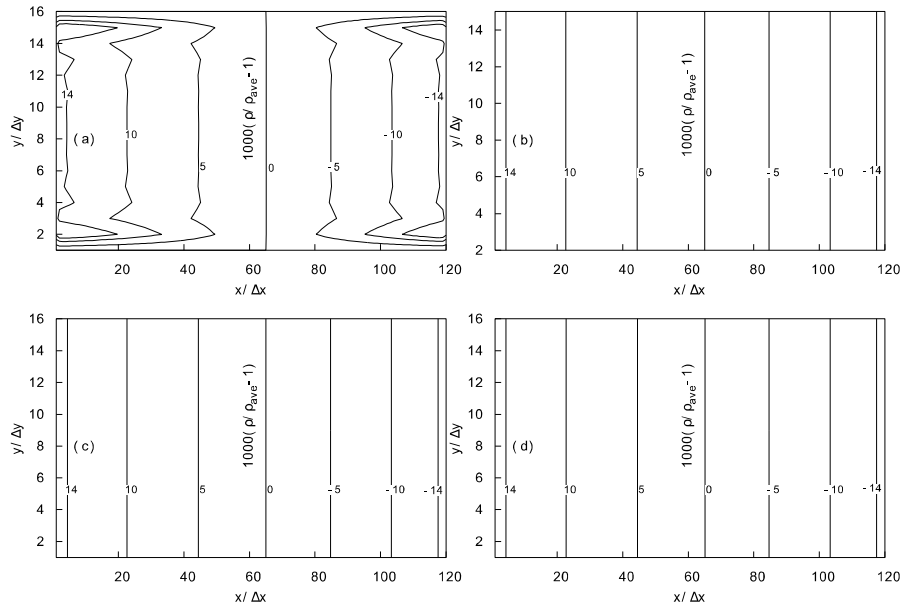

Figure 5-9. Contours of density over the simulation domain for (a) ψ -SBB (b) mψ -SBB (c) mψ -ZH (d) ZH-ZH boundary treatments. Contour levels are made based on $1000(\rho / \rho_{ave} - 1)$. *For the case m ψ -SBB no density required to be defined for the wall nodes and for ψ -SBB* $\rho_s = \rho_{ave}$. *For all cases* $\Upsilon = 0.4$ *is chosen.*

Figure 5-9 shows the contours of density field over the computational domain for ψ-SBB, mψ-SBB, mψ-ZH, and ZH-ZH treatments. The density variation across the channel for ψ-SBB is much larger than the others. It is seen that only around halfway through the channel an almost vertical contour level, $1000(\rho / \rho_{ave} - 1) = 0$, is formed. Since the wall density is set at $\rho_s = \rho_{ave}$, that is the location where the density of fluid

coincides with the density of the wall. Therefore, any density difference between fluid and solid causes the density fluctuation. Due to high fluid fluctuation, this treatment is not comparable to the others, and hereafter we concentrate on the other treatments.

Figure 5-10 demonstrates the density variation across the channel for the three cases ZH-ZH, mψ-SBB, and mψ-ZH. Since at macro-scale desired flow field has a constant density across the channel, we define a simple parameter, $fluctuation = (\rho_{max} - \rho_{min}) / \rho_{max}$. In section 5.4.3, we have seen that at $\Upsilon = 0.4$ the system shows highest density fluctuations close to the boundary wall, therefore, this value is chosen for these simulations. The density fluctuation is very small for all these cases. mψ-SBB and mψ-ZH show the same accuracy but ZH-ZH treatment gives one order of magnitude less in fluctuation. Moreover, when using ZH-ZH, the wall density calculated by ZH method will be well in accordance with interior nodes. The density jumps near the wall, filled circles, can be observed in mψ-ZH treatment.

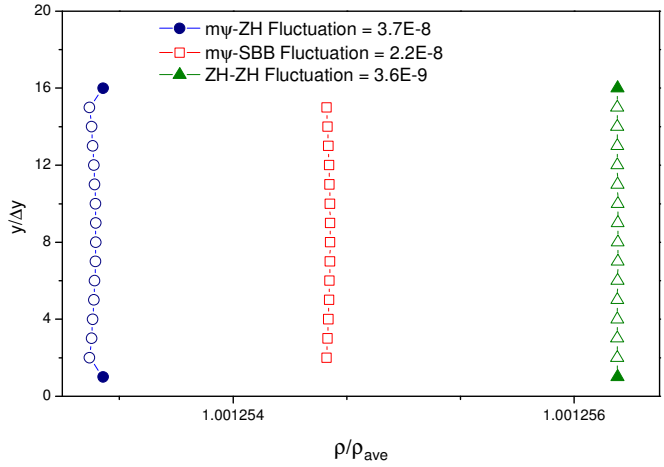

Figure 5-10. Profile of density across the channel for three boundary treatments ZH-ZH, mψ -SBB, and mψ -ZH. The filled circle and triangles represent wall nodes defined by ZH boundary treatment.

The error is depicted versus vertical resolution of the domain in Figure 5-11. As expected, the error decreases with the increase of domain resolution. ZH-ZH treatment is superior at different resolutions. After that, mψ-SBB placed which shows lesser error than mψ-ZH. It should be noted the horizontal resolution is accordingly increased to make sure that the dynamics of the simulations stay the same.

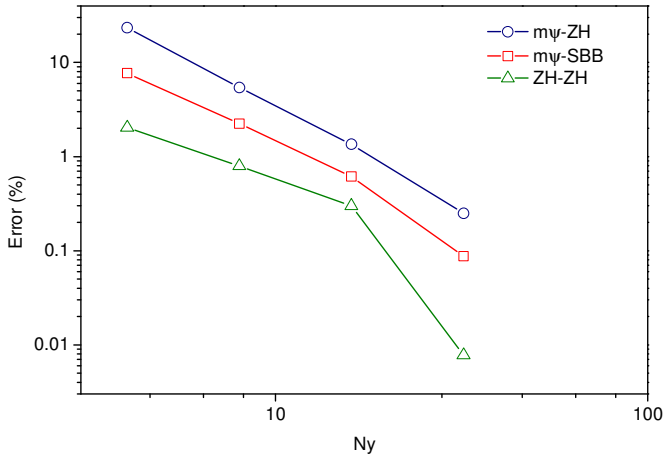

Figure 5-11. Error due to the vertical resolution of the channel for three boundary treatments ZH-ZH, m ψ -SBB, and m ψ -ZH.

The effect of relaxation time is shown in Figure 5-12. In the range of $0.6 \le \tau \le 1.1$, the m ψ-ZH method shows more error than the others but the error almost reaches a plateau after $\tau = 0.8$. Similar behaviour is seen for ZH-ZH treatment which has the lowest error. However, m ψ-SBB error increases proportionally with τ.

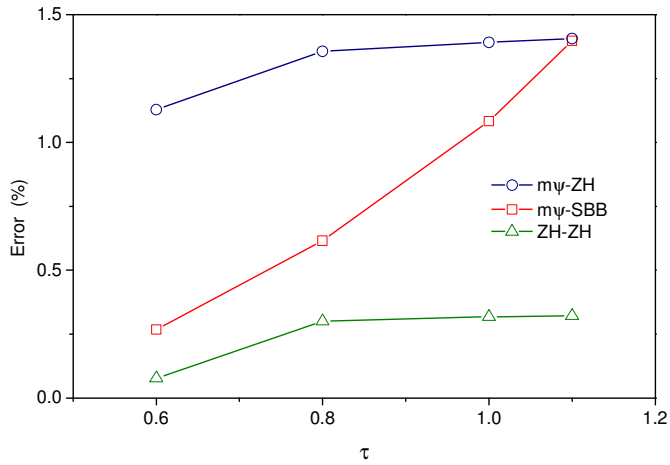

Figure 5-12. Error due to change of relaxation time for three boundary treatments ZH-ZH, m ψ -SBB, and m ψ -ZH.

If we increase Υ in SRK EOS, in fact, the compressibility of the liquid is increased which intensify compressibility error of lattice Boltzmann. Such behaviour can be seen in Figure 5-13 which demonstrates the error dependency to parameter Υ. ZH-ZH treatment is better than the others and m ψ-SBB is placed after m ψ-ZH.

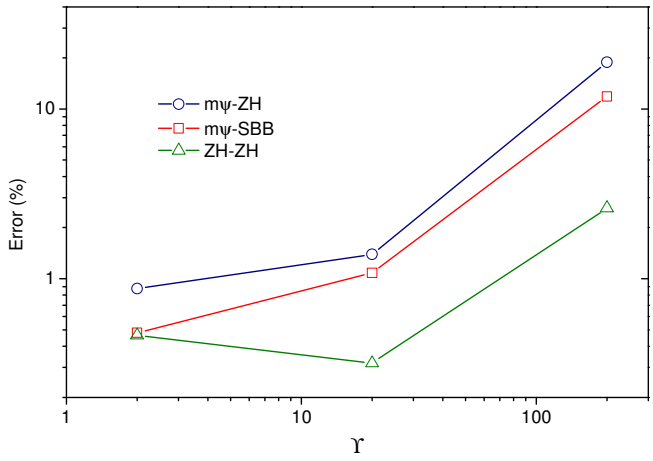

Figure 5-13. Error due to parameter Υ for three boundary treatments ZH-ZH, mψ -SBB, and mψ -ZH.

5.5 Conclusion

We have chosen the two most popular boundary treatments, SBB and ZH. The aim is applying them in the pseudopotential LBM to obtain the ability to simulate compressed single-phase flow involved with stationary walls especially water in a channel. MPI scheme with SRK EOS is utilised to model water. Three force interactions between fluid and solid are considered ψ-based, and modified ψ-based, which are found in the literature, and ZH-based which is defined in this chapter. They are combined with SBB and ZH. The criterion is closeness to macroscopic poiseuille flow.

The first case periodic poiseuille flow is studied as an ideal poiseuille flow purely made of LB equation without the need of boundary conditions. It is shown that the method is second order accurate as density is constant all over the channel and the method coincides with conventional LB without pseudopotential interactions.

ψ-based interaction along with SBB gives high-density gradient and fluctuations near the wall. The choice of wall density plays the key role. The closer it is to neighbouring fluid nodes, the less fluctuation is observed which makes it hard to use in complex geometries. The velocity profile is very close to analytical poiseuille flow unless the parameter Υ is greatly increased which makes the fluid more compressible and consequently strengthens compressibility error of LB method.

The density fluctuations of ZH-ZH, mψ-SBB, and mψ-ZH are far less than and not comparable to ψ-SBB. Therefore, those three treatments are studied together. The performance of them assessed based on density variation across the channel, and error because of domain resolution, relaxation time, and Υ parameter. ZH-ZH in all cases is superior. It has one order of magnitude less variation of density across the channel in comparison with others. It shows less error in different resolutions, a low relaxation time dependency and less compressibility error. In all cases, mψ-ZH takes the third place after mψ-SBB.

Chapter 6 – Summary and future work

6.1 Summary of the thesis

The overall aim of this thesis was to develop a new LBM multiphase scheme, multipseudopotential interaction, which overcomes the current shortcomings seen in the pseudopotential schemes such as thermodynamic inconsistency, being limited to low-density ratios, and unable to control interface width independent of EOS. The multipseudopotential interaction scheme has been studied for the effect of solid-fluid interactions on the bulk flow as well.

At the first step, the SC force is expanded in a way that each sub-force has a thermodynamic consistent shape. We showed that the summation of these forces satisfies the thermodynamic requirement as well. The outcome equation of state has a virial-like shape with an arbitrary number of free parameter. This EOS could be fitted on the practical EOSs and simulate them in the LB system.

The MPI scheme is compared with the commonly used SPI scheme in reproducing VW and CS EOS. It is found that, first of all, in contrast to the SPI scheme, the MPI scheme is scalable and shows the independency of equilibrium densities under grid refinement. Secondly, when reproducing the Maxwell construction, at the vapour branch, the SPI prediction deviates significantly with decrease in temperature, whereas the MPI scheme shows much better results, and their accuracies are independent of temperature (for $0.74 < T_R < 0.99$), and the type of chosen EOS.

There exist the thermodynamic states where the SPI pseudopotential has real values in the liquid (vapour) region and imaginary values in the vapour (liquid) region, thereby causing the collapse of simulations. The nature of the MPI scheme is free from this shortcoming.

Besides curve-fitting, an alternative procedure in achieving a specific MPI two-phase system is suggested using only the properties of pressure, liquid density, vapour density, and sound speeds in vapour and liquid phase. The results from the simulated system show good agreement with the requested data.

At the second step, the MPI scheme is extended for cubic and virial equations of state. The thermodynamic consistency condition has been made more flexible to employ those EOSs analytically and consistently in pseudopotential schemes, without the need for curve-fitting or trial and error procedures.

The LB system is analysed in a reduced format which can be compared to real physical systems. The equilibrium interface shapes are predicted from mechanical stability condition and found in good agreement with the simulations. Interface width is systematically adjusted with the aid of the EOS parameters. It can positively affect the accuracy of the results.

The proposed MPI scheme provides stable two-phase systems even for very high-density ratios. The liquid branch of the Maxwell construction curve is almost perfectly achieved. Regarding the vapour branch, the errors are negligible and small to density ratio of 1000. However, at higher density ratios, the errors grow exponentially. The errors can be suppressed by broadening the interface width.

The main drawback of multipseudopotential scheme is higher computational costs in comparison with original Shan-Chen model. For example, in the case of SRK EOS, three interaction forces are calculated in one time-step between two nodes. Moreover, the scheme is completely based on Shan-Chen model, therefore, it inherits the Shan-Chen frame work. For instance, it is only applicable to isothermal flows and compressibility error is inherent in the scheme.

We have shown that the isotropy of the circular drops is satisfactorily preserved in the process of shortening the interface width. An MPI drop is moved diagonally in a periodic domain which showed the Galilean invariant.

At the third step, we investigate the effect the two most popular wall boundary treatments: SBB and ZH on the (non-ideal) bulk flow. Three force interactions between fluid and solid are considered ψ-based, modified ψ-based, which are found in the literature, and ZH-based which is defined in this thesis. They are combined with SBB and ZH. The criterion is closeness to macroscopic poiseuille flow.

ψ-based interaction along with SBB gives high-density gradient and fluctuations near the wall. The velocity profile is very close to analytical poiseuille flow unless the parameter Υ is greatly increased which makes the fluid more compressible and consequently strengthens compressibility error of LB method.

The density fluctuations of ZH-ZH, mψ-SBB, and mψ-ZH are much less than ψ-SBB. Therefore, those three treatments are studied together. ZH-ZH in all cases is superior. It has one order of magnitude less variation of density across the channel in comparison with others. It shows less error in different resolutions, a low relaxation time dependency and less compressibility error. In all cases, mψ-ZH takes the third place after mψ-SBB.

6.2 Future work proposals

The multipseudopotential interaction scheme introduced in this thesis is limited to 2D, isothermal, single component, two-phase flow. However, it is the basis for many other developments such as the addition of an interface tension force, multi-relaxation time technique, heat transfer, and other fluid components.

Pseudopotential schemes lack a specific independent force or source term describing interface tension. However, recent modifications, especially the work of [143], show that this capability is achievable. Therefore, adding tunable interface tension to MPI is doable and makes the scheme more versatile.

MRT is a more general form of the LBM with a collision matrix where moments of distribution functions like density, momentum are relaxed with different time scales. It solves the deficiency of constant Prandtl number in the SRT. MRT is more stable than SRT and can simulate flows on D3Q13 lattice. Studying multipseudopotential interaction in the MRT framework is another important target.

Pseudopotential schemes found many applications in fuel cells and heat transfer phenomena involving with boiling and evaporation. They utilise a secondary lattice Boltzmann equation to account for heat transfer in the fluid. Such idea can be imported

to powerful multipseudopotential interaction scheme as it has intrinsic thermodynamic consistency by itself.

One of the advantages of pseudopotential schemes over the other multiphase systems is the ease of handling multicomponent systems. For a two-component system, two lattices simply simulate two fluids, however, in the case of MPI, the interface interactions can be complex due to multiple interaction forces. Therefore, interface forces should be separately defined and investigated.

REFERENCES

[1] Anderson, J., *Computational Fluid Dynamics*. 1995: McGraw-Hill Education.

[2] Karniadakis, G.E., A. Beskok, and N. Aluru, *Microflows and Nanoflows: Fundamentals and Simulation*. 2006: Springer New York.

[3] Allen, P. and D.J. Tildesley, *Computer Simulation of Liquids*. 1989: Clarendon Press.

[4] Groot, R.D. and P.B. Warren, *Dissipative particle dynamics: Bridging the gap between atomistic and mesoscopic simulation.* Journal of Chemical Physics, 1997. **107**(11): p. 4423.

[5] Aidun, C.K. and J.R. Clausen, *Lattice-Boltzmann Method for Complex Flows.* Annual Review of Fluid Mechanics, 2009. **42**(1): p. 439-472.

[6] White, F.M. and R.Y. Chul, *Fluid Mechanics*. 2016: McGraw-Hill Education.

[7] Powell, R.L., *Experimental techniques for multiphase flows.* Physics of fluids, 2008. **20**(4): p. 040605.

[8] Butler, J.E. and R.T. Bonnecaze, *Imaging of particle shear migration with electrical impedance tomography.* Physics of fluids, 1999. **11**(8): p. 1982-1994.

[9] Norman, J.T., H.V. Nayak, and R.T. Bonnecaze, *Migration of buoyant particles in low-Reynolds-number pressure-driven flows.* Journal of Fluid Mechanics, 2005. **523**: p. 1-35.

[10] Etuke, E.O. and R.T. Bonnecaze, *Measurement of angular velocities using electrical impedance tomography.* Flow Measurement and Instrumentation, 1998. **9**(3): p. 159-169.

[11] Melling, A., *Tracer particles and seeding for particle image velocimetry.* Measurement Science and Technology, 1997. **8**(12): p. 1406.

[12] Seymour, J.D. and P.T. Callaghan, *Generalized approach to NMR analysis of flow and dispersion in porous media.* AIChE Journal, 1997. **43**(8): p. 2096-2111.

[13] Lee, S., et al., *Combined effect of sedimentation velocity fluctuation and self-sharpening on interface broadening.* Physics of Fluids A: Fluid Dynamics, 1992. **4**(12): p. 2601-2606.

[14] Abbott, J., et al., *Experimental observations of particle migration in concentrated suspensions: Couette flow.* Journal of rheology, 1991. **35**(5): p. 773-795.

[15] Jeong, E.K., S. Altobelli, and E. Fukushima, *NMR imaging studies of stratified flows in a horizontal rotating cylinder.* Physics of Fluids, 1994. **6**(9): p. 2901-2906.

[16] Gatehouse, P.D., et al., *Applications of phase-contrast flow and velocity imaging in cardiovascular MRI.* European radiology, 2005. **15**(10): p. 2172-2184.

[17] Fukushima, E., *Nuclear magnetic resonance as a tool to study flow.* Annual review of fluid mechanics, 1999. **31**(1): p. 95-123.

[18] Gladden, L.F., *Nuclear magnetic resonance in chemical engineering: Principles and applications.* Chemical Engineering Science, 1994. **49**(20): p. 3339-3408.

[19] Günther, H., *NMR Spectroscopy: Basic Principles, Concepts and Applications in Chemistry*. 2013: Wiley.

[20] Tayler, A.B., et al., *Applications of ultra-fast MRI to high voidage bubbly flow: measurement of bubble size distributions, interfacial area and hydrodynamics.* Chemical engineering science, 2012. **71**: p. 468-483.

[21] Haacke, E.M., et al., *Magnetic resonance imaging: physical principles and sequence design*. Vol. 82. 1999: Wiley-Liss New York:.

[22] Pedrotti, F.L. and L.S. Pedrotti, *Introduction to Optics*. 1993: Prentice Hall.
[23] Heindel, T.J., *A review of X-ray flow visualization with applications to multiphase flows.* Journal of Fluids Engineering, 2011. **133**(7): p. 074001.
[24] Mondy, L., et al., *Techniques of measuring particle motions in concentrated suspensions.* International journal of multiphase flow, 1986. **12**(3): p. 497-502.
[25] Wang, Y., et al., *Ultrafast X-ray study of dense-liquid-jet flow dynamics using structure-tracking velocimetry.* Nature Physics, 2008. **4**(4): p. 305.
[26] Mondy, L.A., et al., *Techniques of measuring particle motions in concentrated suspensions.* International Journal of Multiphase Flow, 1986. **12**(3): p. 497-502.
[27] Rowe, P. and C. Yacono, *The bubbling behaviour of fine powders when fluidised.* Chemical Engineering Science, 1976. **31**(12): p. 1179-1192.
[28] Rowe, P., L. Santoro, and J. Yates, *The division of gas between bubble and interstitial phases in fluidised beds of fine powders.* Chemical Engineering Science, 1978. **33**(1): p. 133-140.
[29] Yates, Y., D. Cheesman, and Y. Sergeev, *Experimental observations of voidage distribution around bubbles in a fluidized bed.* Chemical engineering science, 1994. **49**(12): p. 1885-1895.
[30] Luggar, R.D., et al., *X-ray tomographic imaging in industrial process control.* Radiation Physics and Chemistry, 2001. **61**(3): p. 785-787.
[31] Jenneson, P., et al., *Examining nanoparticle assemblies using high spatial resolution x-ray microtomography.* Journal of applied physics, 2004. **96**(5): p. 2889-2894.
[32] McLeod, F. and M. Anliker. *Multiple gate pulsed Doppler flowmeter*. in *IEEE TRANSACTIONS ON SONICS AND ULTRASONICS*. 1972. IEEE-INST ELECTRICAL ELECTRONICS ENGINEERS INC 345 E 47TH ST, NEW YORK, NY 10017-2394.
[33] Takeda, Y., *Velocity profile measurement by ultrasonic Doppler method.* Experimental thermal and fluid science, 1995. **10**(4): p. 444-453.
[34] Xu, H.J. and C.K. Aidun, *Characteristics of fiber suspension flow in a rectangular channel.* International Journal of Multiphase Flow, 2005. **31**(3): p. 318-336.
[35] Bröring, S., et al., *Flow structure of the dispersed gasphase in real multiphase chemical reactors investigated by a new ultrasound–doppler technique.* The Canadian Journal of Chemical Engineering, 1991. **69**(6): p. 1247-1256.
[36] Yeh, Y. and H. Cummins, *Localized fluid flow measurements with an He–Ne laser spectrometer.* Applied Physics Letters, 1964. **4**(10): p. 176-178.
[37] Riva, C., B. Ross, and G.B. Benedek, *Laser Doppler Measurements of Blood Flow in Capillary Tubes and Retinal Arteries.* Investigative Ophthalmology & Visual Science, 1972. **11**(11): p. 936-944.
[38] Nilsson, G.E., T. Tenland, and P.A. Oberg, *Evaluation of a laser Doppler flowmeter for measurement of tissue blood flow.* IEEE Transactions on Biomedical Engineering, 1980(10): p. 597-604.
[39] Holloway, G.A. and D.W. Watkins, *Laser Doppler measurement of cutaneous blood flow.* Journal of Investigative Dermatology, 1977. **69**(3): p. 306-309.
[40] Hibiki, T., et al., *Visualization of fluid phenomena using a high frame-rate neutron radiography with a steady thermal neutron beam.* Nuclear Instruments and Methods in Physics Research Section A: Accelerators, Spectrometers, Detectors and Associated Equipment, 1994. **351**(2-3): p. 423-436.

[41] He, X., S. Chen, and R. Zhang, *A Lattice Boltzmann Scheme for Incompressible Multiphase Flow and Its Application in Simulation of Rayleigh–Taylor Instability.* Journal of Computational Physics, 1999. **152**(2): p. 642-663.
[42] Satoh, A., *1 - Outline of Molecular Simulation and Microsimulation Methods*, in *Introduction to Practice of Molecular Simulation*. 2011, Elsevier: London. p. 1-27.
[43] Satoh, A., *2 - Outline of Methodology of Simulations*, in *Introduction to Practice of Molecular Simulation*. 2011, Elsevier: London. p. 29-47.
[44] Allen, M.P., *Introduction to molecular dynamics simulation.* Computational soft matter: from synthetic polymers to proteins, 2004. **23**: p. 1-28.
[45] Alder, B.J. and T. Wainwright, *Studies in molecular dynamics. I. General method.* The Journal of Chemical Physics, 1959. **31**(2): p. 459-466.
[46] Hans Meuer, E.S., Jack Dongarra, Horst Simon, Martin Meuer. *November 2016 List*. 2016 [cited 05/01/2017]; Available from: https://www.top500.org.
[47] Hoogerbrugge, P. and J. Koelman, *Simulating microscopic hydrodynamic phenomena with dissipative particle dynamics.* EPL (Europhysics Letters), 1992. **19**(3): p. 155.
[48] Espanol, P. and P. Warren, *Statistical mechanics of dissipative particle dynamics.* EPL (Europhysics Letters), 1995. **30**(4): p. 191.
[49] Pagonabarraga, I. and D. Frenkel, *Dissipative particle dynamics for interacting systems.* The Journal of Chemical Physics, 2001. **115**(11): p. 5015-5026.
[50] Liu, M., P. Meakin, and H. Huang, *Dissipative particle dynamics with attractive and repulsive particle-particle interactions.* Physics of Fluids (1994-present), 2006. **18**(1): p. 017101.
[51] Kim, J.M. and R.J. Phillips, *Dissipative particle dynamics simulation of flow around spheres and cylinders at finite Reynolds numbers.* Chemical engineering science, 2004. **59**(20): p. 4155-4168.
[52] Chen, S., et al., *Flow around spheres by dissipative particle dynamics.* Physics of Fluids (1994-present), 2006. **18**(10): p. 103605.
[53] Moeendarbary, E., et al., *Migration of DNA molecules through entropic trap arrays: a dissipative particle dynamics study.* Microfluidics and Nanofluidics, 2010. **8**(2): p. 243-254.
[54] Reddy, H. and J. Abraham, *Dissipative-particle dynamics simulations of flow over a stationary sphere in compliant channels.* Physics of Fluids (1994-present), 2009. **21**(5): p. 053303.
[55] Clark, A.T., et al., *Mesoscopic simulation of drops in gravitational and shear fields.* Langmuir, 2000. **16**(15): p. 6342-6350.
[56] Liu, M., P. Meakin, and H. Huang, *Dissipative particle dynamics simulation of multiphase fluid flow in microchannels and microchannel networks.* Physics of Fluids (1994-present), 2007. **19**(3): p. 033302.
[57] Tiwari, A. and J. Abraham, *Dissipative particle dynamics simulations of liquid nanojet breakup.* Microfluidics and Nanofluidics, 2008. **4**(3): p. 227-235.
[58] Kumar, A., et al., *From dissipative particle dynamics scales to physical scales: a coarse-graining study for water flow in microchannel.* Microfluidics and Nanofluidics, 2009. **7**(4): p. 467-477.
[59] Duong-Hong, D., et al., *Dissipative particle dynamics simulations of electroosmotic flow in nano-fluidic devices.* Microfluidics and Nanofluidics, 2008. **4**(3): p. 219-225.
[60] Eggers, J. and E. Villermaux, *Physics of liquid jets.* Reports on progress in physics, 2008. **71**(3): p. 036601.

[61] Milne-Thomson, L.M., *Theoretical Aerodynamics*. 1966: Dover Publications.
[62] Evans, M.W., F.H. Harlow, and E. Bromberg, *The particle-in-cell method for hydrodynamic calculations*. 1957, LOS ALAMOS NATIONAL LAB NM.
[63] LeVeque, R.J., *Finite volume methods for hyperbolic problems*. Vol. 31. 2002: Cambridge university press.
[64] Connor, J.J. and C.A. Brebbia, *Finite element techniques for fluid flow*. 2013: Newnes.
[65] Pozrikidis, C., *Finite-Difference Methods*, in *Fluid Dynamics: Theory, Computation, and Numerical Simulation*. 2009, Springer US: Boston, MA. p. 424-493.
[66] Patankar, S., *Numerical heat transfer and fluid flow*. 1980: CRC press.
[67] Prosperetti, A. and G. Tryggvason, *Computational methods for multiphase flow*. 2009: Cambridge university press.
[68] Harlow, F.H. and J.E. Welch, *Numerical Calculation of Time-Dependent Viscous Incompressible Flow of Fluid with Free Surface.* Physics of Fluids, 1965. **8**(12): p. 2182-2189.
[69] Noh, W.F. and P. Woodward, *SLIC (Simple Line Interface Calculation)*, in *Proceedings of the Fifth International Conference on Numerical Methods in Fluid Dynamics June 28 – July 2, 1976 Twente University, Enschede*, A.I. van de Vooren and P.J. Zandbergen, Editors. 1976, Springer Berlin Heidelberg: Berlin, Heidelberg. p. 330-340.
[70] Osher, S. and J.A. Sethian, *Fronts propagating with curvature-dependent speed: algorithms based on Hamilton-Jacobi formulations.* Journal of computational physics, 1988. **79**(1): p. 12-49.
[71] Klingenberg, C. and B. Plohr, *An Introduction to front Tracking*, in *Multidimensional Hyperbolic Problems and Computations*, J. Glimm and A. Majda, Editors. 1991, Springer New York. p. 203-216.
[72] Hirt, C.W. and B.D. Nichols, *Volume of fluid (VOF) method for the dynamics of free boundaries.* Journal of Computational Physics, 1981. **39**(1): p. 201-225.
[73] Rudman, M., *Volume-tracking methods for interfacial flow calculations.* International journal for numerical methods in fluids, 1997. **24**(7): p. 671-691.
[74] Youngs, D.L., *Time-dependent multi-material flow with large fluid distortion.* Numerical methods for fluid dynamics, 1982. **24**(2): p. 273-285.
[75] Sussman, M., P. Smereka, and S. Osher, *A level set approach for computing solutions to incompressible two-phase flow.* Journal of Computational physics, 1994. **114**(1): p. 146-159.
[76] A.R. Wadhwa, V.M., J. Abraham. *Numerical Studies of Droplet Interactions*. in *Proceedings of International Conference on Liquid Atomization and Spray Systems*. 2003. Sorrento, Italy.
[77] Tryggvason, G., et al., *A Front-Tracking Method for the Computations of Multiphase Flow.* Journal of Computational Physics, 2001. **169**(2): p. 708-759.
[78] Yoon, S.G., *A Fully Nonlinear Model for Atomization of High-Speed Jets*. 2002, Purdue University.
[79] Manninen, M., V. Taivassalo, and S. Kallio, *On the mixture model for multiphase flow*. 1996, Technical Research Centre of Finland Finland.
[80] Niu, Y.Y., Y.C. Lin, and C.H. Chang, *A further work on multi-phase two-fluid approach for compressible multi-phase flows.* International journal for numerical methods in fluids, 2008. **58**(8): p. 879-896.
[81] Drew, D., L. Cheng, and R. Lahey, *The analysis of virtual mass effects in two-phase flow.* International Journal of Multiphase Flow, 1979. **5**(4): p. 233-242.

[82] Mohamad, A.A., *Lattice Boltzmann Method*. 1 ed. 2011: Springer-Verlag London.
[83] Wolf-Gladrow, D.A., *4. Some statistical mechanics*, in *Lattice Gas Cellular Automata and Lattice Boltzmann Models: An Introduction*. 2000, Springer Berlin Heidelberg: Berlin, Heidelberg. p. 139-158.
[84] Succi, S., I.V. Karlin, and H. Chen, *Colloquium: Role of the H theorem in lattice Boltzmann hydrodynamic simulations.* Reviews of Modern Physics, 2002. **74**(4): p. 1203.
[85] Sterling, J.D. and S. Chen, *Stability Analysis of Lattice Boltzmann Methods.* Journal of Computational Physics, 1996. **123**(1): p. 196-206.
[86] Wolf-Gladrow, D., *5. Lattice Boltzmann Models*, in *Lattice Gas Cellular Automata and Lattice Boltzmann Models*. 2000, Springer Berlin Heidelberg. p. 159-246.
[87] Bhatnagar, P.L., E.P. Gross, and M. Krook, *A model for collision processes in gases. I. Small amplitude processes in charged and neutral one-component systems.* Physical review, 1954. **94**(3): p. 511.
[88] McNamara, G.R. and G. Zanetti, *Use of the Boltzmann Equation to Simulate Lattice-Gas Automata.* Physical Review Letters, 1988. **61**(20): p. 2332-2335.
[89] Higuera, F.J. and J. Jiménez, *Boltzmann Approach to Lattice Gas Simulations.* EPL (Europhysics Letters), 1989. **9**(7): p. 663.
[90] Koelman, J.M.V.A., *A Simple Lattice Boltzmann Scheme for Navier-Stokes Fluid Flow.* EPL (Europhysics Letters), 1991. **15**(6): p. 603.
[91] Qian, Y.H., D.D. Humières, and P. Lallemand, *Lattice BGK Models for Navier-Stokes Equation.* EPL (Europhysics Letters), 1992. **17**(6): p. 479.
[92] K. Diemer, K.H., S. Chen, T. Shimomura, and G. D. Doolen, *Density andVelocityDependence ofReynoldsNumbers for Several Lattice Gas Models*, in *Lattice Gas Methods for Partial Differential Equations*, G.D. Doolen, Editor. 1989.
[93] Eggels, J.G.M., *Direct and large-eddy simulation of turbulent fluid flow using the lattice-Boltzmann scheme.* International Journal of Heat and Fluid Flow, 1996. **17**(3): p. 307-323.
[94] Pan, C., M. Hilpert, and C.T. Miller, *Lattice-Boltzmann simulation of two-phase flow in porous media.* Water Resources Research, 2004. **40**(1): p. W01501.
[95] Huang, H., L. Wang, and X.-y. Lu, *Evaluation of three lattice Boltzmann models for multiphase flows in porous media.* Computers & Mathematics with Applications, 2011. **61**(12): p. 3606-3617.
[96] Zhang, J., P.C. Johnson, and A.S. Popel, *Red blood cell aggregation and dissociation in shear flows simulated by lattice Boltzmann method.* Journal of biomechanics, 2008. **41**(1): p. 47-55.
[97] Fang, H., et al., *Lattice Boltzmann method for simulating the viscous flow in large distensible blood vessels.* Physical Review E, 2002. **65**(5): p. 051925.
[98] Succi, S., *Lattice Boltzmann 2038.* EPL, 2015. **109**(5): p. 50001.
[99] Succi, S., *Lattice Boltzmann across scales: from turbulence to DNA translocation.* The European Physical Journal B-Condensed Matter and Complex Systems, 2008. **64**(3): p. 471-479.
[100] Safi, M.A. and S. Turek, *Efficient computations for high density ratio rising bubble flows using a diffused interface, coupled lattice Boltzmann-level set scheme.* Computers & Mathematics with Applications, 2015. **70**(6): p. 1290-1305.

[101] Yong, W.-A. and L.-S. Luo, *Nonexistence of H theorems for the athermal lattice Boltzmann models with polynomial equilibria.* Physical Review E, 2003. **67**(5): p. 051105.
[102] Wagner, A.J., *An H-theorem for the lattice Boltzmann approach to hydrodynamics.* Europhysics Letters, 1998. **44**(2): p. 144-149.
[103] D'Humieres, D., et al., *Multiple-relaxation-time lattice Boltzmann models in three dimensions.* Philos Trans A Math Phys Eng Sci, 2002. **360**(1792): p. 437-51.
[104] d'Humieres, D., M. Bouzidi, and P. Lallemand, *Thirteen-velocity three-dimensional lattice Boltzmann model.* Phys Rev E Stat Nonlin Soft Matter Phys, 2001. **63**(6 Pt 2): p. 066702.
[105] Lallemand, P. and L.-S. Luo, *Theory of the lattice Boltzmann method: Dispersion, dissipation, isotropy, Galilean invariance, and stability.* Physical Review E, 2000. **61**(6): p. 6546-6562.
[106] Premnath, K.N., M.J. Pattison, and S. Banerjee, *Generalized lattice Boltzmann equation with forcing term for computation of wall-bounded turbulent flows.* Physical Review E, 2009. **79**(2): p. 026703.
[107] Pan, C., L.-S. Luo, and C.T. Miller, *An evaluation of lattice Boltzmann schemes for porous medium flow simulation.* Computers & Fluids, 2006. **35**(8-9): p. 898-909.
[108] Premnath, K.N. and J. Abraham, *Three-dimensional multi-relaxation time (MRT) lattice-Boltzmann models for multiphase flow.* Journal of Computational Physics, 2007. **224**(2): p. 539-559.
[109] Luo, L.-S., et al., *Numerics of the lattice Boltzmann method: Effects of collision models on the lattice Boltzmann simulations.* Physical Review E, 2011. **83**(5): p. 056710.
[110] Shan, X. and H. Chen, *Simulation of nonideal gases and liquid-gas phase transitions by the lattice Boltzmann equation.* Physical Review E, 1994. **49**(4): p. 2941-2948.
[111] Shan, X. and H. Chen, *Lattice Boltzmann model for simulating flows with multiple phases and components.* Physical Review E, 1993. **47**(3): p. 1815-1819.
[112] Gunstensen, A.K., et al., *Lattice Boltzmann model of immiscible fluids.* Physical Review A, 1991. **43**(8): p. 4320-4327.
[113] Swift, M.R., W.R. Osborn, and J.M. Yeomans, *Lattice Boltzmann Simulation of Nonideal Fluids.* Physical Review Letters, 1995. **75**(5): p. 830-833.
[114] Rothman, D. and J. Keller, *Immiscible cellular-automaton fluids.* Journal of Statistical Physics, 1988. **52**(3-4): p. 1119-1127.
[115] Reis, T. and T.N. Phillips, *Lattice Boltzmann model for simulating immiscible two-phase flows.* Journal of Physics A: Mathematical and Theoretical, 2007. **40**(14): p. 4033.
[116] Grunau, D., S. Chen, and K. Eggert, *A lattice Boltzmann model for multiphase fluid flows.* Physics of Fluids A: Fluid Dynamics, 1993. **5**(10): p. 2557-2562.
[117] Latva-Kokko, M. and D.H. Rothman, *Diffusion properties of gradient-based lattice Boltzmann models of immiscible fluids.* Physical Review E, 2005. **71**(5): p. 056702.
[118] Leclaire, S., M. Reggio, and J.-Y. Trépanier, *Numerical evaluation of two recoloring operators for an immiscible two-phase flow lattice Boltzmann model.* Applied Mathematical Modelling, 2012. **36**(5): p. 2237-2252.
[119] Swift, M.R., et al., *Lattice Boltzmann simulations of liquid-gas and binary fluid systems.* Physical Review E, 1996. **54**(5): p. 5041-5052.

[120] Holdych, D.J., et al., *An Improved Hydrodynamics Formulation for Multiphase Flow Lattice-Boltzmann Models.* International Journal of Modern Physics C, 1998. **09**(08): p. 1393-1404.
[121] Kalarakis, A.N., V.N. Burganos, and A.C. Payatakes, *Galilean-invariant lattice-Boltzmann simulation of liquid-vapor interface dynamics.* Physical Review E, 2002. **65**(5): p. 056702.
[122] Kalarakis, A.N., V.N. Burganos, and A.C. Payatakes, *Three-dimensional lattice-Boltzmann model of van der Waals fluids.* Physical Review E, 2003. **67**(1): p. 016702.
[123] Wagner, A.J. and Q. Li, *Investigation of Galilean invariance of multi-phase lattice Boltzmann methods.* Physica A: Statistical Mechanics and its Applications, 2006. **362**(1): p. 105-110.
[124] Wagner, A.J., *Thermodynamic consistency of liquid-gas lattice Boltzmann simulations.* Physical Review E, 2006. **74**(5): p. 056703.
[125] Zheng, H.W., C. Shu, and Y.T. Chew, *A lattice Boltzmann model for multiphase flows with large density ratio.* Journal of Computational Physics, 2006. **218**(1): p. 353-371.
[126] He, X., S. Chen, and G.D. Doolen, *A Novel Thermal Model for the Lattice Boltzmann Method in Incompressible Limit.* Journal of Computational Physics, 1998. **146**(1): p. 282-300.
[127] Nourgaliev, R.R., et al., *The lattice Boltzmann equation method: theoretical interpretation, numerics and implications.* International Journal of Multiphase Flow, 2003. **29**(1): p. 117-169.
[128] Lee, T. and C.-L. Lin, *A stable discretization of the lattice Boltzmann equation for simulation of incompressible two-phase flows at high density ratio.* Journal of Computational Physics, 2005. **206**(1): p. 16-47.
[129] Kupershtokh, A.L., D.A. Medvedev, and D.I. Karpov, *On equations of state in a lattice Boltzmann method.* Computers & Mathematics with Applications, 2009. **58**(5): p. 965-974.
[130] Hyväluoma, J. and J. Harting, *Slip Flow Over Structured Surfaces with Entrapped Microbubbles.* Physical Review Letters, 2008. **100**(24): p. 246001.
[131] Yuan, P. and L. Schaefer, *Equations of state in a lattice Boltzmann model.* Physics of Fluids, 2006. **18**(4): p. 042101.
[132] Benzi, R., et al., *Mesoscopic modeling of a two-phase flow in the presence of boundaries: The contact angle.* Physical Review E, 2006. **74**(2): p. 021509.
[133] Li, Q., et al., *Contact angles in the pseudopotential lattice Boltzmann modeling of wetting.* Phys Rev E Stat Nonlin Soft Matter Phys, 2014. **90**(5-1): p. 053301.
[134] Frijters, S., F. Günther, and J. Harting, *Effects of nanoparticles and surfactant on droplets in shear flow.* Soft Matter, 2012. **8**(24): p. 6542-6556.
[135] Márkus, A. and G. Házi, *Numerical simulation of the detachment of bubbles from a rough surface at microscale level.* Nuclear Engineering and Design, 2012. **248**: p. 263-269.
[136] Huang, H., M. Krafczyk, and X. Lu, *Forcing term in single-phase and Shan-Chen-type multiphase lattice Boltzmann models.* Physical Review E, 2011. **84**(4): p. 046710.
[137] Middleton, R.S., et al., *The cross-scale science of CO2 capture and storage: from pore scale to regional scale.* Energy & Environmental Science, 2012. **5**(6): p. 7328-7345.

[138] Connington, K. and T. Lee, *A review of spurious currents in the lattice Boltzmann method for multiphase flows.* Journal of mechanical science and technology, 2012. **26**(12): p. 3857.
[139] Shan, X., *Analysis and reduction of the spurious current in a class of multiphase lattice Boltzmann models.* Physical Review E, 2006. **73**(4): p. 047701.
[140] Sbragaglia, M., et al., *Generalized lattice Boltzmann method with multirange pseudopotential.* Physical Review E, 2007. **75**(2): p. 026702.
[141] Shan, X., *Pressure tensor calculation in a class of nonideal gas lattice Boltzmann models.* Physical Review E, 2008. **77**(6): p. 066702.
[142] Falcucci, G., et al., *Lattice Boltzmann Models with Mid-Range Interactions.* Communications in computational physics, 2007. **2**: p. 1071-1084.
[143] Li, Q. and K. Luo, *Achieving tunable surface tension in the pseudopotential lattice Boltzmann modeling of multiphase flows.* Physical Review E, 2013. **88**(5): p. 053307.
[144] Succi, S., *The lattice Boltzmann equation: for fluid dynamics and beyond*. 2001: Oxford university press.
[145] He, X.Y. and G.D. Doolen, *Thermodynamic foundations of kinetic theory and Lattice Boltzmann models for multiphase flows.* Journal of Statistical Physics, 2002. **107**(1-2): p. 309-328.
[146] Chen, L., et al., *A critical review of the pseudopotential multiphase lattice Boltzmann model: Methods and applications.* International Journal of Heat and Mass Transfer, 2014. **76**(0): p. 210-236.
[147] Sbragaglia, M. and X. Shan, *Consistent pseudopotential interactions in lattice Boltzmann models.* Physical Review E, 2011. **84**(3): p. 036703.
[148] Sbragaglia, M. and D. Belardinelli, *Interaction pressure tensor for a class of multicomponent lattice Boltzmann models.* Physical Review E, 2013. **88**(1): p. 013306.
[149] Shan, X., X.-F. Yuan, and H. Chen, *Kinetic theory representation of hydrodynamics: a way beyond the Navier-Stokes equation.* Journal of Fluid Mechanics, 2006. **550**(1): p. 413-441.
[150] Zhang, J. and F. Tian, *A bottom-up approach to non-ideal fluids in the lattice Boltzmann method.* EPL (Europhysics Letters), 2008. **81**(6): p. 66005.
[151] Li, Q., K.H. Luo, and X.J. Li, *Forcing scheme in pseudopotential lattice Boltzmann model for multiphase flows.* Physical Review E, 2012. **86**(1): p. 016709.
[152] Falcucci, G., et al., *Lattice Boltzmann spray-like fluids.* EPL (Europhysics Letters), 2008. **82**(2): p. 24005.
[153] Falcucci, G., S. Ubertini, and S. Succi, *Lattice Boltzmann simulations of phase-separating flows at large density ratios: the case of doubly-attractive pseudo-potentials.* Soft Matter, 2010. **6**(18): p. 4357-4365.
[154] Chibbaro, S., et al., *Lattice Boltzmann models for nonideal fluids with arrested phase-separation.* Physical Review E, 2008. **77**(3): p. 036705.
[155] Benzi, R., et al., *Herschel-Bulkley rheology from lattice kinetic theory of soft glassy materials.* EPL (Europhysics Letters), 2010. **91**(1): p. 14003.
[156] Colosqui, C.E., et al., *Mesoscopic simulation of non-ideal fluids with self-tuning of the equation of state.* Soft matter, 2012. **8**(14): p. 3798-3809.
[157] Zarghami, A., N. Looije, and H. Van den Akker, *Assessment of interaction potential in simulating nonisothermal multiphase systems by means of lattice Boltzmann modeling.* Physical Review E, 2015. **92**(2): p. 023307.

[158] Guo, Z., C. Zheng, and B. Shi, *Discrete lattice effects on the forcing term in the lattice Boltzmann method.* Physical Review E, 2002. **65**(4): p. 046308.
[159] He, X., X. Shan, and G.D. Doolen, *Discrete Boltzmann equation model for nonideal gases.* Physical Review E, 1998. **57**(1): p. R13-R16.
[160] Li, Q., et al., *Lattice Boltzmann methods for multiphase flow and phase-change heat transfer.* Progress in Energy and Combustion Science, 2016. **52**: p. 62-105.
[161] Li, Q., K.H. Luo, and X.J. Li, *Lattice Boltzmann modeling of multiphase flows at large density ratio with an improved pseudopotential model.* Physical Review E, 2013. **87**(5): p. 053301.
[162] Lycett-Brown, D. and K.H. Luo, *Improved forcing scheme in pseudopotential lattice Boltzmann methods for multiphase flow at arbitrarily high density ratios.* Physical Review E, 2015. **91**(2): p. 023305.
[163] Chen, H., S. Chen, and W.H. Matthaeus, *Recovery of the Navier-Stokes equations using a lattice-gas Boltzmann method.* Physical Review A, 1992. **45**(8): p. R5339-R5342.
[164] Ginzbourg, I. and P.M. Adler, *Boundary flow condition analysis for the three-dimensional lattice Boltzmann model.* J. Phys. II France, 1994. **4**(2): p. 191-214.
[165] Noble, D.R., et al., *A consistent hydrodynamic boundary condition for the lattice Boltzmann method.* Physics of Fluids (1994-present), 1995. **7**(1): p. 203-209.
[166] Ziegler, D.P., *Boundary conditions for lattice Boltzmann simulations.* Journal of Statistical Physics, 1993. **71**(5): p. 1171-1177.
[167] Chen, S., D. Martínez, and R. Mei, *On boundary conditions in lattice Boltzmann methods.* Physics of Fluids, 1996. **8**(9): p. 2527-2536.
[168] Zhao-Li, G., Z. Chu-Guang, and S. Bao-Chang, *Non-equilibrium extrapolation method for velocity and pressure boundary conditions in the lattice Boltzmann method.* Chinese Physics, 2002. **11**(4): p. 366.
[169] Zou, Q. and X. He, *On pressure and velocity boundary conditions for the lattice Boltzmann BGK model.* Physics of Fluids, 1997. **9**(6): p. 1591-1598.
[170] Inamuro, T., M. Yoshino, and F. Ogino, *A non-slip boundary condition for lattice Boltzmann simulations.* Physics of Fluids, 1995. **7**(12): p. 2928-2930.
[171] Skordos, P.A., *Initial and boundary conditions for the lattice Boltzmann method.* Physical Review E, 1993. **48**(6): p. 4823-4842.
[172] Latt, J., et al., *Straight velocity boundaries in the lattice Boltzmann method.* Physical Review E, 2008. **77**(5): p. 056703.
[173] Bouzidi, M.h., M. Firdaouss, and P. Lallemand, *Momentum transfer of a Boltzmann-lattice fluid with boundaries.* Physics of Fluids, 2001. **13**(11): p. 3452.
[174] Junk, M. and Z. Yang, *One-point boundary condition for the lattice Boltzmann method.* Phys Rev E Stat Nonlin Soft Matter Phys, 2005. **72**(6 Pt 2): p. 066701.
[175] Nash, R.W., et al., *Choice of boundary condition for lattice-Boltzmann simulation of moderate-Reynolds-number flow in complex domains.* Physical Review E, 2014. **89**(2): p. 023303.
[176] He, X. and L.-S. Luo, *Theory of the lattice Boltzmann method: From the Boltzmann equation to the lattice Boltzmann equation.* Physical Review E, 1997. **56**(6): p. 6811-6817.
[177] Holdych, D.J., et al., *Truncation error analysis of lattice Boltzmann methods.* Journal of Computational Physics, 2004. **193**(2): p. 595-619.
[178] Wolfram, S., *Cellular automaton fluids 1: Basic theory.* Journal of Statistical Physics, 1986. **45**(3-4): p. 471-526.

[179] Khajepor, S., J. Wen, and B. Chen, *Multipseudopotential interaction: A solution for thermodynamic inconsistency in pseudopotential lattice Boltzmann models.* Physical Review E, 2015. **91**(2): p. 023301.
[180] Soave, G., *20 years of Redlich-Kwong equation of state.* Fluid Phase Equilibria, 1993. **82**(0): p. 345-359.
[181] Soave, G., *Equilibrium constants from a modified Redlich-Kwong equation of state.* Chemical Engineering Science, 1972. **27**(6): p. 1197-1203.
[182] Peng, D.-Y. and D.B. Robinson, *A New Two-Constant Equation of State.* Industrial & Engineering Chemistry Fundamentals, 1976. **15**(1): p. 59-64.
[183] Danesh, A., *PVT and phase behaviour of petroleum reservoir fluids*. Vol. 47. 1998: Elsevier.
[184] Schmidt, G. and H. Wenzel, *A modified van der Waals type equation of state.* Chemical Engineering Science, 1980. **35**(7): p. 1503-1512.
[185] Patel, N.C. and A.S. Teja, *A new cubic equation of state for fluids and fluid mixtures.* Chemical Engineering Science, 1982. **37**(3): p. 463-473.
[186] Sellami, N., et al., *Dynamics of rising CO2 bubble plumes in the QICS field experiment: Part 1 – The experiment.* International Journal of Greenhouse Gas Control, 2015. **38**: p. 44-51.
[187] Qian, Y.H. and S.A. Orszag, *Lattice BGK Models for the Navier-Stokes Equation: Nonlinear Deviation in Compressible Regimes.* EPL (Europhysics Letters), 1993. **21**(3): p. 255.
[188] Nie, X., X. Shan, and H. Chen, *Galilean invariance of lattice Boltzmann models.* EPL (Europhysics Letters), 2008. **81**(3): p. 34005.
[189] Khajepor, S. and B. Chen, *Multipseudopotential interaction: A consistent study of cubic equations of state in lattice Boltzmann models.* Physical Review E, 2016. **93**(1): p. 013303.
[190] Martys, N.S. and H. Chen, *Simulation of multicomponent fluids in complex three-dimensional geometries by the lattice Boltzmann method.* Physical Review E, 1996. **53**(1): p. 743-750.
[191] Raiskinmäki, P., et al., *Spreading dynamics of three-dimensional droplets by the lattice-Boltzmann method.* Computational Materials Science, 2000. **18**(1): p. 7-12.
[192] Sukop, M.C. and D.T. Thorne, *Lattice Boltzmann Modeling: An Introduction for Geoscientists and Engineers*. 2006: Springer-Verlag Berlin Heidelberg. XII, 172.
[193] Kang, Q., D. Zhang, and S. Chen, *Displacement of a two-dimensional immiscible droplet in a channel.* Physics of Fluids, 2002. **14**(9): p. 3203-3214.
[194] Backer, J.A., et al., *Poiseuille flow to measure the viscosity of particle model fluids.* The Journal of Chemical Physics, 2005. **122**(15): p. 154503.